

THE MILKY WAY TOMOGRAPHY WITH SDSS. I. STELLAR NUMBER DENSITY DISTRIBUTION

MARIO JURIC^{1,2}, ŽELJKO IVEŽIĆ³, ALYSON BROOKS³, ROBERT H. LUPTON¹, DAVID SCHLEGEL^{1,4}, DOUGLAS FINKBEINER^{1,5},
NIKHIL PADMANABHAN^{4,6}, NICHOLAS BOND¹, BRANIMIR SESAR³, CONSTANCE M. ROCKOSI^{3,7}, GILLIAN R. KNAPP¹,
JAMES E. GUNN¹, TAKAHIRO SUMI^{1,8}, DONALD P. SCHNEIDER⁹, J. C. BARENTINE¹⁰, HOWARD J. BREWINGTON¹⁰,
J. BRINKMANN¹⁰, MASATAKA FUKUGITA¹¹, MICHAEL HARVANEK¹⁰, S. J. KLEINMAN¹⁰,
JUREK KRZESINSKI^{10,12}, DAN LONG¹⁰, ERIC H. NEILSEN, JR.¹³, ATSUKO NITTA¹⁰,
STEPHANIE A. SNEDDEN¹⁰ AND DONALD G. YORK¹⁴

Received 2005 October 21; accepted 2007 September 6

ABSTRACT

Using the photometric parallax method we estimate the distances to ~ 48 million stars detected by the Sloan Digital Sky Survey (SDSS) and map their three-dimensional number density distribution in the Galaxy. The currently available data sample the distance range from 100 pc to 20 kpc and cover 6500 deg² of sky, mostly at high Galactic latitudes ($|b| > 25$). These stellar number density maps allow an investigation of the Galactic structure with no a priori assumptions about the functional form of its components. The data show strong evidence for a Galaxy consisting of an oblate halo, a disk component, and a number of localized overdensities. The number density distribution of stars as traced by M dwarfs in the solar neighborhood ($D < 2$ kpc) is well fit by two exponential disks (the thin and thick disk) with scale heights and lengths, bias corrected for an assumed 35% binary fraction, of $H_1 = 300$ pc and $L_1 = 2600$ pc, and $H_2 = 900$ pc and $L_2 = 3600$ pc, and local thick-to-thin disk density normalization $\rho_{\text{thick}}(R_\odot)/\rho_{\text{thin}}(R_\odot) = 12\%$. We use the stars near main-sequence turnoff to measure the shape of the Galactic halo. We find a strong preference for oblate halo models, with best-fit axis ratio $c/a = 0.64$, $\rho_H \propto r^{-2.8}$ power-law profile, and the local halo-to-thin disk normalization of 0.5%. Based on a series of Monte Carlo simulations, we estimate the errors of derived model parameters not to be larger than $\sim 20\%$ for the disk scales and $\sim 10\%$ for the density normalization, with largest contributions to error coming from the uncertainty in calibration of the photometric parallax relation and poorly constrained binary fraction. While generally consistent with the above model, the measured density distribution shows a number of statistically significant localized deviations. In addition to known features, such as the Monoceros stream, we detect two overdensities in the thick disk region at cylindrical galactocentric radii and heights $(R, Z) \sim (6.5, 1.5)$ kpc and $(R, Z) \sim (9.5, 0.8)$ kpc and a remarkable density enhancement in the halo covering over 1000 deg² of sky toward the constellation of Virgo, at distances of ~ 6 –20 kpc. Compared to counts in a region symmetric with respect to the $l = 0^\circ$ line and with the same Galactic latitude, the Virgo overdensity is responsible for a factor of 2 number density excess and may be a nearby tidal stream or a low-surface brightness dwarf galaxy merging with the Milky Way. The $u - g$ color distribution of stars associated with it implies metallicity lower than that of thick disk stars and consistent with the halo metallicity distribution. After removal of the resolved overdensities, the remaining data are consistent with a smooth density distribution; we detect no evidence of further unresolved clumpy substructure at scales ranging from ~ 50 pc in the disk to ~ 1 –2 kpc in the halo.

Subject headings: Galaxy: disk — Galaxy: fundamental parameters — Galaxy: halo — Galaxy: structure

Online material: color figures

1. INTRODUCTION

In the canonical model of Milky Way formation (Eggen et al. 1962, hereafter ELS62), the Galaxy began with a relatively rapid ($\sim 10^8$ yr) radial collapse of the initial protogalactic cloud, followed by an equally rapid settling of gas into a rotating disk. This model readily explained the origin and general structural, kine-

matic, and metallicity correlations of observationally identified populations of field stars (Baade 1944; O’Connell 1958): low metallicity Population II stars formed during the initial collapse and populate the extended *stellar halo*; younger Population I and intermediate Population II stars formed after the gas had settled into the Galactic plane and constitute the *disk*.

The observationally determined distribution of disk stars is commonly described by exponential density laws (Bahcall &

¹ Department of Astrophysical Sciences, Princeton University, Princeton, NJ 08544.

² School of Natural Sciences, Institute for Advanced Study, Princeton, NJ 08540.

³ Department of Astronomy, University of Washington, Box 351580, Seattle, WA 98195.

⁴ Lawrence Berkeley National Laboratory, One Cyclotron Road, MS 50R5032, Berkeley, CA, 94720.

⁵ Harvard-Smithsonian Center for Astrophysics, 60 Garden Street, Cambridge, MA 02138.

⁶ Department of Physics, Princeton University, Princeton, NJ 08544.

⁷ University of California Santa Cruz, 1156 High Street, Santa Cruz, CA 95060.

⁸ Solar-Terrestrial Environment Laboratory, Nagoya University, Furo-cho, Chikusa-ku, Nagoya, 464-8601, Japan.

⁹ Department of Astronomy and Astrophysics, Pennsylvania State University, University Park, PA 16802.

¹⁰ Apache Point Observatory, P.O. Box 59, Sunspot, NM 88349.

¹¹ Institute for Cosmic Ray Research, University of Tokyo, Kashiwa, Chiba, Japan.

¹² Mt. Suhora Observatory, Cracow Pedagogical University, ulica Podchorznych 2, 30-084 Cracow, Poland.

¹³ Fermi National Accelerator Laboratory, P.O. Box 500, Batavia, IL 60510.

¹⁴ Department of Astronomy and Astrophysics and Enrico Fermi Institute, University of Chicago, Chicago, IL 60637.

Soneira 1980; Gilmore & Reid 1983; Gilmore et al. 1989), while power laws or flattened de Vaucouleurs spheroids are usually used to describe the halo (e.g., Wyse & Gilmore 1989; Larsen 1996; see also a review by Majewski 1993). In both the disk and the halo, the distribution of stars is expected to be a smooth function of position, perturbed only slightly by localized bursts of star formation or spiral structure induced shocks.

However, for some time, starting with the pioneering work of Searle & Zinn (1978), continuing with the studies of stellar counts and count asymmetries from the Palomar Observatory Sky Survey (e.g., Larsen 1996; Larsen & Humphreys 1996; Parker et al. 2003), and most recently with the data from modern large-scale sky surveys (e.g., the Sloan Digital Sky Survey, York et al. 2000; the Two Micron All Sky Survey, 2MASS, Majewski et al. 2003; and the QUEST survey, Vivas et al. 2001) evidence has been mounting for a more complex picture of the Galaxy and its formation. Unlike the smooth distribution easily captured by analytic density laws, new data argue for much more irregular substructure, especially in the stellar halo. Examples include the Sgr dwarf tidal stream in the halo (Ivezić et al. 2000; Yanny et al. 2000; Vivas et al. 2001; Majewski et al. 2003) or the Monoceros stream closer to the Galactic plane (Newberg et al. 2002; Rocha-Pinto et al. 2003). The existence of ongoing merging points to a likely significant role of accretion events in the early formation of the Milky Way’s components, making the understanding of both the distribution of merger remnants and of the Milky Way’s overall stellar content of considerable theoretical interest.

The majority (>90%) of Galactic stellar content resides in the form of main-sequence (MS) stars. However, a direct measurement of their spatial distribution requires accurate estimates of stellar distances to faint flux levels, as even the most luminous MS stars have $V \sim 15\text{--}18$ for the 1–10 kpc distance range. This requirement, combined with the need to cover a large sky area to sample a representative portion of the Galaxy, have historically made this type of measurement a formidable task.

A common workaround to the first part of the problem is to use bright tracers for which reasonably accurate distance estimates are possible (e.g., RR Lyrae stars, A-type stars, M giants) and which are thought to correlate with the overall stellar number density distribution. These tracers, however, represent only a tiny fraction of stars on the sky, and their low number density prevents tight constraints on the Galactic structure model parameters (Reid et al. 1996). For the same reason, such tracers are unsuitable tools for finding localized overdensities with small contrast ratios over their surroundings.

Preferably, given precise enough multiband photometry, one would avoid the use of tracers and estimate the distances to MS stars directly using a color–absolute magnitude, or “photometric parallax,” relation. However, until now the lack of deep, large-area optical¹⁵ surveys with sufficiently accurate multiband photometry has prevented an efficient use of this method.

Surveying a wide area is of particular importance. For example, even the largest Galactic structure-oriented data set to date to use accurate optical CCD photometry (Siegel et al. 2002) covered only $\sim 15\text{ deg}^2$, with $\sim 10^5$ stars. To recover the overall Galactic density field, their study, as others before it, has had to resort to model fitting and *assume* a high degree of regularity in the density distribution and its functional form. This, however, given that typical disk + halo models can have up to 10 free parameters,

makes parameter estimation vulnerable to bias by unrecognized clumpy substructure.

Indeed, a significant spread in results coming from different studies has existed for quite some time (e.g., Siegel et al. 2002, Table 1; Bilir et al. 2006), indicating that either the unidentified substructures are confusing the model fits, that there are a multitude of degenerate models that are impossible to differentiate from using a limited number of lines of sight, or that the usual models provide an inappropriate description of the large-scale distribution of stars in the Galaxy. A direct model-free determination of the stellar number density distribution in a large volume of the Galaxy would shed light on, and possibly resolve, all these issues.

The large area covered by the SDSS, with accurate photometric measurements ($\sim 0.02\text{ mag}$) and faint flux limits ($r < 22$), allows for a novel approach to studies of the stellar distribution in the Galaxy; using a photometric parallax relation appropriate for MS stars, we estimate distances for a large number of stars and *directly map the Galactic stellar number density* without the need for an a priori model assumption.¹⁶ In this paper, we describe a study based on ~ 48 million stars detected by the SDSS in $\sim 6500\text{ deg}^2$ of sky. An advantage of this approach is that the number density of stars as a function of color and position in the Galaxy, $\rho(X, Y, Z, r - i)$, can be measured without assuming a particular Galactic model (e.g., the luminosity function and functional forms that describe the density laws for disks and halo). Rather, with minimal assumptions about the nature of the observed stellar population (that the large majority of the observed stars are on the MS) and by using an adequate photometric parallax relation, the computed stellar number density maps can be used to get an overall picture about the distribution of stars first, and a posteriori constrain the density laws of Galactic components and look for deviations from them second.

This is the first paper, in a series of three,¹⁷ that employs SDSS data and a photometric parallax relation to map the Galaxy. Here, we focus on the stellar number density distribution. In Ivezić et al. (2008, hereafter Paper II) we discuss the distribution of photometric metallicity (calibrated using SDSS spectroscopic data), and in N. Bond et al. (2008, in preparation, hereafter Paper III), we analyze the stellar kinematics using radial velocity and proper motion measurements.

We begin by describing the SDSS data, the photometric parallax relations, and the construction of stellar number density maps in § 2. Analysis of overall trends and identification of localized density features (substructure) is described in § 3. In § 4 we use the maps to derive the best-fit parameters of the density model for the Galactic disk and stellar halo. Section 5 discusses the details of a remarkably large overdensity of stars identified in § 3. Our results and their theoretical implications are summarized and discussed in § 6.

2. DATA AND METHODOLOGY

In this section we list the basic characteristics of the SDSS imaging survey, discuss the adopted photometric parallax relation used to estimate the distance to each star, and describe a method for determining three-dimensional number density distribution as a function of Galactic coordinates.

¹⁵ For example, near-IR colors measured by the all-sky 2MASS survey are not well suited for this purpose, because they only probe the Rayleigh-Jeans tail of the stellar spectral energy distribution and thus are not very sensitive to the effective temperature.

¹⁶ The use of photometric parallax to determine Galactic model parameters is not particularly novel, having a long history going back to at least Gilmore & Reid (1983). The novelty in our approach is to use the photometric parallax and wide area of SDSS to construct stellar density distribution maps first and look for structure in the maps and fit analytic Galactic models second.

¹⁷ We credit the late J. R. R. Tolkien for demonstrating the virtues of this approach.

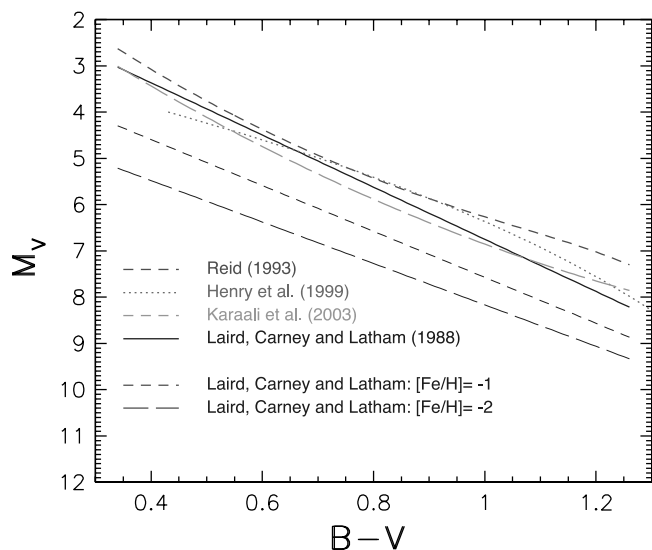


FIG. 1.—Comparison of photometric parallax relations, expressed in the Johnson system, from the literature. The relation from Henry et al. (1999) is valid for stars closer than 10 pc, while other relations correspond to the Hyades MS. Note that the latter differ by a few tenths of a magnitude. The relation from Laird et al. (1988) is also shown when corrected for two different metallicity values, as marked in the legend. The gradient $dM_V/d[Fe/H]$ given by their prescription is about 1 mag dex^{-1} at the blue end and about half this value at the red end. [See the electronic edition of the *Journal* for a color version of this figure.]

2.1. The Basic Characteristics of the SDSS Imaging Survey

The SDSS is a digital photometric and spectroscopic survey which will cover up to one quarter of the celestial sphere in the north Galactic cap and produce a smaller area ($\sim 225 \text{ deg}^2$) but much deeper survey in the southern Galactic hemisphere¹⁸ (York et al. 2000; Stoughton et al. 2002; Abazajian et al. 2003; Gunn et al. 2006; Tucker et al. 2006). The flux densities of detected objects are measured almost simultaneously in five bands ($u, g, r, i,$ and z) with effective wavelengths of 3540 Å, 4760 Å, 6280 Å, 7690 Å, and 9250 Å, respectively (Fukugita et al. 1996; Gunn et al. 1998; Smith et al. 2002; Hogg et al. 2001). The completeness of SDSS catalogs for point sources is $\sim 99.3\%$ at the bright end ($r \sim 14$, where the SDSS CCDs saturate; Ivezić et al. 2001) and drops to 95% at magnitudes¹⁹ of 22.1, 22.4, 22.1, 21.2, and 20.3 in $u, g, r, i,$ and z , respectively. All magnitudes are given on the AB_r system (Oke & Gunn 1983; for additional discussion regarding the SDSS photometric system see Fukugita et al. [1996] and Fan [1999]). The final survey sky coverage of about 8000 deg^2 will result in photometric measurements to the above detection limits for about 80 million stars and a similar number of galaxies. Astrometric positions are accurate to about $0.1''$ per coordinate for sources brighter than $r \sim 20.5 \text{ mag}$ (Pier et al. 2003), and the morphological information from the images allows robust point source–galaxy separation to $r \sim 21.5 \text{ mag}$ (Lupton et al. 2002). The SDSS photometric accuracy is 0.02 mag (rms, at the bright end), with well-controlled tails of the error distribution (Ivezić et al. 2003). The absolute zero-point calibration of the SDSS photometry is accurate to within $\sim 0.02 \text{ mag}$ (Ivezić et al. 2004b). A compendium of technical details about SDSS can be found in Stoughton et al. (2002) and on the SDSS Web site.²⁰

¹⁸ See also <http://www.astro.princeton.edu/PBOOK/welcome.htm>.

¹⁹ These values are determined by comparing multiple scans of the same area obtained during the commissioning year. Typical seeing in these observations was $1.5'' \pm 0.1''$.

²⁰ See <http://www.sdss.org>.

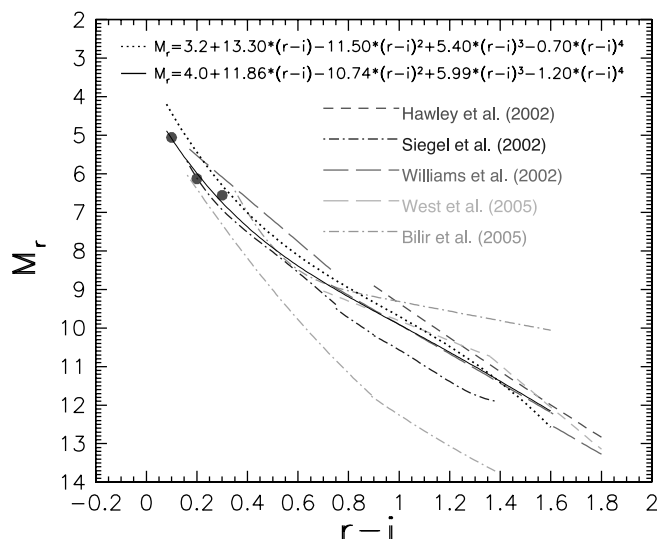


FIG. 2.—Comparison of photometric parallax relations in the SDSS $ugriz$ system from the literature and adopted in this work. The two relations adopted here are shown by the dotted (“bright” normalization) and solid (“faint” normalization) lines. Other lines show photometric parallax relations from the literature, as marked. The bottom thin line from Siegel et al. corresponds to low-metallicity stars. The large symbols show SDSS observations of globular cluster M13. [See the electronic edition of the *Journal* for a color version of this figure.]

2.2. The Photometric Parallax Method

SDSS is superior to previous optical sky surveys because of its high catalog completeness and accurate multiband CCD photometry to faint flux limits over a large sky area. The majority of stars detected by SDSS are MS stars ($\sim 98\%$; Finlator et al. 2000), which have a fairly well-defined color-luminosity relation.²¹ Thus, accurate SDSS colors can be used to estimate luminosity and, hence, distance, for each individual star. While these estimates are incorrect for a fraction of stars such as multiple systems and non-MS stars, the overall contamination is small or controllable.

There are a number of proposed photometric parallax relations in the literature. They differ in the methodology used to derive them (e.g., geometric parallax measurements, fits to globular cluster color-magnitude sequences), photometric systems, and the absolute magnitude and metallicity range for which they are applicable. Not all of them are mutually consistent, and most exhibit significant intrinsic scatter of order a half a magnitude or more. Even the relations corresponding to the same cluster, such as the Hyades, can differ by a few tenths of a magnitude (see Fig. 1).

In Figure 2 we compare several recent photometric parallax relations found in the literature. They are all based on geometric parallax measurements, but the stellar colors are measured in different photometric systems. In order to facilitate comparison, we use photometric transformations between the Johnson and SDSS systems derived for MS stars by Ivezić et al. (2007b) and fits to the stellar locus in SDSS color-color diagrams from Ivezić et al. (2004b). As is evident, different photometric parallax relations from the literature are discrepant at the level of several tenths to a magnitude. Furthermore, the relation proposed by Williams et al. (2002) is a piecewise fit to restricted color ranges and results in a discontinuous relation. The behavior of Kurucz model atmospheres suggests that these discontinuities are probably unphysical.

²¹ The uniqueness of the color-luminosity relation breaks down for stars at MS turnoff ($r-i \sim 0.11 \text{ mag}$ for disk and $r-i \sim 0.06 \text{ mag}$ for halo stars; Chen et al. 2001). Those are outside of all but the bluest bin of the $r-i$ range studied here.

We constructed a fit, shown in Figure 2, that attempts to reconcile the differences between these relations. We require a low-order polynomial fit that is roughly consistent with the three relations at the red end and properly reproduces the SDSS observations of the position of the turnoff (median $M_r = 5$ at $r - i = 0.10$) for globular cluster M13 (using a distance of 7.1 kpc; Harris 1996). The adopted relation

$$M_r = 4.0 + 11.86(r - i) - 10.74(r - i)^2 + 5.99(r - i)^3 - 1.20(r - i)^4 \quad (1)$$

is very similar to the Williams et al. (2002) relation at the red end and agrees well with the Siegel et al. (2002) relation at the blue end.

In order to keep track of uncertainties in our results due to systematic errors in the photometric parallax relation, we adopt an additional relation. The absolute magnitude difference between the two relations covers the plausible uncertainty range, and hence, the final results are also expected to bracket the truth. While we could arbitrarily shift the normalization of equation (1) for this purpose, we instead use a relation that has an independent motivation.

In Paper III, we propose a novel method to constrain the photometric parallax relation using kinematic data. The method relies on the large sky coverage by SDSS and simultaneous availability of both radial velocities and proper motion data for a large number of stars. These data can be successfully modeled using simple models such as a nonrotating halo and a disk rotational lag that is dependent only on the height above the Galactic plane. The best-fit models that are independently constrained using radial velocity and proper motion measurements agree only if the photometric parallax relation is correct. That is, the tangential velocity components, which are proportional to distance and measured proper motions, are tied to the radial velocity scale by adopting an appropriate distance scale. As a result of such kinematic analysis, we adopt a second photometric parallax relation

$$M_r = 3.2 + 13.30(r - i) - 11.50(r - i)^2 + 5.40(r - i)^3 - 0.70(r - i)^4. \quad (2)$$

This relation is 0.66 mag brighter at the blue end ($r - i = 0.1$) and matches equation (1) at $r - i = 1.38$ (see Fig. 2 for a comparison). The normalization differences between the two relations at the blue end correspond to a systematic distance scale change of $\pm 18\%$, relative to their mean.

To distinguish between the two relations, we refer to the relation from equation (1) as the “faint” normalization and to the relation from equation (2) as the “bright” normalization. We note that, encouragingly, the *Hipparcos*-based M_R versus $R - I$ relation from Reid et al. (2001) falls in between these two relations.

In the sections to follow, we perform all the analysis separately for each relation and discuss the differences in results when they are noticeable. For all figures, we use the bright normalization, unless noted otherwise.

Equations (1) and (2) are quite steep, for example, $\Delta M_r / \Delta(r - i) \sim 10$ mag/mag at the blue end ($r - i \sim 0.1$). Because of this steepness,²² very accurate photometry (0.01–0.02 mag) is required to reach the intrinsic accuracy of the photometric relation (about 0.2 mag or better for individual globular clusters; for metallicity effects see below). Older photographic surveys

²² This is not an artifact of the SDSS photometric system or the adopted photometric parallax relation. For example, even for the linear M_V vs. $B - V$ relation from Laird et al. (1988) $dM_V/d(B - V) = 5.6$ mag/mag.

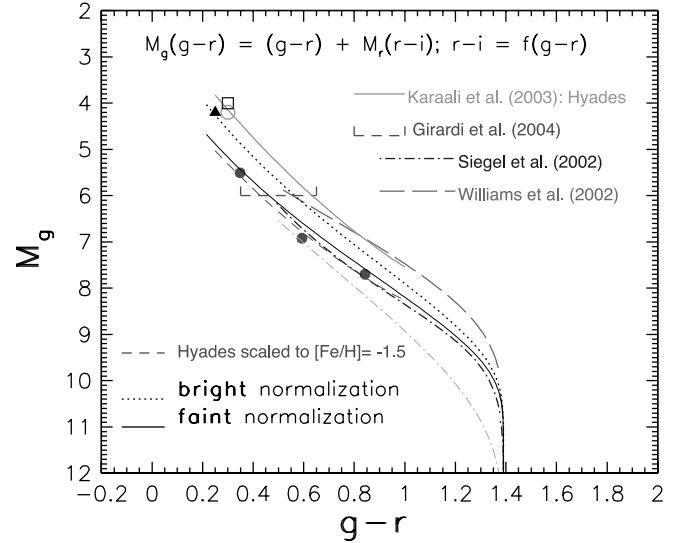


Fig. 3.—Comparison of photometric parallax relations from the literature and adopted in this work, shown using SDSS bands (stars with spectral types later than $\sim M0$ have $g - r \sim 1.4$). The two relations adopted here are shown by the dotted (“bright” normalization) and solid (“faint” normalization) lines. These are the same relations as shown in Fig. 2, translated here into the $M_g(g - r)$ form using the $r - i = f(g - r)$ relation appropriate for MS stars on the main stellar locus. Other lines show photometric parallax relations from the literature, as marked. The line marked Girardi et al. shows the range of model colors for $M_g = 6$. The bottom thin line from Siegel et al. corresponds to low-metallicity stars. The triangle, circle, and square show the SDSS observations of globular cluster Pal 5 ($[Fe/H] = -1.4$) and the Hyades ($[Fe/H] = 0.1$) and M48 ($[Fe/H] = -0.2$) open clusters, respectively. The three large dots show the SDSS observations of globular cluster M13 ($[Fe/H] = -1.5$). Note the good agreement between these observations and the Hyades sequence scaled to M13’s metallicity using the prescription from Laird et al. (1988). For reference, $B - V = 0.95(g - r) + 0.20$ to within 0.05 mag. [See the electronic edition of the *Journal* for a color version of this figure.]

have photometric errors of ~ 0.1 – 0.2 mag (Sesar et al. 2006), and inaccurate color measurements result in M_r errors exceeding ~ 1 mag. Hence, with the SDSS, the intrinsic accuracy of the photometric parallax method can be approached to a faint flux limit and over a large sky area for the first time.

2.2.1. Effects of Metallicity on the Photometric Parallax Relation

The main source of systematic errors in the photometric parallax relation is its dependence on metallicity. For example, Siegel et al. (2002) address this problem by adopting different relations for low- and high-metallicity stars (cf. Fig. 2). Another approach is to estimate metallicity, either from a spectrum or using photometric methods such as a UV excess–based δ -method (e.g., Carney 1979), and then apply a correction to the adopted photometric parallax relation that depends both on color and metallicity (e.g., Laird et al. 1988), as illustrated in Figure 1. We have tested the Laird et al. metallicity correction by scaling the Hyades MS, as given by Karaali et al. (2003) using $[Fe/H] = -1.5$ appropriate for M13, and comparing it to SDSS observations of that cluster. As shown in Figure 3, the agreement is very good (~ 0.1 mag).

An application of the δ -method to SDSS photometric system was recently attempted by Karaali et al. (2005). However, as they pointed out, their study was not based on SDSS data, and thus, even small differences between different photometric systems may have a significant effect on derived metallicities (especially since the SDSS u -band photometry is not precisely on the AB system; see Eisenstein et al. 2006).

The expected correlation of metallicity and the SDSS $u - g$ and $g - r$ colors was recently discussed by Ivezić et al. (2006).

Using SDSS photometry and metallicity estimates derived from SDSS spectra (Allende Prieto et al. 2006), they demonstrated a very strong dependence of the median metallicity on the position in the $g - r$ versus $u - g$ color-color diagram. For example, for stars at the blue tip of the stellar locus ($u - g < 1$, mostly F stars), the expression

$$[\text{Fe}/\text{H}] = 5.11(u - g) - 6.33 \quad (3)$$

reproduces the spectroscopic metallicity with an rms of only 0.3 dex. This relation shows that even in this favorable case (it is much harder to estimate metallicity for red stars), a 0.1 mag error of the $u - g$ color would introduce an error of $[\text{Fe}/\text{H}]$ as large as 0.5 dex, resulting in an error in the absolute magnitude of ~ 0.5 mag.

We aim here to study the Galaxy to as large a distance limit as the SDSS photometric sample of stars allows. While metallicity could be estimated for bright blue stars using the above expression, for most stars in the sample the SDSS u -band photometry is not sufficiently accurate to do so reliably. For example, the random error of $u - g$ color becomes 0.1 mag at $u \sim 20.5$ (Ivezić et al. 2003), which corresponds to $g \sim 19.5$ or brighter even for the bluest stars. Therefore, metallicity estimates based on the $u - g$ color would come at the expense of a more than 2 mag shallower sample. Hence, we choose not to correct the adopted photometric parallax relation for metallicity effects and only utilize the correlation between metallicity and $u - g$ color when constraining the metallicity distribution of a large halo overdensity as discussed in § 5.

We point out that the adopted relations do account for metallicity effects to some extent. The metallicity distribution shows a much larger gradient perpendicular to the Galactic plane than in the radial direction (see Fig. 3 in Ivezić et al. 2006). As we only consider high Galactic latitude data, the height above the plane is roughly proportional to distance. At the red end, the adopted relations are tied via geometric parallax to nearby metal-rich stars, and even the faintest M dwarfs in the SDSS sample are only ~ 1 kpc away. At the blue end, the adopted relations are tied to globular clusters and halo kinematics, which is appropriate for the bluest stars in the sample, which are detected at distances from several kpc to ~ 10 kpc. Thus, in some loose “mean” sense, the adopted relation smoothly varies from a relation appropriate for nearby, red, high-metallicity stars to a relation appropriate for more distant, blue, low-metallicity stars.²³ Furthermore, Reid et al. (2001) show that photometric parallax relations constructed using red photometric bands, such as our M_r versus $r - i$ relation, are much less sensitive to metallicity than the traditional M_V versus $B - V$ relation (compare the top left and bottom right panels in their Fig. 15). Nevertheless, to further control metallicity and other systematic effects, we perform our analysis in narrow color bins, as described in more detail in § 2.3.

2.2.2. A Test of the Photometric Parallax Relation Using Resolved Binary Stars

The number of close stellar pairs in the SDSS survey with distances in the $2'' - 5''$ range shows an excess relative to the extrapolation from larger distances (Sesar et al. 2008). Statistically,

²³ When the adopted photometric parallax relation is applied to the Sun ($r - i = 0.10$), the resulting absolute magnitude is too faint by about 0.5 mag. This is an expected result, because the relation is anchored to a low-metallicity globular cluster at the blue end. For both relations, the predicted absolute magnitudes of low-temperature, low-metallicity stars are systematically too bright. However, the majority of such stars (e.g., distant halo M dwarfs) are faint and well beyond the flux limit of the survey.

$\sim 70\%$ of such pairs are physically associated binary systems. Since they typically have different colors, they also have different absolute magnitudes. The difference in absolute magnitudes, ΔM , can be computed from an adopted photometric parallax relation without the knowledge of the system’s distance and should agree with the measured difference of their apparent magnitudes, Δm . The distribution of the difference, $\delta = \Delta m - \Delta M$, should be centered on zero and should not be correlated with color if the shape of the photometric parallax relation is correct (the overall normalization is not constrained, but this is not an issue since the relation can be anchored at the red end using nearby stars with geometric parallaxes).²⁴ The width of the δ -distribution provides an upper limit for the intrinsic error of the photometric parallax method (note, however, that δ is not sensitive to systematic errors due to metallicity, since the binary components presumably have the same metallicity).

We have performed such a test of adopted parallax relations using a sample of 17,000 candidate binaries from SDSS Data Release 5. Pairs of stars with $14 < r < 20$ are selected as candidate wide binaries if their angular separation is in the $3'' - 4''$ range. The brighter star (in the r band) is designated as the primary (subscript 1) and the fainter one as the secondary (subscript 2). For each pair, we calculated δ twice—once assuming the bright photometric parallax relation (eq. [2]) and once assuming the faint relation (eq. [1]). We further remove from the sample all pairs with $|\delta| > 0.5$, those likely being the interlopers and not actual physical pairs.

The results of this analysis are summarized in Figure 4. The color-coded diagrams show the dependence of δ on the $r - i$ colors of the primary and the secondary components. The median δ -value in each (r_1, r_2) pixel measures whether the absolute magnitude difference obtained using the parallax relation for stars of colors r_1 and r_2 is consistent with the difference of their apparent magnitudes (in each bin, the δ -distribution is much more peaked than for a random sample of stars and is not much affected by the $|\delta| < 0.5$ cut). If the *shape* of the photometric parallax relation is correct, the median δ should be close to zero for all combinations of r_1 and r_2 .

The distributions of the median δ for each pixel are fairly narrow (~ 0.1 mag) and centered close to zero (the medians are 0.07 mag for the bright relation and -0.004 mag for the faint relation). Irrespective of color and the choice of photometric parallax relation, the deviations are confined to the $\sim \pm 0.25$ mag range, thus placing a stringent upper limit on the errors in the shape of the adopted relations. The δ -distribution rms width of ~ 0.1 mag implies an average distance error of about 5%. Nevertheless, the binary stars in a candidate pair are of presumably identical metallicities. As a large fraction of the intrinsic scatter of $M_r(r - i)$ comes from the dependence of absolute magnitude on metallicity, we adopt a conservative value of $\sigma_{M_r} = 0.3$.

The coherent deviations seen in Figure 4 (e.g., around $r_1 \sim 0.3$ and $r_2 \sim 0.5$) indicate that the adopted parallax relations could be improved. Given the already satisfactory accuracy of the adopted relations, such a study is presented separately (Sesar et al. 2008).

2.2.3. Contamination by Giants

The photometric parallax method is not without pitfalls, even when applied to the SDSS data. Traditionally, the application of this method was prone to significant errors due to sample contamination by evolved stars (subgiants and giants, hereafter giants for simplicity) and their underestimated distances. This effect is

²⁴ Note the similarities of this method and the method of reduced proper motions (Luyten 1968).

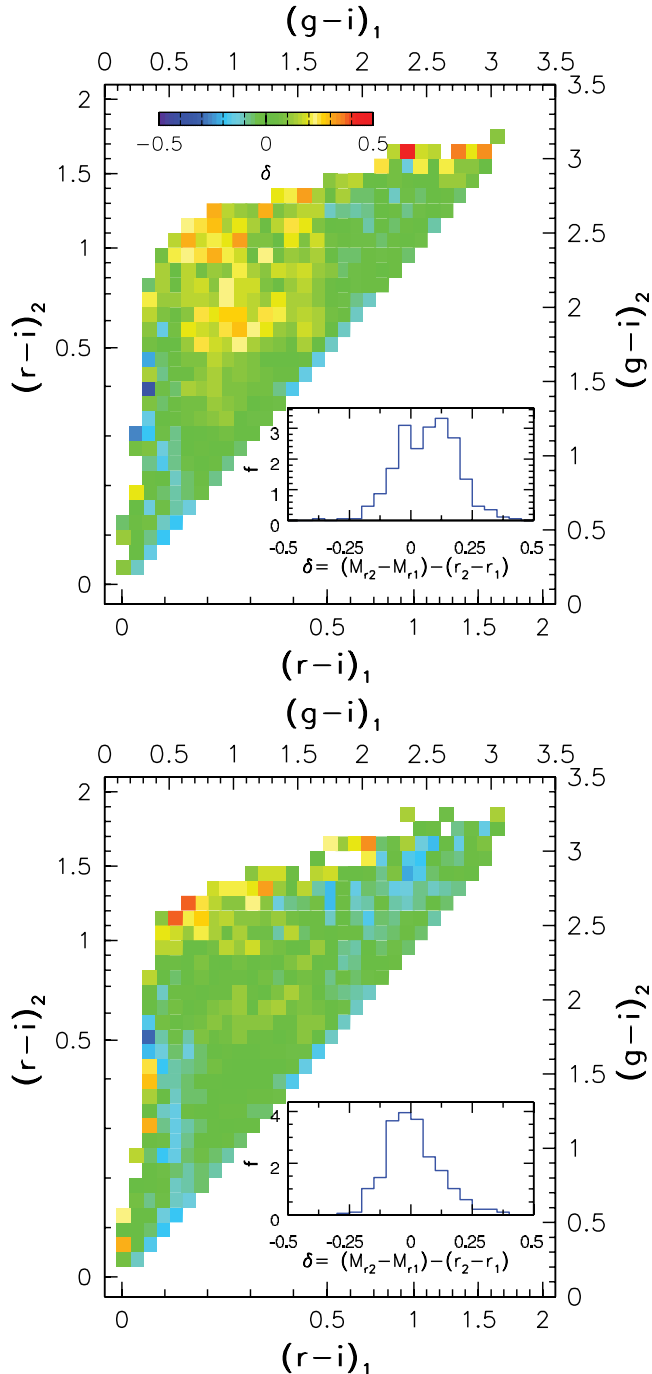


FIG. 4.—Distribution of the median δ for a sample of $\sim 17,000$ candidate wide-angle binaries in the $(r-i)_1$ (color of brighter pair member; the primary) vs. $(r-i)_2$ (color of fainter member; the secondary) color-color diagram. Here, $\delta = (M_{r,2} - M_{r,1}) - (r_2 - r_1)$ is the difference of two estimates (one from the absolute and the other from the apparent magnitude) of brightness difference between the two components. In the top panel, the absolute magnitudes were estimated using eq. (2) (the “bright” parallax relation; the dotted line in Fig. 2) and, in the bottom panel, using eq. (1) (the “faint” parallax relation; the solid line in Fig. 2). Inset histograms show the distribution of the median δ evaluated for each color-color pixel. The distribution medians are 0.07 (top) and -0.004 (bottom), and the dispersions (determined from the interquartile range) are 0.13 and 0.10 mag, respectively.

also present in this study, but at a much less significant level because of the faint magnitudes probed by SDSS. At these flux levels, the distances corresponding to giants are large and sometimes even beyond the presumed edge of the Galaxy (up to ~ 100 kpc). The stellar density at these distances is significantly smaller than at

distances corresponding to MS stars with the same apparent magnitude. The contamination with evolved stars rapidly asymptotes (e.g., assuming a $\sim r^{-3}$ halo profile) and may decline when the edge of the halo is reached.

A quantitative illustration of this effect is shown in Figure 5 for a fiducial Galaxy model. The worst case scenario corresponds to G giants with $g-r \sim 0.4-0.5$ and $r-i \sim 0.15-0.20$, and their most probable fraction is about 5%. This color range and the fraction of giants was determined using the SDSS data for the globular cluster M13 (the data for the globular cluster Pal 5 imply similar behavior). To be conservative, we have also tested a model with a twice as large fraction of giants. This analysis (see Fig. 5, bottom) shows that the effect of misidentifying giants as MS stars is an overall bias in estimated number density of $\sim 4\%$ ($\sim 8\%$ when the fraction of giants is 10%), with little dependence on distance from the Galactic plane beyond 500 pc. This is the distance range probed by blue stars, and thus, the worst effect of contamination by giants is a small overall overestimate of the density normalization. Shorter distances are probed by redder stars, M dwarfs, for which the contamination by M giants is negligible, because the luminosity difference between red giants and dwarfs is very large (e.g., there are tens of millions of M dwarfs in our sample, while the 2MASS survey revealed only a few thousand M giants in the same region of the sky; Majewski et al. 2003). Hence, the misidentified giants are not expected to significantly impact our analysis.

2.2.4. Unrecognized Multiplicity

Multiplicity may play a significant role by systematically making unresolved multiple systems, when misidentified as a single star, appear closer than they truly are. The net effect of unrecognized multiplicity on derived distance scales, such as scale height and scale length, is to underestimate them by up to $\sim 35\%$ (see § 4.3.4 here and Siegel et al. 2002). The magnitude of this bias is weakly dependent on the actual composition of the binaries (e.g., their color difference and luminosity ratio), but dependent on the fraction of multiple systems in the Galaxy. Since this fraction is not well constrained, for the purpose of constructing the number density maps (§ 2.4) we assume all observed objects are single stars. This biases the distance scales measured off the maps, making them effectively lower limits, and we a posteriori correct for it, after making the Galactic model fits (§§ 4.3.4 and 4.3.11). Note that this bias cannot affect the shapes of various density features seen in the maps, unless the properties of multiple systems vary greatly with the position in the Galaxy.

2.2.5. Distance Range Accessible to SDSS Observations of Main-Sequence Stars

A disadvantage of this method is its inability, when applied to MS stars, to probe distances as large as those probed by RR Lyrae and M giants (20 kpc vs. 100 kpc). However, a significant advantage of using MS stars is the vastly larger number of stars (the number ratio of MS to RR Lyrae stars in the SDSS sample is $\sim 10,000$ and even larger for M giants; Ivezić et al. 2003, 2004d, 2005). This large number of MS stars allows us to study their number density distribution with a high spatial resolution and without being limited by Poisson noise in a large fraction of the observed volume.

2.3. The SDSS Stellar Sample

In this section we describe the stellar sample utilized in this work and the methods used to construct the three-dimensional number density maps.

2.3.1. *The Observations*

We utilize observations from 248 SDSS imaging runs obtained in a five year period through 2003 September, which cover 6538 deg^2 of the sky. This is a superset of imaging runs described in SDSS Data Release 3 (Abazajian et al. 2005), complemented by a number of runs from SDSS Data Release 4 (Adelman-McCarthy et al. 2006) and the so-called Orion runs (Finkbeiner et al. 2004). The sky coverage of these 248 runs is shown in Figure 6. They cover 5450 deg^2 in the northern Galactic hemisphere and 1088 deg^2 in the south.

We start the sample selection with 122 million detections classified as point sources (stars) by the SDSS photometric pipeline, *Photo* (Lupton et al. 2002). For a star to be included in the starting sample, we require that $r < 22$ and that it is also detected (above 5σ) in at least the g or i band. The latter requirement is necessary to be able to compute either the $g - r$ or $r - i$ color. The two requirements reduce the sample to 87 million observations. For each magnitude measurement, *Photo* also provides a fairly reliable estimate of its accuracy (Ivezić et al. 2003), hereafter σ_g , σ_r , and σ_i . We correct all measurements for the interstellar dust extinction using the Schlegel et al. (1998, hereafter SFD98) maps.

2.3.2. *The Effects of Errors in Interstellar Extinction Corrections*

The SFD98 maps are believed to be correct within 10% or better. This uncertainty plays only a minor role in this work because the interstellar extinction is fairly small at the high Galactic latitudes analyzed here ($|b| > 25$): the median value of the extinction in the r band, A_r , is 0.08, with 95% of the sample with $A_r < 0.23$ and 99% of the sample with $A_r < 0.38$. Thus, only about 5% of stars could have extinction correction uncertain by more than the photometric accuracy of SDSS data ($\sim 0.02 \text{ mag}$). The SFD98 maps do not provide the wavelength dependence of the interstellar correction, only its magnitude. The extinction corrections in the five SDSS photometric bands are computed from the SFD98 maps using conversion coefficients derived from an $R_V = 3.1$ dust model. Analysis of the position of the stellar locus in the SDSS color-color diagrams suggests that these coefficients are satisfactory at the level of accuracy and galactic latitudes considered here (Ivezić et al. 2004b).

We apply full SFD98 extinction correction to all stars in the sample. This is inappropriate for the nearest stars because they are not beyond all the dust. Distances to the nearest stars in our sample, those with $r - i = 1.5$ (the red limit) and $r \sim 14$ (approximately the SDSS r -band saturation limit), are $\sim 30 \text{ pc}$ (distance determination is described in the next two sections). Even when these stars are observed at high galactic latitudes, it is likely that they are overcorrected for the effects of interstellar extinction. To estimate at what distances this effect becomes important, we have examined the dependence of the $g - r$ color on apparent magnitude for red stars, selected by the condition $r - i > 0.9$, in the region defined by $210 < l < 240$ and $25 < b < 30$. The distribution of the intrinsic $g - r$ color for these stars is practically independent of their $r - i$ color (see Fig. 8), with a median of 1.40 and a standard deviation of only 0.06 mag (Ivezić et al. 2004b). This independence allows us to test at what magnitude (i.e., distance) the applied SFD98 extinction corrections become an overestimate, because in such a case, they result in $g - r$ colors that are bluer than the expected value of ~ 1.40 . We find that for $r > 15$ the median $g - r$ color is nearly constant—it varies by less than 0.02 mag over the $15 < r < 20$ range. On the other hand, for stars with $r < 15$ the median $g - r$ color becomes much bluer—at $r = 14.5$ the median value is 1.35. This demonstrates that stars

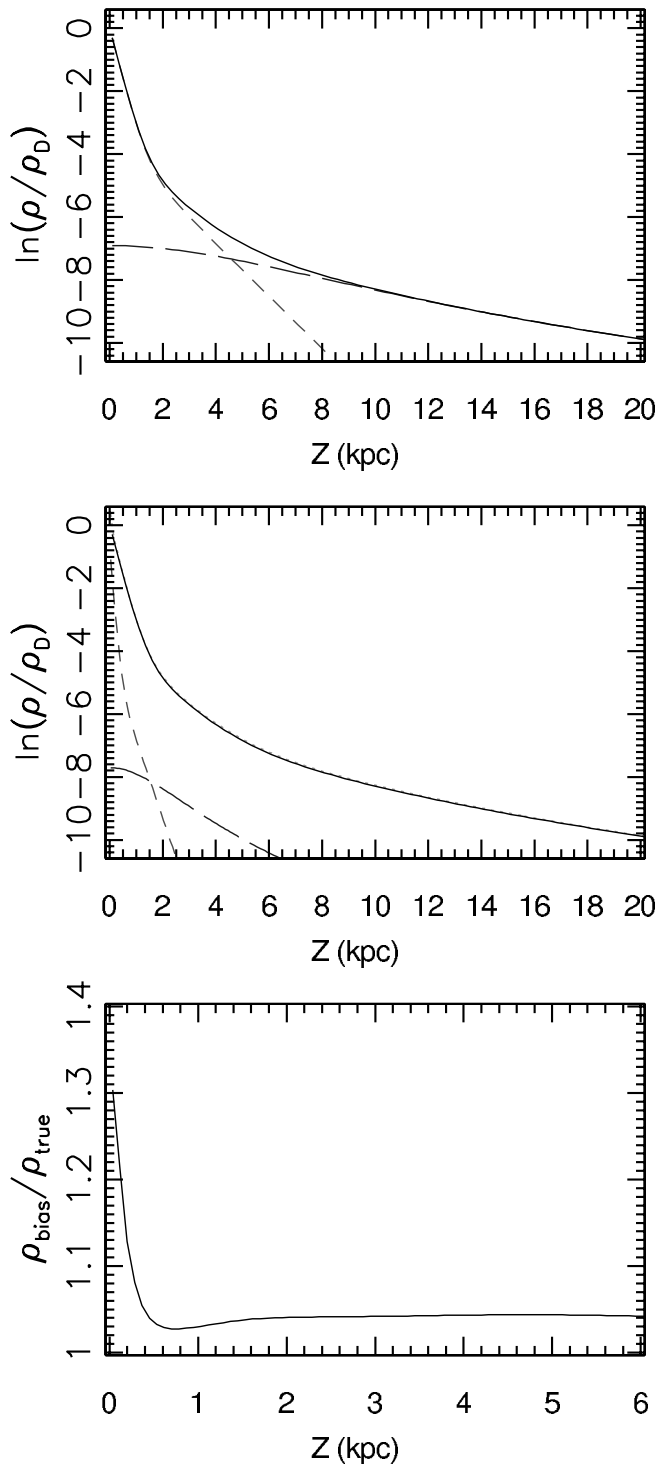


FIG. 5.—Illustration of the effects of misidentifying giants as MS stars. The top panel shows the Z -dependence of stellar density at $R = 8 \text{ kpc}$ for a fiducial model consisting of two disks with scale heights of 300 and 1200 pc. The contribution of the disks is shown by the short-dashed line, and the long-dashed line shows the contribution of a power-law spherical halo with the power-law index of 3. The middle panel shows the contribution of misidentified giants from disks (short-dashed line) and halo (long-dashed line) for an assumed giant fraction of 5% and underestimated distances by a factor of 3. The “contaminated” model is shown by dotted line, just above the solid line, which is the same as the solid line in the top panel. The ratio of the “contaminated” to true density is shown in the bottom panel (note the different horizontal scale). [See the electronic edition of the *Journal* for a color version of this figure.]

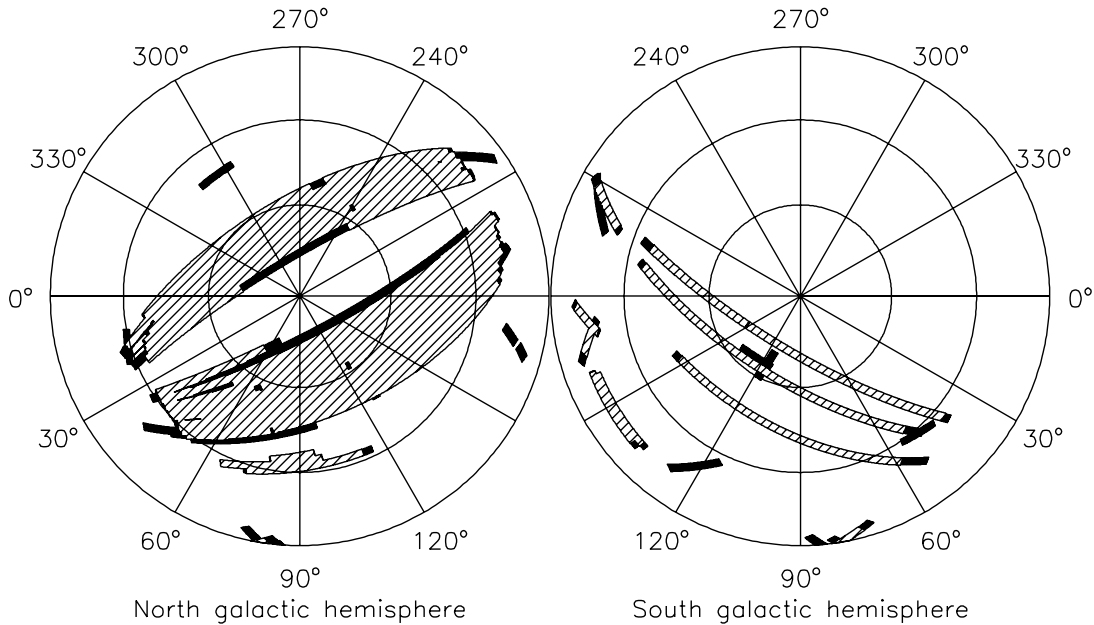


FIG. 6.—Footprint on the sky of SDSS observations used in this work shown in Lambert equal area projection (*hatched region*). The circles represent contours of constant Galactic latitude, with the straight lines showing the location of constant Galactic longitude. For this study, observations from 248 SDSS imaging runs were used, obtained over the course of 5 yr. The data cover 5450 deg^2 of the north Galactic hemisphere and a smaller but more frequently sampled area of 1088 deg^2 in the southern Galactic hemisphere.

at $r > 15$ are already behind most of the dust column. With the median $r - i$ color of 1.17, the implied distance corresponding to $r = 15$ is ~ 80 pc. For the probed galactic latitude range, this indicates that practically all the dust is confined to a region within ~ 70 pc from the galactic midplane (here we define midplane as a plane parallel to the galactic plane that has $Z = -25$ pc, because the Sun is offset from the midplane toward the north Galactic pole (NGP) by ~ 25 pc; for more details see below). We arrive to the same conclusion about the dust distribution when using an analogous sample in the south galactic plane with $|b| \sim 12$ (in this case the median $g - r$ color is systematically bluer for $r < 19$, due to different projection effects and the Sun's offset from the midplane). Hence, in order to avoid the effects of overestimated interstellar extinction correction for the nearest stars, we exclude stars that are within 100 pc from the galactic plane when fitting galaxy models (described below). Only 0.05% of stars in the sample are at such distances. In summary, the effects of overestimated interstellar extinction correction, just as the effects of contamination by giants, are not very important due to the faint magnitude range probed by SDSS.

2.3.3. The Treatment of Repeated Observations

SDSS imaging data are obtained by tracking the sky in six parallel scan lines, each $13.5'$ wide. The six scan lines from two runs are then interleaved to make a filled stripe. Because of the scan overlaps and because of the convergence of the scans near the survey poles, about 40% of the northern survey is surveyed at least twice. In addition, the southern survey areas will be observed dozens of times to search for variable objects and, by stacking the frames, to push the flux limit deeper. For these reasons, a significant fraction of measurements are repeated observations of the same stars.

We positionally identify observations as corresponding to the same object if they are within $1''$ of each other (the median SDSS seeing in the r band is $1.4''$). Out of the initial ~ 122 million observations, the magnitude cuts and positional matching produce a catalog of 47.7 million unique stars (the “star catalog,”

Table 1). They span the MK spectral types from $\sim F9$ to $\sim M3$ (Table 2). There are two or more observations for about 36% (17.2 million) of observed stars. For stars with multiple observations we take the catalog magnitude of the star to be equal to the weighted mean of all observations. In this step there is a tacit

TABLE 1
REPEAT OBSERVATION STATISTICS

N_{app}	$N(r < 22)$	$N(r < 21.5)$
1.....	30543044	2418472
2.....	11958311	1072235
3.....	3779424	3471972
4.....	856639	785711
5.....	220577	199842
6.....	105481	93950
7.....	141017	132525
8.....	43943	40065
9.....	59037	57076
10.....	15616	15002
11.....	1522	1273
12.....	2012	1772
13.....	2563	2376
14.....	1776	1644
15.....	1864	1741
16.....	3719	3653
17.....	1281	1253
N_{stars}	47737826	39716935
N_{obs}	73194731	62858036

NOTES.—Repeat observations in the stellar sample. Because of partial imaging scan overlaps and the convergence of scans near survey poles, a significant fraction of observations are repeated observations of the same stars. In columns $N(r < 22)$ and $N(r < 21.5)$, we show the number of stars observed N_{app} times for stars with average magnitudes less than $r = 22$ and $r = 21.5$, respectively. The bottom two rows list the total number of stars in the samples and the total number of observations.

TABLE 2
NUMBER DENSITY DISTRIBUTION MAPS

NUMBER	$r_{i0} - r_{i1}$	N_{stars} ($\times 10^6$)	$\langle gr \rangle$	SpT	BRIGHT		FAINT	
					\tilde{M}_r	$D_0 - D_1(dx)$	\tilde{M}_r	$D_0 - D_1(dx)$
1.....	0.10–0.15	4.2	0.36	~F9	4.69	1306–20379 (500)	5.33	961–15438 (500)
2.....	0.15–0.20	3.8	0.48	F9–G6	5.20	1021–16277 (400)	5.77	773–12656 (400)
3.....	0.20–0.25	2.8	0.62	G6–G9	5.67	816–13256 (400)	6.18	634–10555 (400)
4.....	0.25–0.30	2.0	0.75	G9–K2	6.10	664–10989 (300)	6.56	529–8939 (300)
5.....	0.30–0.35	1.5	0.88	K2–K3	6.49	551–9259 (200)	6.91	448–7676 (200)
6.....	0.35–0.40	1.3	1.00	K3–K4	6.84	464–7915 (200)	7.23	384–6673 (200)
7.....	0.40–0.45	1.2	1.10	K4–K5	7.17	397–6856 (200)	7.52	334–5864 (200)
8.....	0.45–0.50	1.1	1.18	K5–K6	7.47	344–6008 (150)	7.79	293–5202 (150)
0.....	0.50–0.55	1.0	1.25	K6	7.74	301–5320 (150)	8.04	260–4653 (150)
10.....	0.55–0.60	0.9	1.30	K6–K7	8.00	267–4752 (150)	8.27	233–4191 (150)
11.....	0.60–0.65	0.8	1.33	K7	8.23	238–4277 (100)	8.49	210–3798 (100)
12.....	0.65–0.70	0.8	1.36	K7	8.45	214–3874 (100)	8.70	190–3458 (100)
13.....	0.70–0.80	1.4	1.38	K7–M0	8.76	194–3224 (75)	9.00	173–2897 (100)
14.....	0.80–0.90	1.4	1.39	M0–M1	9.15	162–2714 (60)	9.37	145–2450 (60)
15.....	0.90–1.00	1.3	1.39	M1	9.52	136–2291 (50)	9.73	122–2079 (50)
16.....	1.00–1.10	1.3	1.39	M1–M2	9.89	115–1925 (50)	10.09	104–1764 (50)
17.....	1.10–1.20	1.3	1.39	M2–M3	10.27	96–1600 (40)	10.45	88–1493 (40)
18.....	1.20–1.30	1.1	1.39	M3	10.69	80–1306 (30)	10.81	74–1258 (30)
19.....	1.30–1.40	0.9	1.39	M3	11.16	65–1043 (25)	11.18	63–1056 (25)

NOTES.—The number density map parameters. Each of the 19 maps is a volume-limited three-dimensional density map of stars with $r_{i0} < r - i < r_{i1}$, corresponding to MK spectral types and mean $g - r$ listed in columns SpT and $\langle gr \rangle$, respectively. Median absolute magnitude \tilde{M}_r , distance limits $D_0 - D_1$ (in parsecs), and binning pixel scale dx (also in parsecs) are given in columns labeled “Bright” and “Faint”, for the bright (eq. [2]) and faint (eq. [1]) photometric parallax relation. The number of stars in each $r - i$ bin is given in N_{stars} column (in millions).

assumption that the variability is not important, justified by the MS nature of the stellar sample under consideration (for the variability analysis of the SDSS stellar sample, see Sesar et al. 2006).

As discussed in § 2.2, an accurate determination of stellar distances by photometric parallax hinges on a good estimate of the stellar color and magnitude. In the bottom panel of Figure 7 we show the mean r magnitude error of stars in the catalog as a function of the r -band magnitude. The photometric errors are ~ 0.02 mag for bright objects (limited by errors in modeling the point-spread function) and steadily increase toward the faint end due to the photon noise. At the adopted sample limit, $r = 22$, the r -band photometric errors are ~ 0.15 mag. The g - and i -band magnitude errors display similar behavior as the r band.

2.3.4. Maximum Likelihood Estimates of True Stellar Colors

The photometric parallax relation (eqs. [1] and [2]) requires only the knowledge of $r - i$ color to estimate the absolute magnitude. The accuracy of this estimate deteriorates at the faint end due to increased $r - i$ measurement error. It also suffers for blue stars ($r - i < 0.2$) of all magnitudes, because the slope, $\Delta M_r / \Delta(r - i)$, is quite large at the blue end—for these stars it would be better to use the $g - r$ (or $u - g$) color to parameterize the photometric parallax relation. On the other hand, the $g - r$ color is constant for stars later than $\sim M0$ ($g - r \sim 1.4$) and cannot be used for this purpose. These problems can be alleviated to some extent by utilizing the fact that colors of MS stars form a very narrow, nearly one-dimensional locus.

The $r - i$ versus $g - r$ color-color diagram of stars used in this work is shown in Figure 8. We find that the stellar locus is well described by the relation

$$g - r = 1.39 \{ 1 - \exp[-4.9(r - i)^3 - 2.45(r - i)^2 - 1.68(r - i) - 0.050] \}, \quad (4)$$

which is shown by the solid line in the figure.

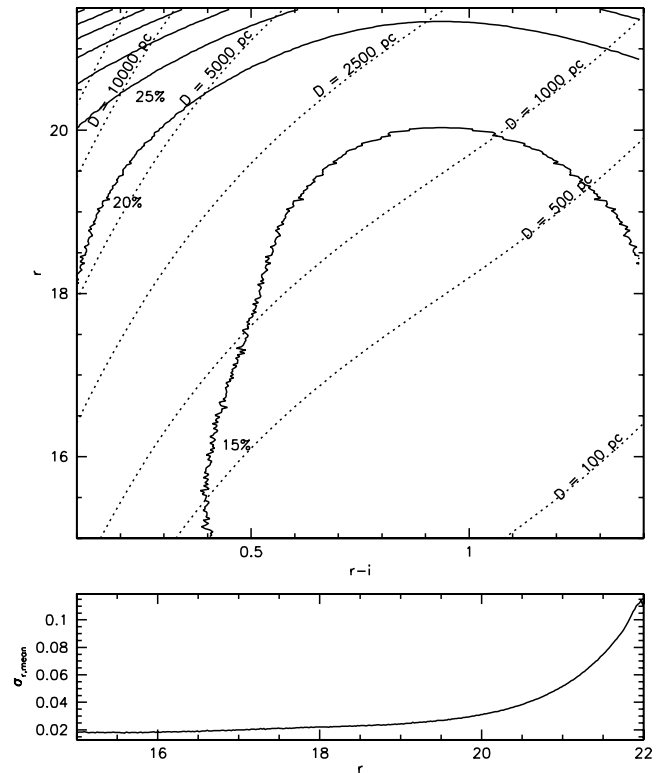


FIG. 7.—Top: Mean fractional distance error as a function of the $r - i$ color and r -band magnitude, assuming the intrinsic photometric parallax relation scatter of $\sigma_{M_r} = 0.3$ mag. The solid lines are contours of constant fractional distance error, starting with $\sigma_D/D = 15\%$ (bottom right) and increasing in increments of 5% toward the top left corner. The dotted lines are contours of constant distance and can be used to quickly estimate the distance errors for an arbitrary combination of color and magnitude/distance. Fractional distance errors are typically smaller than $\sim 20\%$. Note that the distance errors act as a σ_{M_r} wide convolution kernel in magnitude space and leave intact structures larger than the kernel scale. In particular, they have little effect on the slowly varying Galactic density field and the determination of Galactic model parameters.

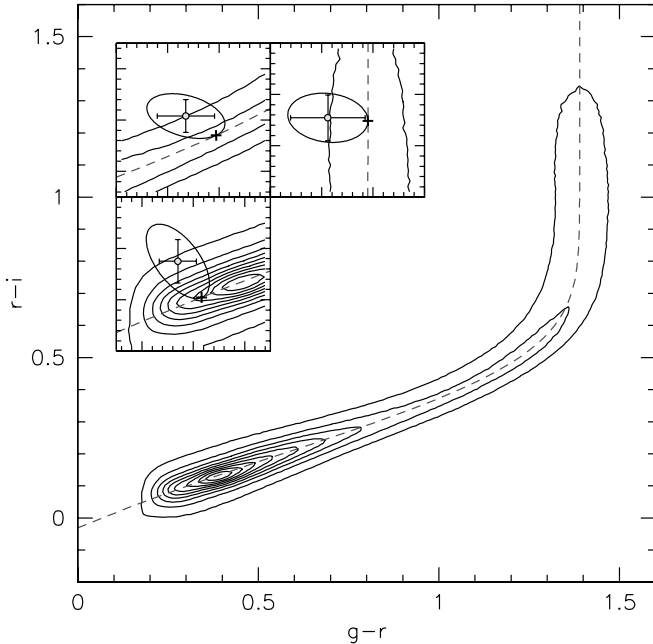


FIG. 8.—Distribution of ~ 48 million stars analyzed in this work in the $r-i$ vs. $g-r$ color-color diagram, shown by isodensity contours. Most stars lie on a narrow locus, shown by the dashed line, whose width at the bright end is 0.02 mag for blue stars ($g-r \lesssim 1$) and 0.06 mag for red stars ($g-r \sim 1.4$). The insets illustrate the maximum likelihood method used to improve color estimates; the ellipses show measurement errors, and the crosses are the color estimates obtained by requiring that a star lies exactly on the stellar locus. Note that the principal axes of the error ellipses are not aligned with the axes of the color-color diagram, because both colors include the r -band magnitude. [See the electronic edition of the *Journal* for a color version of this figure.]

The intrinsic width of the stellar locus is 0.02 mag for blue stars and 0.06 mag for red stars (Ivezić et al. 2004b), which is significantly smaller than the measurement error at the faint end. To a very good approximation, any deviation of observed colors from the locus can be attributed to photometric errors. We use this assumption to improve estimates of true stellar colors and apparent magnitudes at the faint end and thus *to increase the sample effective distance limit by nearly a factor of 2*.

As illustrated in Figure 8, for each point and a given error probability ellipse, we find a point on the locus with the highest probability²⁵ and adopt the corresponding $(g-r)_e$ and $(r-i)_e$ colors. The error ellipse is not aligned with the $g-r$ and $r-i$ axes, because the $g-r$ and $r-i$ errors are correlated ($\sigma_{g-r, r-i}^2 = \sigma_{g,r}^2 + \sigma_{g,-i}^2 + \sigma_{-r,r}^2 + \sigma_{-r,-i}^2 = -\sigma_r^2$).

We exclude all points further than 0.3 mag from the locus, as such large deviations are inconsistent with measurement errors and, in most cases, indicate the source is not a MS star. This requirement effectively removes hot white dwarfs (Kleinman et al. 2004), low-redshift quasars ($z < 2.2$; Richards et al. 2002), and white dwarf/red dwarf unresolved binaries (Smolčić et al. 2004).

Using the maximum likelihood colors, we estimate the magnitudes (g_e, r_e, i_e) by minimizing

$$\chi^2 = \frac{(r-r_e)^2}{\sigma_r^2} + \frac{(g-g_e)^2}{\sigma_g^2} + \frac{(i-i_e)^2}{\sigma_i^2}, \quad (5)$$

²⁵ This is effectively a Bayesian maximum likelihood procedure with the assumption of a uniform prior along the one-dimensional locus. As seen from Fig. 8, the real prior is not uniform. We have tested the effects of nonuniform priors. Adopting an observationally determined (from Fig. 8) nonuniform prior would change the loci of posterior maxima by only ~ 0.005 mag (worst case), while further complicating the maximum likelihood procedure. We therefore retain the assumption of a uniform prior.

which results in

$$r_e = \frac{w_r r + w_g [g - (g-r)_e] + w_i [i + (r-i)_e]}{w_r + w_g + w_i}, \quad (6)$$

$$g_e = (g-r)_e + r_e, \quad (7)$$

$$i_e = (r-i)_e - r_e, \quad (8)$$

where $w_j = 1/\sigma_j^2$ for $j = g, r, i$.

The adopted $(r-i)_e$ color and r_e magnitude uniquely determine (through eqs. [1] and [2]) the absolute magnitude M_r for each star in the catalog. We dub this procedure a “locus projection” method and refer to the derived colors as “locus-projected colors.” In all subsequent calculations we use these “locus-projected” colors, unless explicitly stated otherwise. This method is the most natural way to make use of all available color information and performs well in cases where the measurement of one color is substantially worse than the other (or even nonexistent). It not only improves the color estimates at the faint end, but also helps with debiasing the estimate of density normalization in regions of high gradients in the $(g-r, r-i)$ color-color diagram (e.g., near turnoff). This and other aspects of locus projection are further discussed in Appendix A.

2.3.5. The Contamination of Stellar Counts by Quasars

The stellar samples selected using the $g-r$ and $r-i$ colors, as described above, are contaminated by low-redshift quasars. While easily recognizable with the aid of $u-g$ color, a significant fraction of quasars detected by SDSS have the $g-r$ and $r-i$ colors similar to those of turnoff stars. The SDSS sample of spectroscopically confirmed quasars is flux-limited at $i = 19.1$ (Richards et al. 2002 and references therein), and thus, it is not deep enough to assess the contamination level at the faint end relevant here. Instead, we follow analysis from Ivezić et al. (2004a), who were interested in the contamination of quasar samples by stars, and obtain an approximate contamination level by comparing the counts of faint blue stars and photometrically selected quasar candidates. We use a catalog of co-added photometry based on about 10 repeated SDSS observations recently constructed by Ivezić et al. (2007a). The catalog covers a 300 deg² large sky region at high galactic latitudes ($|b| \sim 60^\circ$), and thus, the estimated contamination fraction represents an upper limit. With its significantly improved $u-g$ color measurements relative to single SDSS scans, this catalog allows efficient photometric selection of low-redshift quasar candidates to flux levels below $r = 21$.

As summarized in Figure 9, the largest contamination of the stellar sample by quasars is expected in blue bins. The bluest bin ($0.10 < r-i < 0.15$) includes stars with $0.2 < g-r < 0.5$, and $\sim 5\%$ of sources in the $r < 21.5$ subsample have $u-r < 0.8$, consistent with quasars. Even if we restrict the sample to $0.2 < g-r < 0.3$ and, thus, maximize the sample contamination by quasars, the estimated fraction of quasars does not exceed 10% for $r < 21.5$ (see Fig. 9, *bottom right*).

2.3.6. Estimation of Distances

Given the photometric parallax relations, the locus-projected maximum likelihood r -band magnitude, and $r-i$ color, it is straightforward to determine the distance D to each star in the catalog using

$$D = 10^{(r-M_r)/5+1} \text{ pc}. \quad (9)$$

Depending on color and the chosen photometric parallax relation, for the magnitude range probed by our sample ($r = 15-21.5$) the distance varies from ~ 100 pc to ~ 20 kpc.

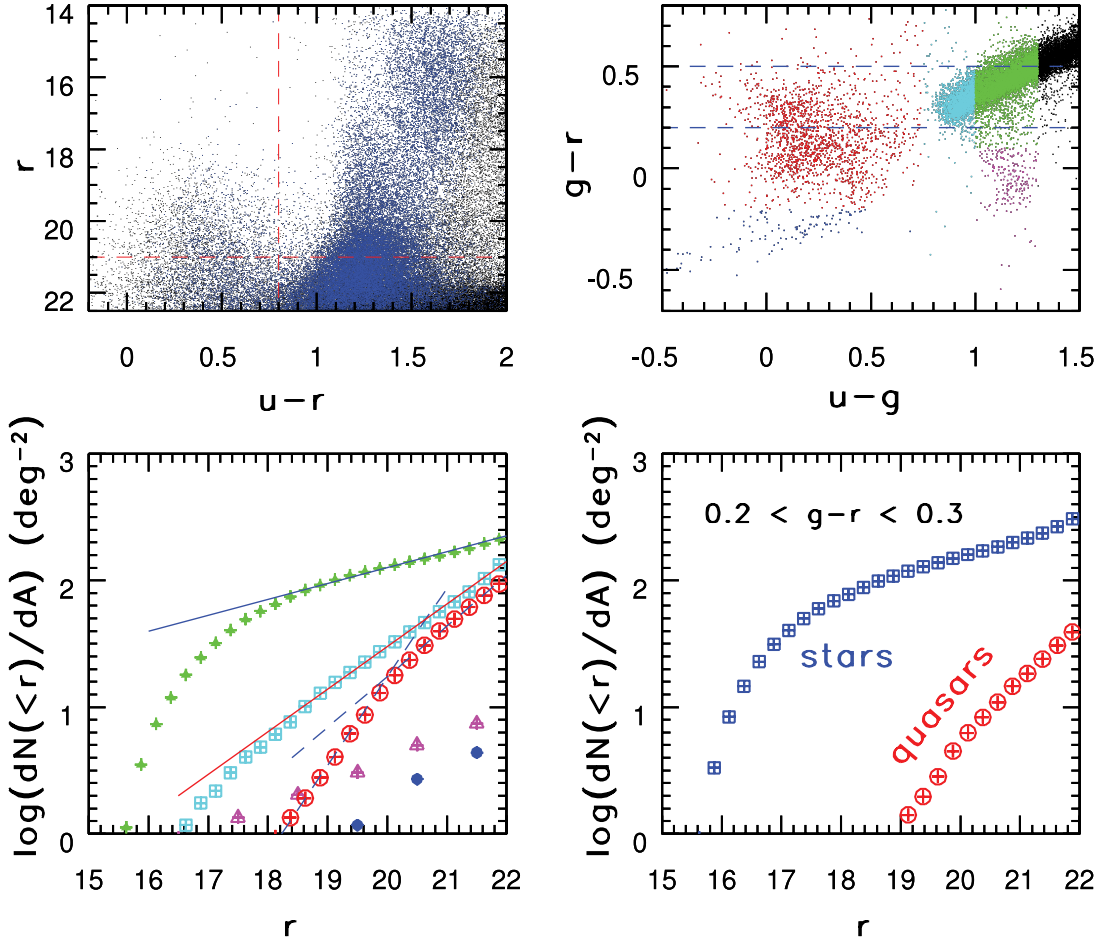


FIG. 9.— Point sources from the SDSS Stripe 82 catalog of co-added observations in the r vs. $u-r$ color-magnitude diagram are shown by the dots in the top left panel. Sources with $0.3 < g-r < 0.5$ are marked blue. Sources with $u-r < 0.8$ are dominated by low-redshift quasars, those with $u-r \sim 1.3$ by low-metallicity halo stars, and the bright stars ($r < 18$) with $u-r \sim 1.6$ are dominated by thick disk stars. Note the remarkable separation of halo and disk stars both in magnitude (a distance effect) and color (a metallicity effect) directions. The top right panel shows a subset of sources with $r < 21$ in the $g-r$ vs. $u-g$ color-color diagram. Cumulative counts of sources from several regions of this diagram (*blue*: hot stars, dominated by white dwarfs; *red*: quasars; *magenta*: blue horizontal branch stars; *cyan*: halo stars; *green*: thick disk stars) are shown in the bottom left panel, with the same color coding. The solid lines have slopes of 0.13 (*blue*) and 0.34 (*red*) for thick disk and halo stars, while the quasar counts change slope at $r \sim 20$ from ~ 0.7 to ~ 0.4 , as indicated by the dashed lines. The bottom right panel compares cumulative counts of two subsets of sources with $0.2 < g-r < 0.3$ that are separated by the $u-r = 0.8$ condition. The fraction of $u-r < 0.8$ sources is $\sim 10\%$ for $r < 21.5$ and $\sim 34\%$ for $21.5 < r < 22$.

Due to photometric errors in color, magnitude, and the intrinsic scatter of the photometric parallax relation, the distance estimate has an uncertainty, σ_D , given by

$$\sigma_{M_r(r-i)}^2 = \left[\frac{\partial M_r}{\partial(r-i)} \right]^2 \sigma_{r-i}^2 + \sigma_{M_r}^2, \quad (10)$$

$$\sigma_D^2 = \left(\frac{\partial D}{\partial M_r} \right)^2 \sigma_{M_r(r-i)}^2 + \left(\frac{\partial D}{\partial r} \right)^2 \sigma_r^2, \quad (11)$$

where σ_{M_r} is the intrinsic scatter in the photometric parallax relation. With an assumption of $\sigma_{r-i}^2 \approx 2\sigma_r^2$, this reduces to a simpler form,

$$\frac{\sigma_D}{D} = 0.46 \sqrt{\left\{ 1 + 2 \left[\frac{\partial M_r}{\partial(r-i)} \right]^2 \right\} \sigma_r^2 + \sigma_{M_r}^2}. \quad (12)$$

The fractional distance error, σ_D/D , is a function of color, apparent magnitude, and magnitude error (which itself is a function of apparent magnitude). In the top panel in Figure 7 we show the expected σ_D/D as a function of r and $r-i$ with an assumed in-

trinsic photometric relation scatter of $\sigma_{M_r} = 0.3$ mag. This figure is a handy reference for estimating the distance accuracy at any location in the density maps we introduce in § 2.4. For example, a star with $r-i = 0.5$ and $r = 20$ (or, using eq. [2], at a distance of $D = 3$ kpc) has an $\sim 18\%$ distance uncertainty. Equivalently, when the stars are binned to three-dimensional grids to produce density maps (§ 2.4), this uncertainty gives rise to a nearly Gaussian kernel smoothing the maps in the radial direction, with color- and distance-dependent variance σ_D^2 . Note that this convolution leaves intact structures larger than the kernel scale and, in particular, has little effect on the slowly varying Galactic density field and determination of Galactic model parameters (§ 4.3.3).

To summarize, due to measurement errors and uncertainty in the absolute calibration of the adopted photometric parallax relations, the derived density maps, described below, will differ from the true stellar distribution. First, in the radial direction the spatial resolution is degraded due to the smoothing described above. A similar effect is produced by misidentification of binaries and multiple systems as single stars, the distance scale may have systematic errors, probably color and metallicity dependent, that “stretch or shrink” the density maps. Third, for a small fraction of stars, the distance estimates may be grossly incorrect due to

contamination by giants and multiple unresolved systems. Finally, stars with metallicities significantly different than assumed at a particular $r - i$ in the parallax relation may be systematically placed closer or farther away from the origin (the Sun).

However, all of these are either small (e.g., contamination by giants), have a small total effect on the underlying Galactic density field (radial smearing due to dispersion in distance estimates), or cause relative radial displacements of *entire* clumps of stars with metallicities different than that of the background while not affecting their relative parallaxes and thus allowing the discrimination of finer structure. Altogether, the maps' fidelity will be fairly well preserved, making them a powerful tool for studying the Milky Way's stellar number density distribution.

2.4. The Construction of the Density Maps

The distance, estimated as described above, and the Galactic longitude and latitude, (l, b) , fully determine the three-dimensional coordinates of each star in the sample. To better control the systematics and study the dependence of density field on spectral type, we divide and map the sample in 19 bins in $r - i$ color²⁶,

$$ri_0 < r - i < ri_1. \quad (13)$$

Typically, the width of the color bins, $\Delta_{ri} \equiv ri_1 - ri_0$, is $\Delta_{ri} = 0.1$ for bins redder than $r - i = 0.7$ and $\Delta_{ri} = 0.05$ otherwise. The bin limits ri_0 and ri_1 for each color bin are given in the second column of Table 2. This color binning is roughly equivalent to a selection by MK spectral type (Covey et al. 2005) or stellar mass. The range of spectral types corresponding to each $r - i$ bin is given in the SpT column of Table 2.

For each color bin we select a volume-limited sample given by

$$\begin{aligned} D_0 &= 10^{[r_{\min} - M_r(ri_0)]/5+1} \text{ pc}, \\ D_1 &= 10^{[r_{\max} - M_r(ri_1)]/5+1} \text{ pc}, \end{aligned} \quad (14)$$

where $r_{\min} = 15$ and $r_{\max} = 21.5$ are adopted as bright and faint magnitude limits (SDSS detectors saturate at $r \sim 14$). In each color bin $D_1/D_0 \sim 15$ and for the full sample $D_1/D_0 \sim 300$.

We define the ‘‘Cartesian galactocentric coordinate system’’ by the set of coordinate transformations

$$X = R_\odot - D \cos(l) \cos(b), \quad (15)$$

$$Y = -D \sin(l) \cos(b), \quad (16)$$

$$Z = D \sin(b),$$

where $R_\odot = 8$ kpc is the adopted distance to the Galactic center (Reid 1993).

The choice of the coordinate system is motivated by the expectation of cylindrical symmetry around the axis of Galactic rotation \hat{Z} and mirror symmetry of Galactic properties with respect to the Galactic plane. Its (X, Y) origin is at the Galactic center, the \hat{X} -axis points toward the Earth, and the \hat{Z} -axis points toward the north Galactic pole. The $\hat{Y} = \hat{Z} \times \hat{X}$ axis is defined so as to keep the system right handed. The \hat{X} - \hat{Y} plane is parallel to the plane of the Galaxy, and the $Z = 0$ plane contains the Sun. The Galaxy rotates clockwise around the \hat{Z} -axis (the rotational velocity of the Sun is in the direction of the $-\hat{Y}$ -axis).

We bin the stars onto a three-dimensional rectangular grid in these coordinates. The choice of grid pixel size is driven by compromise between two competing requirements: keeping the Poisson noise in each pixel at a reasonable level, while simultaneously avoiding overbinning (and related information loss) in high-density regions of the maps. By manual trial and error of a few different pixel sizes, we come to a size (for each color bin) which satisfies both requirements. The adopted pixel sizes are listed in Table 2. For bins with $r - i > 0.3$, the median number of stars per pixel is ~ 10 , growing to ~ 30 for the bluest $r - i$ bin.

For each volume-limited (ri_0, ri_1) color bin sample, this binning procedure results in a three-dimensional data cube, a *map*, of observed stars with each (X, Y, Z) pixel value equal to the number of stars observed in the $(X - dx/2, X + dx/2)$, $(Y - dx/2, Y + dx/2)$, $(Z - dx/2, Z + dx/2)$ interval.

Not all of the pixels in the maps have had their volume fully sampled by the SDSS survey. This is especially true near the edges of the survey volume and at places where there are holes in the footprint of the survey (cf. Fig. 6). In order to convert the number of stars observed in a particular pixel (X, Y, Z) to density, we must know the fraction of pixel volume that was actually sampled by the survey. Although simple in principle, the problem of accurately binning the surveyed volume becomes nontrivial due to the overlap of observing runs, the complicated geometry of the survey, and the large survey area. We solve it by shooting a dense, horizontal, rectangular grid of vertical $(X_r = \text{const}, Y_r = \text{const})$ rays through the observed volume, with horizontal spacing of rays dx_r being much smaller than the pixel size dx (typically, $dx_r/dx = 0.1$). For each ray, we calculate the intervals in the Z -coordinate in which it intersects each imaging run (‘‘ray-run intersections’’). Since imaging runs are bounded by simple geometric shapes (cones, spheres, and planes), the ray-run intersection calculation can be done almost entirely analytically, with the only numerical part being the computation of roots of a fourth-order polynomial. For each ray, the union of all ray-run intersections is the set of Z intervals $\{[Z_0, Z_1], [Z_2, Z_3], [Z_4, Z_5], \dots\}$ at a given column (X_r, Y_r) which were sampled by the survey. It is then a simple matter to bin such interval sets in the \hat{Z} -direction and assign their parts to pixels through which they passed. Then, by approximating that the ray sweeps a small but finite area dx_r^2 , the survey volume swept by the ray contributing to pixel (X, Y, Z) is simply dx_r^2 times the length of the ray interval(s) within the pixel. By densely covering all of the (X, Y) -plane with rays, we eventually sweep the complete volume of the survey and partition it between all of the (X, Y, Z) pixels. This ray-tracing method is very general and can handle any survey geometry in any orientation, as long as the survey geometry can be represented by a set of *runs* along great circles. Using this approach, we compute the volume observed within each pixel with an accuracy of one part in 10^3 .

In summary, for each of the 19 $r - i$ color bins, we finish with a three-dimensional map in which each (X, Y, Z) pixel holds the number of observed stars (N) and the observed volume (V). We estimate the number density in the pixel by simply dividing the two,

$$\rho(X, Y, Z) = \frac{N(X, Y, Z)}{V(X, Y, Z)} \quad (17)$$

with the error in density estimate due to shot noise being

$$\sigma_\rho(X, Y, Z) = \frac{\sqrt{N(X, Y, Z)}}{V(X, Y, Z)}. \quad (18)$$

²⁶ To avoid excessive usage of parenthesis, we sometimes drop the minus sign when referring to the colors [e.g., $g - r \equiv gr$ or $(r - i)_1 \equiv ri_1$].

For each pixel we also track additional auxiliary information (e.g., a list of all contributing SDSS runs), mainly for quality assurance and detailed a posteriori analysis.

3. STELLAR NUMBER DENSITY MAPS

In this section we analyze the 19 stellar number density maps constructed as described above. The $0.10 < r - i < 1.40$ color range spanned by our sample probes a large distance range—as the bin color is varied from the reddest to the bluest, the maps cover distances from as close as 100 pc traced by M dwarfs ($r - i \sim 1.3$) to 20 kpc traced by stars near the MS turnoff ($r - i \sim 0.1$). We begin the analysis with a qualitative survey of the various map cross sections and then proceed to a quantitative description within the context of analytic models.

3.1. The Number Density Maps in the R - Z Plane

We first analyze the behavior of two-dimensional maps in the R - Z plane, where $R = (X^2 + Y^2)^{1/2}$ and Z are the galactocentric cylindrical coordinates. Assuming the Galaxy is circularly symmetric (we critically examine this assumption below), we construct these maps from the three-dimensional maps by taking a weighted mean of all the values for a given Z - R pixel [i.e., we average over the galactocentric polar angle $\phi = \arctan(Y/X)$]. We show a subset of these maps in Figure 10. They bracket the analyzed $r - i$ range; the remaining maps represent smooth interpolations of the displayed behavior. The bottom two panels in Figure 10 correspond to the reddest bins and thus to the solar neighborhood within ~ 2 kpc. They show a striking simplicity in good agreement with a double exponential disk model,

$$\rho(R, Z) = \rho(R_{\odot}, 0)e^{R_{\odot}/L} \exp\left(-\frac{R}{L} - \frac{Z + Z_{\odot}}{H}\right), \quad (19)$$

where ρ is the number density of disk stars, R_{\odot} and Z_{\odot} are the cylindrical coordinates of the Sun, and L and H are the exponential scale length and scale height, respectively. This model predicts that the isodensity contours have the linear form

$$|Z + Z_{\odot}| = C - \frac{H}{L}R, \quad (20)$$

where C is an arbitrary constant, a behavior that is in good agreement with the data.

As the bin color becomes bluer (Fig. 10, *middle and top*) and probed distances larger, the agreement with this simple model worsens. First, the isodensity contours become curved, and it appears that the disk flares for $R > 14$ kpc. Further, as we discuss below, the Z -dependence deviates significantly from the single exponential given by equation (19), and additional components or a different functional form are required to explain the observed behavior.

We test whether the number density maps are circularly symmetric by examining isodensity contours on a cylindrical surface at $R = R_{\odot}$ kpc. Figure 11 shows such projections for two color bins, where we plot the dependence of isodensity contours on the galactocentric polar angle ϕ and the distance from the plane Z . In the case of cylindrical symmetry, the contours would be horizontal. The top panel of Figure 11 shows the isodensity contours for the $1.0 < r - i < 1.1$ color bin and is representative of all bins redder than $r - i \geq 0.35$ mag. The contours are horizontal,

and the number density maps are indeed approximately cylindrically symmetric. However, for bins $r - i < 0.35$ mag, detectable deviations from cylindrical symmetry do exist, especially at large distances from the Galactic plane (a few kpc and beyond). We show an example of this in the bottom panel of Figure 11, where there is a slight upturn of the isodensity contour at $Z \sim 10,000$ pc and $\phi \sim 40^\circ$, indicating the presence of an overdensity. We discuss such overdensities in more detail in § 3.2.

3.2. The X - Y Slices of the Three-Dimensional Number Density Maps

Instead of contracting the three-dimensional maps by taking the mean of all ϕ values for a given Z - R pixel, two-dimensional analysis can be based on simple cross sections parallel to an appropriately chosen plane. A convenient choice is to study the X - Y cross sections that are parallel to the Galactic plane. A series of such projections for the bluest color bin is shown in Figures 12–14. Their outlines are determined by the data availability. In particular, the gap between the two largest data regions will be eventually filled in as more SDSS imaging data becomes available.²⁷

An unexpected large overdensity feature is easily discernible in five of the six panels in Figure 12. In all standard Galaxy models, the stellar density in the upper half ($Y > 0$) should mirror the bottom half ($Y < 0$), and in most models, density depends only on the distance from the center of the Galaxy (each annulus enclosed by two successive circles should have roughly the same color). In contrast, the observed density map, with a strong local maximum offset from the center, is markedly different from these model predictions. This is the same feature that is responsible for the structure visible at $Z \sim 10$ kpc and $R \sim 5$ kpc in the top left panel in Figure 10 and for the upturn of the isodensity contour at $Z \sim 10,000$ pc and $\phi \sim 40^\circ$ in the bottom panel in Figure 11. We discuss this remarkable feature in more detail in § 5.

The top three panels ($Z = 3$ – 5 kpc) in Figure 13 clearly show another local overdensity at $R \sim 16$ kpc and $Y \sim 0$. This is the “Monoceros stream” discovered by Newberg et al. (2002) using a subset of the data analyzed here (this overdensity is also discernible in the top left panel in Fig. 10 at $R \sim 16$ kpc and $Z \sim 3$ kpc). The maps discussed here suggest that the stream is well localized in the radial direction with a width of ~ 3 kpc. This well-defined width rules out the hypothesis that this overdensity is due to disk flaring. An alternative hypothesis, that of a “ring” around the Galaxy, was proposed by Ibata et al. (2003) but put into question by observations of Rocha-Pinto et al. (2003). In particular, Rocha-Pinto et al. analyzed the distribution of 2MASS M giants in the Monoceros feature and concluded its morphology was inconsistent with a homogeneously dense ring surrounding the Milky Way. Instead, a more likely explanation is a merging dwarf galaxy with tidal arms. The inhomogeneity of the stream apparent in the top three panels of Figure 13 as well as $R = \text{const}$ projections of these maps and a theoretical study by Peñarrubia et al. (2005) support this conclusions as well.

Closer to the plane, at distances of less than about 1 kpc, the number density maps become smoother and less asymmetric, with deviations from a simple exponential model not exceeding 30%–40% (measured upper limit). This is true of all color bins for which the region closer than ~ 2 kpc is well sampled and is shown in Figure 14 for the $1.0 < r - i < 1.1$ color bin.

²⁷ This region of the sky has already been imaged and will be a part of SDSS Data Release 6 projected to be released in 2007 July.

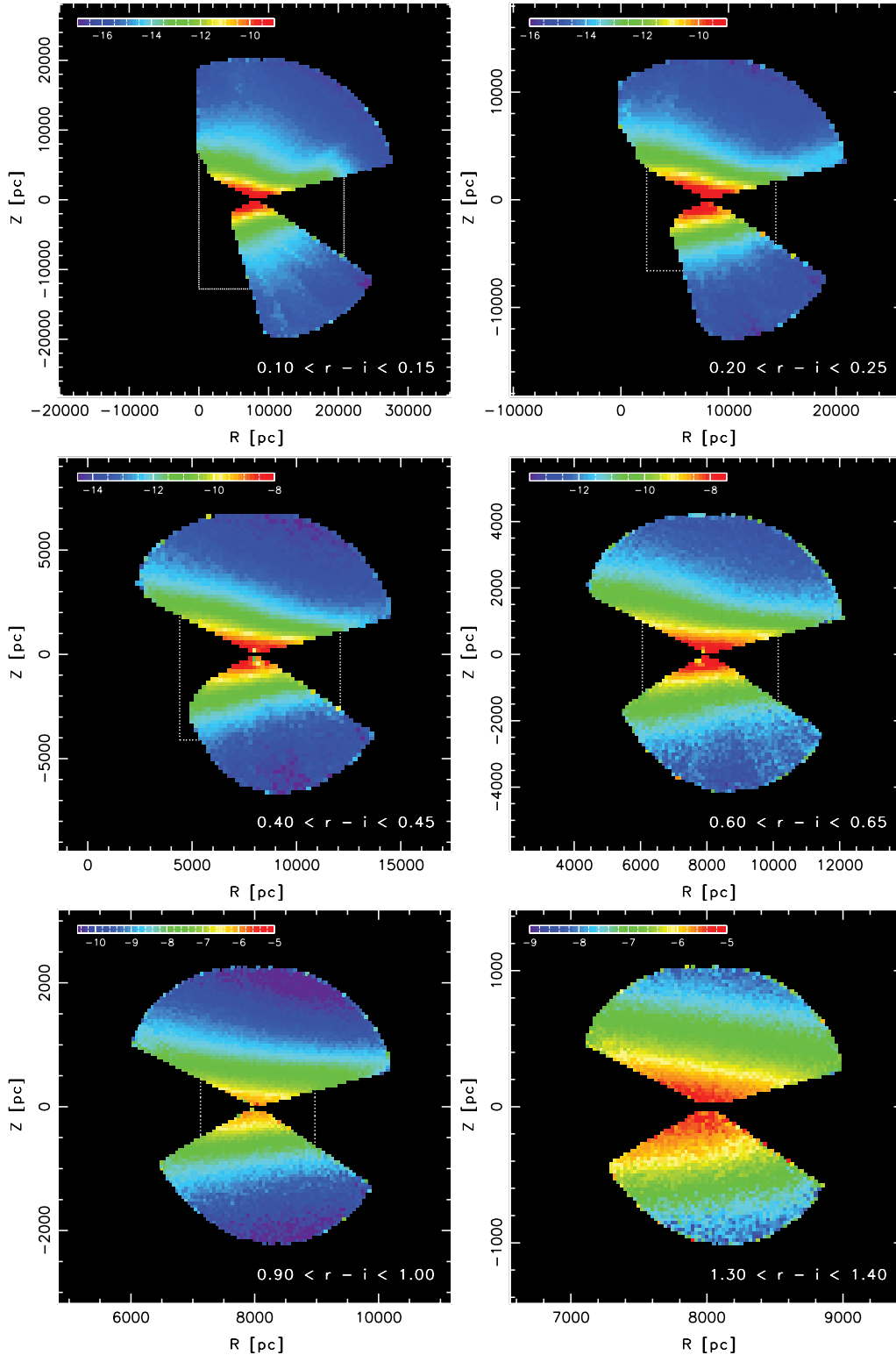


FIG. 10.—Stellar number density as a function of Galactic cylindrical coordinates R (distance from the axis of symmetry) and Z (distance from the plane of the Sun), for different $r - i$ color bins, as marked in each panel. Each pixel value is the mean for all polar angles ϕ . The density is shown on a natural log scale and coded from blue to red (black pixels are regions without the data). Note that the distance scale greatly varies from the top left to the bottom right panel; the size of the bottom right panel is roughly equal to the size of four pixels in the top left panel. Each white dotted rectangle denotes the bounding box of the region containing the data on the subsequent panel.

3.3. Overall Distribution of Stellar Number Density

Traditionally, the stellar distribution of the Milky Way has been decomposed into several components: the thin and thick disks, the central bulge, and a much more extended and tenuous

halo. While it is clear from the preceding discussion that there are a number of overdensities that complicate this simple model, the dynamic range of the number density variation in the Galaxy (orders of magnitude) is large compared to the local density excess due to those features (a factor of a few). Hence, it should

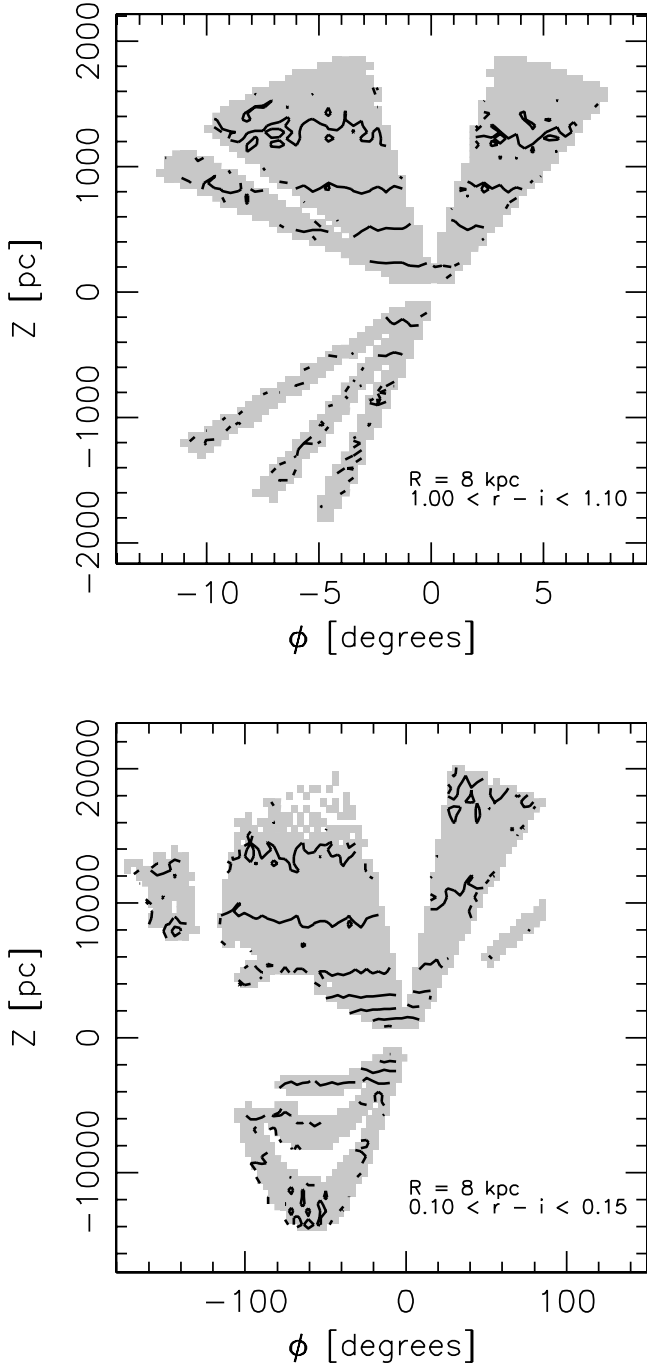


FIG. 11.—Azimuthal dependence of the number density for $R = R_{\odot}$ cylinder around the Galactic center. The shaded region is the area covered by the SDSS survey, and the lines show constant density contours for two color bins ($1.0 < r - i < 1.1$ in the top panel and $0.10 < r - i < 0.15$ in the bottom panel). The fact that isodensity contours are approximately horizontal supports the assumption that the stellar number density distribution is cylindrically symmetric around the Galactic center and at the same time indicates that the assumed photometric parallax distribution is not grossly incorrect. Nevertheless, note that deviations from cylindrical symmetry do exist, e.g., at $Z \sim 10$ kpc and $\phi \sim 40^{\circ}$ in the bottom panel.

still be possible to capture the overall density variation using analytic models.

Before attempting full complex multiparameter fits to the overall number density distribution, we first perform a simple qualitative exploration of density variation in the radial (R) and vertical

(Z) directions. This type of analysis serves as a starting point to understand what types of models are at all compatible with the data and to obtain reasonable initial values of model parameters for global multiparameter fits (§ 4.2).

3.3.1. The Z -Dependence of the Number Density

Figure 15 shows the stellar number density for several color bins as a function of the distance Z from the plane of the Sun at $R = R_{\odot}$. The behavior for red bins, which probe the heights from 50 pc to ~ 2 kpc, is shown in the top panel of Figure 15. They all appear to be well fit by an exponential profile²⁸ with a scale height of ~ 270 pc.²⁹ While the best-fit value of this scale height is uncertain up to 10%–20%, it is encouraging that the same value applies to all the bins. This indicates that the slope of the adopted photometric parallax relation is not greatly incorrect at the red end.

The extrapolations of the best exponential fits for $Z < 0$ and $Z > 0$ to small values of $|Z|$ cross at $Z \sim -25$ pc. This is the well-known solar offset from the Galactic plane toward the north Galactic pole (e.g., Reid 1993), which is here determined essentially directly using a few orders of magnitude greater number of stars (several hundred thousand) than in previous work.

By selecting bluer bins, the Z -dependence of the number density can be studied beyond 1 kpc, as illustrated in the middle panel of Figure 15. At these distances, the number density clearly deviates from a single exponential disk model. The excess of stars at distances beyond 1 kpc, compared to this model, is usually interpreted as evidence of another disk component, the thick disk. Indeed, the data shown in the middle panel in Figure 15 can be modeled using a double exponential profile.

The need for yet another, presumably halo, component is discernible in the bottom panel in Figure 15, which shows the number density for the bluest color bin. The data show that beyond 3–4 kpc even the thick disk component underpredicts the observed counts. The observations can be explained by adding a power-law halo component.

3.3.2. The R -Dependence of the Number Density

We examine the dependence of number density on the (cylindrical) distance from the Galactic center in Figures 16, 17, and 18. Each figure shows the number density as a function of R for a given $r - i$ color bin at different heights above the Galactic plane. For red bins, which probe the solar neighborhood within ~ 2 kpc, the density profiles are approximately exponential (i.e., straight lines in the $\ln(\rho)$ vs. R plot, see Fig. 16). The exponential scale length seems to increase with the distance from the Galactic plane or, alternatively, requires the introduction of an additional exponential dependence with a different scale. Because of the small baseline, this variation or the scale lengths are not strongly constrained with plausible values around $L \sim 3.5$ kpc and an uncertainty of at least 30%.

²⁸ Motivated by theoretical reasoning (e.g., Binney & Tremaine 1987), sometimes the sech^2 function is used instead of exponential dependence. However, the exponential provides a significantly better description of the data than sech^2 . For example, the exponential distribution is a good fit all the way toward the plane to $1/6$ or so of the scale height, where the sech^2 function would exhibit significant curvature in the $\ln(\rho)$ vs. Z plot.

²⁹ Note that this is just an *initial estimate* for the scale height, based on a single effective line of sight (SGP–NGP) and limited Z coverage. In § 4.2 we derive the values of Galactic model parameters using the entire data set.

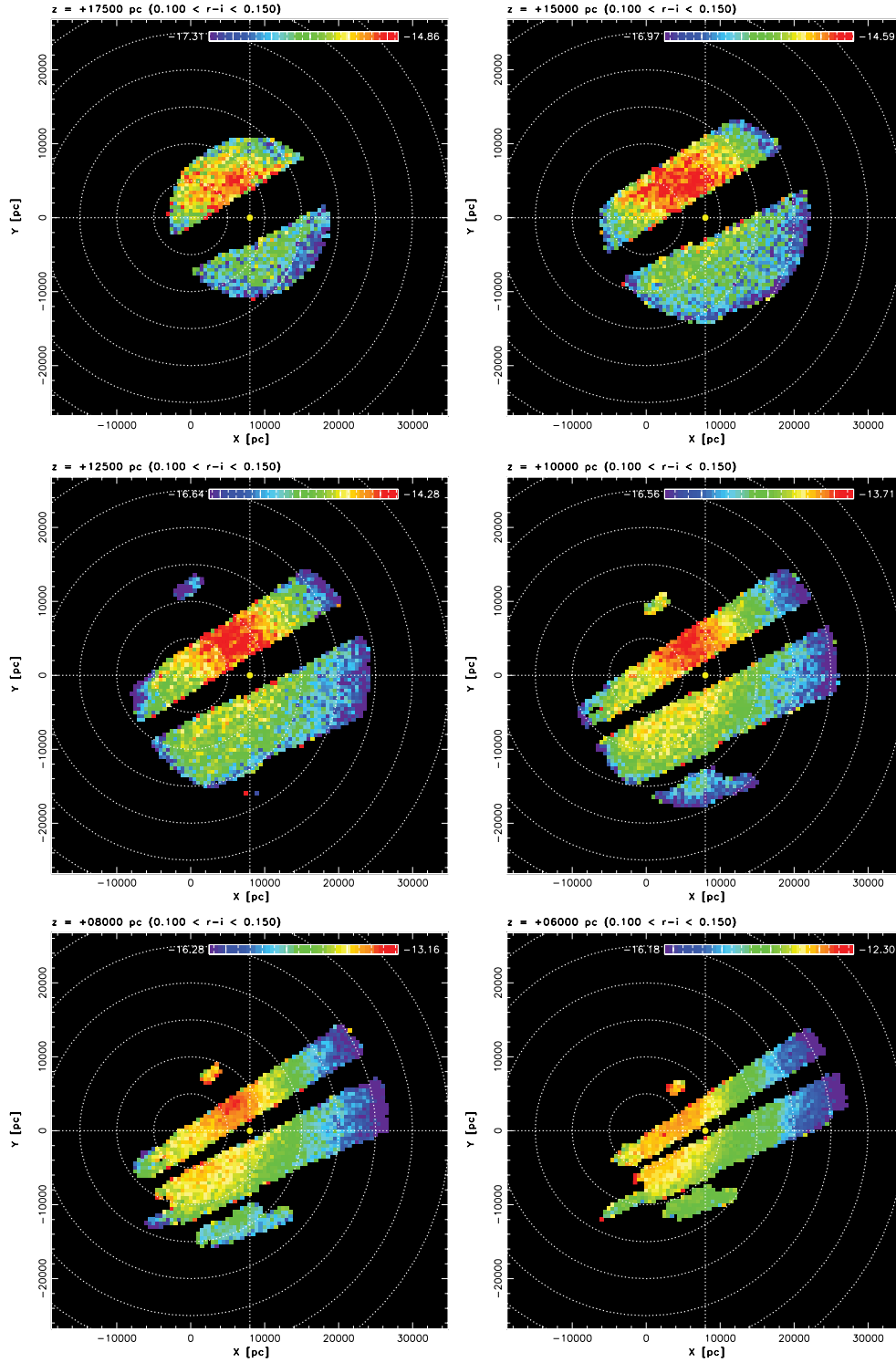


FIG. 12.—Stellar number density for the same color bin as in the top left panel in Fig. 10 ($0.10 < r - i < 0.15$), shown here in slices parallel to the Galactic plane, as a function of the distance from the plane. The distance from the plane varies from 17.5 kpc (*top left*) to 6 kpc (*bottom right*), in steps of 2 and 2.5 kpc. The circles visualize presumed axial symmetry of the Galaxy, and the origin marks the location of the Galactic center (the Sun is at $X = 8$, $Y = 0$ kpc). Note the strong asymmetry with respect to the $Y = 0$ line.

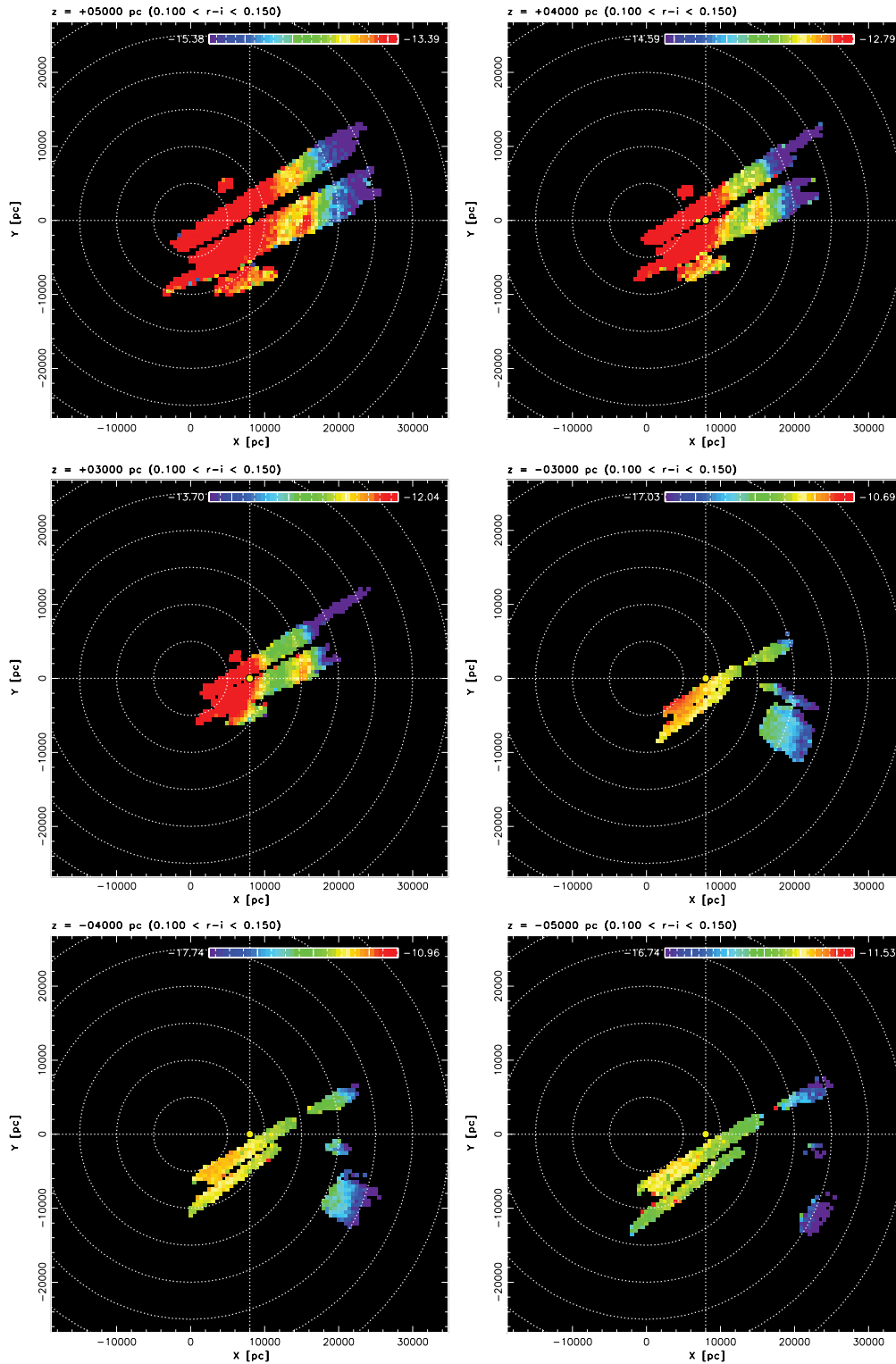


FIG. 13.— Same as Fig. 12, except that three symmetric slices at $Z = 3, 4,$ and 5 kpc above and below the plane are shown. The color stretch in panels for $Z = 3, 4,$ and 5 kpc is optimized to bring out the Monoceros overdensity at $R \sim 16$ kpc and $Y \sim 0$.

At distances from the Galactic plane exceeding 1–2 kpc, the exponential radial dependence becomes a fairly poor fit to the observed density distribution (Fig. 17). The main sources of discrepancy are several overdensities noted in § 3.2. In particular, the Monoceros stream is prominent at $Z \sim 2$ –8 kpc, especially when the density profiles are extracted only for the $|Y| < 1$ kpc slice (Fig. 18).

4. GALACTIC MODEL

The qualitative exploration of the number density maps in the preceding section, as well as the analysis of the density variation in the radial R - and vertical Z -directions, suggest that the gross behavior can be captured by analytic models. These typically model

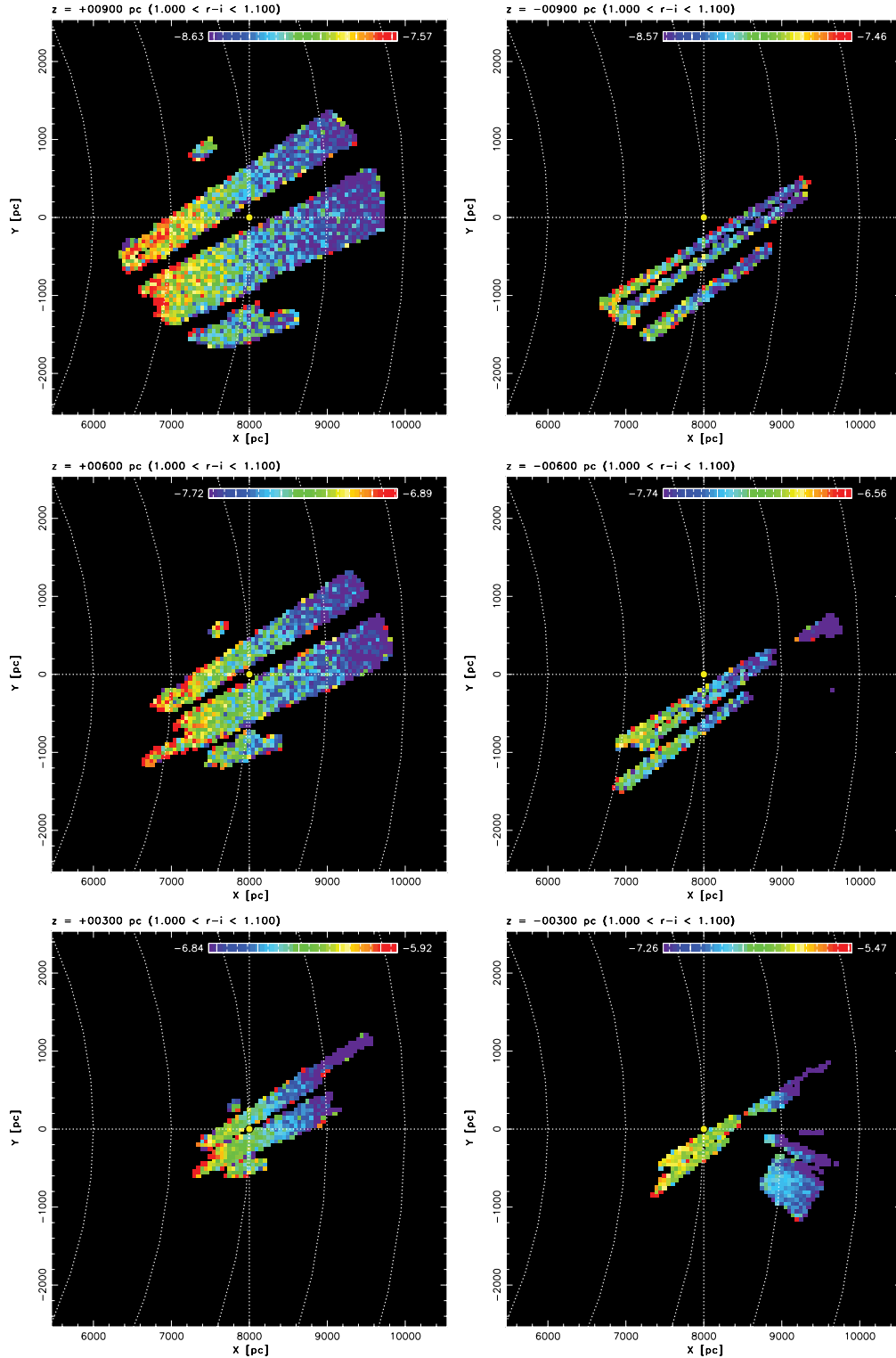


FIG. 14.— Same as Fig. 12, except that here three symmetric slices at $Z = 300, 600,$ and 900 pc above and below the plane are shown, for the $1.00 < r - i < 1.10$ color bin. Note that at these distance scales there is no obvious discernible substructure in the density distribution.

the number density distribution with two exponential disks and a power-law (or de Vaucouleurs spheroidal) elliptical halo.

Following earlier work (e.g., Majewski 1993; Siegel et al. 2002; Chen et al. 2001), we decompose the overall number density into the sum of disk and halo contributions

$$\rho(R, Z) = \rho_D(R, Z) + \rho_H(R, Z). \quad (21)$$

We ignore the bulge contribution because the maps analyzed here only cover regions more than 3–4 kpc from the Galactic center, where the bulge contribution is negligible compared to the disk and halo contributions (for plausible bulge parameters determined using *IRAS* data for asymptotic giant stars, see, e.g., Jackson et al. 2002).

Following Bahcall & Soneira (1980) and Gilmore & Reid (1983) we further decompose the disk into a sum of two exponential

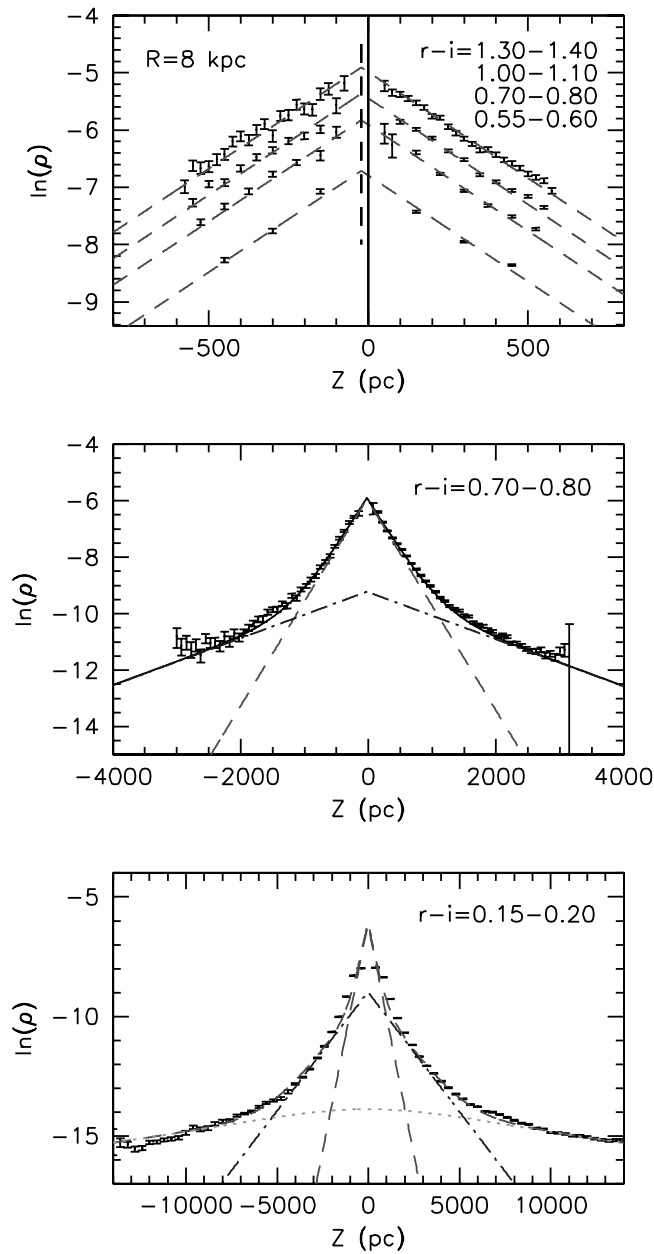


FIG. 15.—Vertical (Z) distribution of SDSS stellar counts for $R = 8$ kpc and different $r - i$ color bins, as marked. The lines are exponential models fitted to the points. The dashed lines in the top panel correspond to a fit with a single, exponential disk having a 270 pc scale height. The vertical dot-dashed line marks the position of the density maximum and implies a solar offset from the Galactic plane of ~ 20 pc. The dashed line in the middle panel corresponds to a sum of two disks with scale heights of 270 and 1200 pc and a relative normalization of 0.04 (the “thin” and the “thick” disks). The dot-dashed line is the contribution of the 1200 pc disk. Note that its contribution becomes important for $|Z| > 1000$ pc. The dashed line in the bottom panel (closely following the data points) corresponds to a sum of two disks (with scale heights of 260 and 1000 pc and the relative normalization of 0.06), a power-law spherical halo with power-law index of 2, and a relative normalization with respect to the 260 pc disk of 4.5×10^{-4} . The dashed line is the contribution of the 260 pc disk, the dot-dashed line is the contribution of the 1000 pc disk, and the halo contribution is shown by the dotted line. Note that both the disk and halo models shown here are just the *initial estimates* of model parameters, based solely on this Z cross section. As we discuss in § 4.3.9, these are not the only combinations of model parameters fitting the data, and the true model parameters fitting *all* of the data are in fact substantially different (Table 10). [See the electronic edition of the *Journal* for a color version of this figure.]

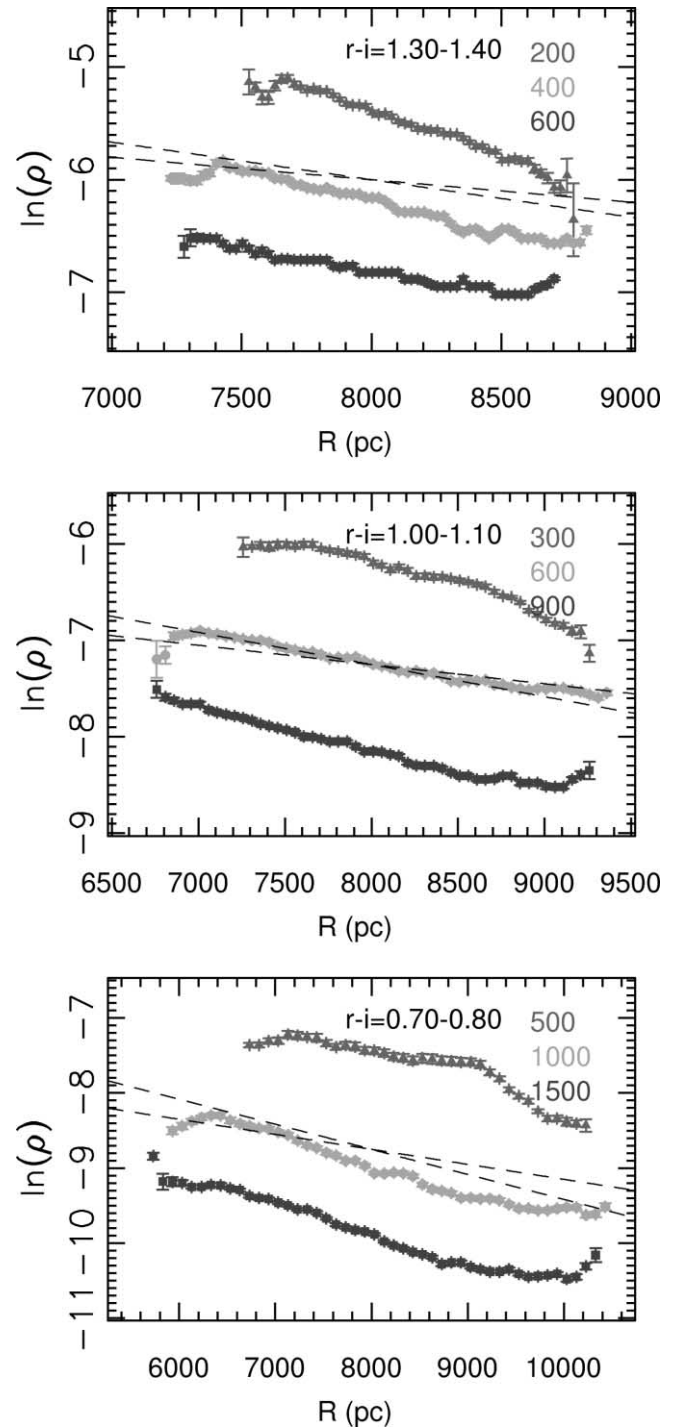


FIG. 16.—Radial distribution of SDSS stellar counts for different $r - i$ color bins and at different heights above the plane, as marked in each panel. The two dashed lines show the exponential radial dependence of density for scale lengths of 3000 and 5000 pc (with arbitrary normalization). [See the electronic edition of the *Journal* for a color version of this figure.]

components (the “thin” and the “thick” disk), allowing for different scale lengths and heights of each component,

$$\rho_D(R, Z) = \rho_D(R, Z; L_1, H_1) + f \rho_D(R, Z; L_2, H_2), \quad (22)$$

where

$$\rho_D(R, Z; L, H) = \rho_D(R_\odot, 0) e^{R_\odot/L} \exp\left(-\frac{R}{L} - \frac{Z + Z_\odot}{H}\right), \quad (23)$$

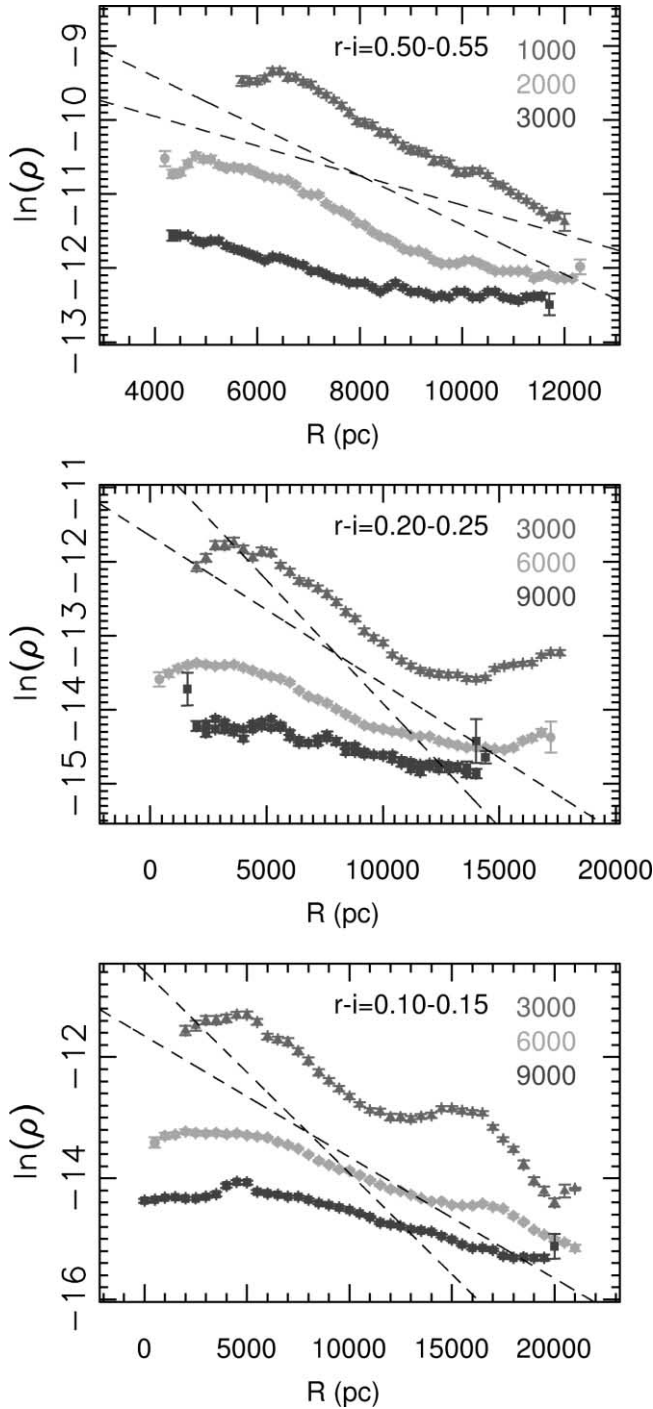


FIG. 17.—Same as Fig. 16, but for bluer color bins, which probe larger distances. [See the electronic edition of the Journal for a color version of this figure.]

where H_1 and H_2 and L_1 and L_2 are the scale heights and lengths for the thin and thick disks, respectively, f is the thick disk normalization relative to the thin disk at ($R = R_\odot, Z = 0$), and Z_\odot is the solar offset from the Galactic plane. From previous work, typical best-fit values are $H_1 \sim 300$ pc, $H_2 \sim 1\text{--}2$ kpc, $f \sim 1\%\text{--}10\%$, and $Z_\odot \sim 10\text{--}50$ pc (e.g., Siegel et al. 2002, Table 1). We also briefly explored models where thin and thick disks had the same scale length that was allowed to vary linearly with distance from the Galactic plane ($L = L_0 + kZ$), but found these to be unnecessary as the two-disk formalism was able to adequately capture the behavior of the data.

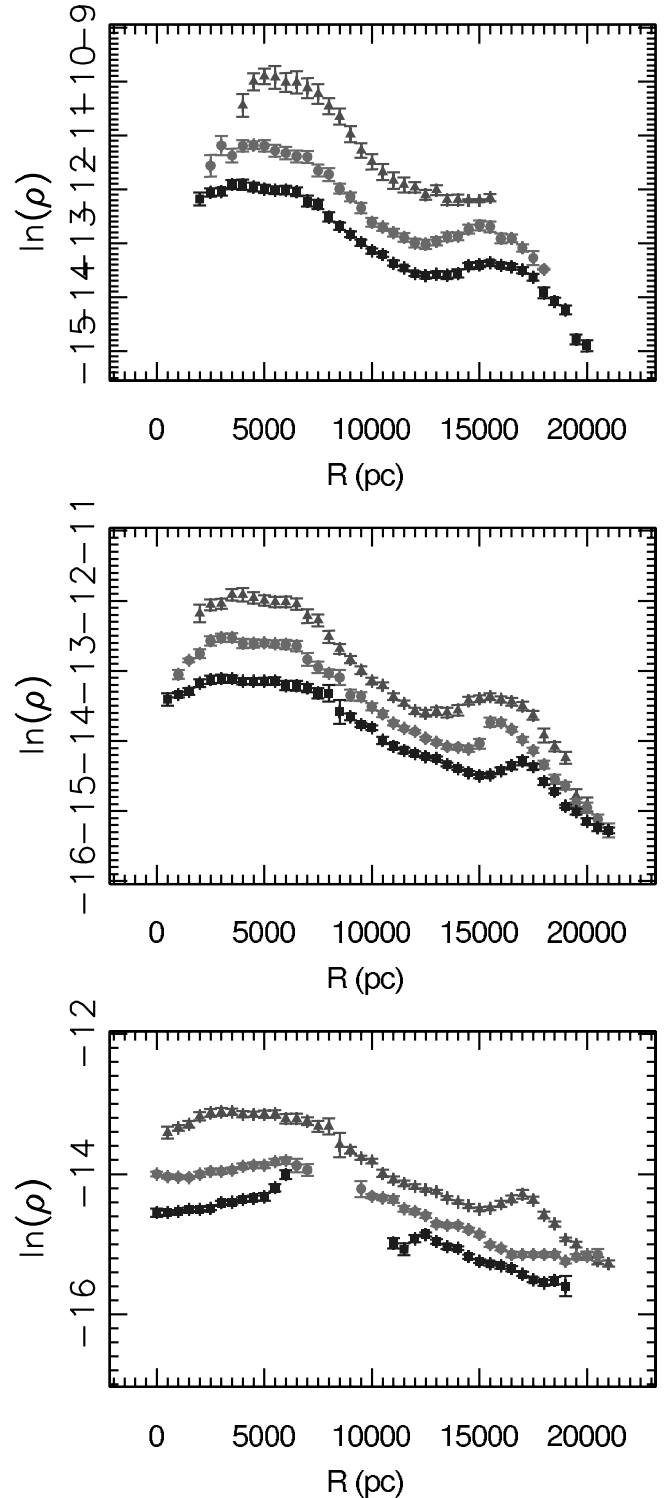


FIG. 18.—Radial distribution of SDSS stellar counts for $0.10 < r - i < 0.15$ color bin, with the data restricted to $|y| < 1$ kpc. The selected heights are, from top to bottom, (2, 3, 4), (4, 5, 6), and (6, 8, 10) kpc. The Monoceros stream is easily visible as local maxima at $R = 16\text{--}17$ kpc, and the Virgo overdensity as the wide bump at $R \sim 6$ kpc. [See the electronic edition of the Journal for a color version of this figure.]

We model the halo as a two-axial power-law ellipsoid³⁰,

$$\rho_H(R, Z) = \rho_D(R_\odot, 0) f_H \left[\frac{R_\odot}{\sqrt{R^2 + (Z/q_H)^2}} \right]^{n_H}. \quad (24)$$

The parameter q_H controls the halo ellipticity, with the ellipsoid described by axes $a = b$ and $c = q_H a$. For $q_H < 1$ the halo is oblate, that is, “squashed” in the same sense as the disk. The halo normalization relative to the thin disk at $(R = R_\odot, Z = 0)$ is specified by f_H . From previous work, typical best-fit values are $n_H \sim 2.5\text{--}3.0$, $f_H \sim 10^{-3}$, and $q_H \sim 0.5\text{--}1$.

4.1. Data Set Preparation

The fitting of models described by equations (21)–(24) will be affected by overdensities identified in § 3.2 and other, smaller overdensities that may be harder to see at first. If unaccounted for, such overdensities will almost certainly bias the best-fit model parameters. In general, as we discuss below in § 4.3.7, their effect is to artificially increase the scale heights of the disks, in order to compensate for the localized density excesses away from the plane. We therefore exclude from the data set the regions where there are obvious localized deviations from a smooth background profile.³¹ The excluded regions are shown in Figure 19.

We exclude the newly found large overdensity discernible in Figure 12 (the “Virgo overdensity”) by masking the pixels that simultaneously satisfy

$$\begin{aligned} -5 < X'/(1 \text{ kpc}) < 25, \\ Y' > -4 \text{ kpc}, \\ (X - 8 \text{ kpc})^2 + Y^2 + Z^2 > (2.5 \text{ kpc})^2, \end{aligned}$$

where

$$\begin{pmatrix} X' \\ Y' \end{pmatrix} = \begin{pmatrix} \cos 30^\circ & -\sin 30^\circ \\ \sin 30^\circ & \cos 30^\circ \end{pmatrix} \begin{pmatrix} X \\ Y \end{pmatrix}.$$

The third condition excludes from the cut pixels closer than 2.5 kpc to the Sun, which are uncontaminated by the overdensity. The excluded region is shown in Figure 19 bounded by the rectangle in the top panel.

The Monoceros stream is located at an approximately constant galactocentric radius. We exclude it by masking out all pixels that satisfy either of the two conditions:

$$\begin{aligned} 14 \text{ kpc} < R < 24 \text{ kpc} \wedge 0 < Z < 7 \text{ kpc}, \\ 16 \text{ kpc} < R < 24 \text{ kpc} \wedge 7 < Z < 10 \text{ kpc}. \end{aligned}$$

These correspond to the region bounded by two white rectangles in the bottom panel of Figure 19.

After the removal of the Virgo and Monoceros regions, the initial fit for bins redder than $r - i = 1.0$ resulted in measured thin and thick scale heights of $H_1 \sim 280$ and $H_2 \sim 1200$. The residuals of this fit showed clear signatures of at least two more major overdensities ($\sim 40\%$ above background), one near $(R, Z) \sim (6.5, 1.5)$ kpc

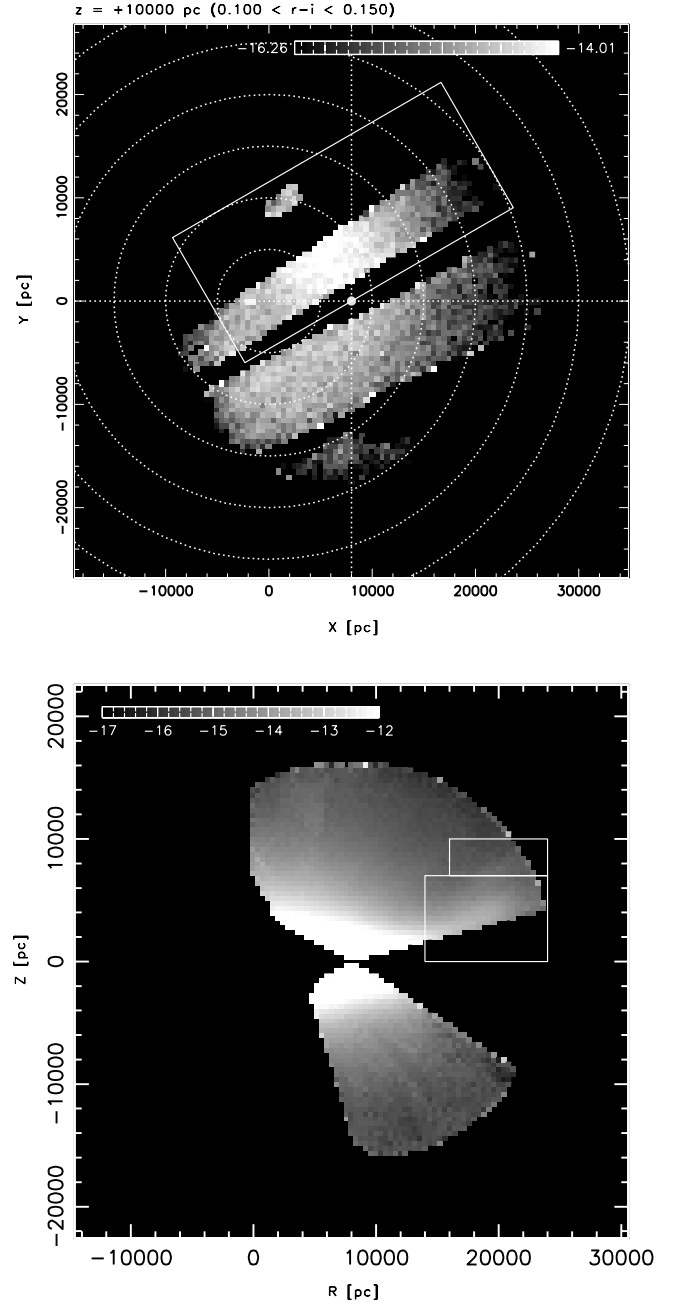


FIG. 19.—Regions with large overdensities excluded from Galactic model fits. The pixels within the rectangle in the top panel are excluded to avoid contamination by the Virgo overdensity (§ 5). The pixels enclosed by the two rectangles in the bottom panel, centered at $R \sim 18$ kpc, exclude the Monoceros stream.

and the other near $(R, Z) \sim (9, 1)$ kpc. We therefore went back and further excluded the pixels satisfying

$$\begin{aligned} -90^\circ < \arctan\left(\frac{Z - 0.75 \text{ kpc}}{R - 8.6 \text{ kpc}}\right) < 18^\circ \wedge Z > 0, \\ R < 7.5 \text{ kpc} \wedge Z > 0. \end{aligned}$$

The remaining pixels are averaged over the galactocentric polar angle ϕ to produce the equivalent of (R, Z) maps shown in Figure 10. We additionally imposed a cut on Galactic latitude, excluding all pixels with $b < 20^\circ$ to remove the stars observed close to the Galactic disk. This excludes stars that may have been overcorrected for extinction (§ 2.3.2) and stars detected in imaging

³⁰ For the halo component, $Z + Z_\odot \approx Z$ is a very good approximation.

³¹ Note that we are excluding overdensities, but not underdensities, as there are physical reasons to expect the Galaxy to have a smooth distribution with overdense regions (due to mergers, clusters, etc.).

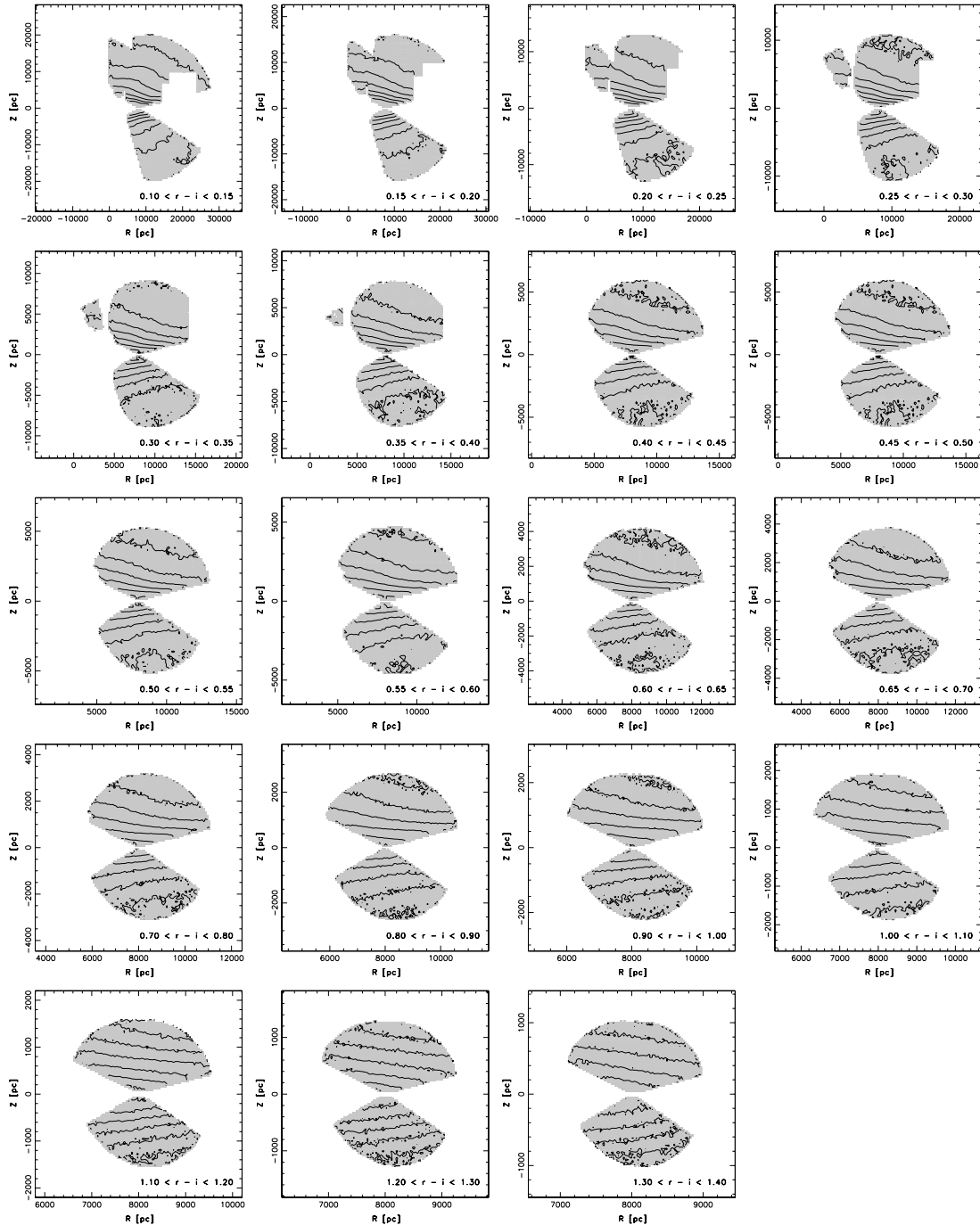


FIG. 20.—“Cleaned-up” (R, Z) maps of the Galaxy, analogous to Fig. 10, but with pixels in obvious overdensities (Fig. 19) excluded from azimuthal averaging. We show the maps for all 19 color bins, with the bluest bin in the top left corner and the reddest bin in the bottom right. The contours are the lines of constant density, spaced at constant logarithmic intervals.

runs crossing the Galactic plane where the efficiency of SDSS photometric pipeline drops due to extremely crowded fields. Other, less significant, $r - i$ bin-specific cuts have also been applied, for example, the exclusion of $|Z| > 2500$ pc stars in $r - i > 1.0$ bins to avoid contamination by halo stars.

We show all 19 “cleaned-up” maps in Figure 20. The contours denote the locations of constant density. The gray areas show the regions with available SDSS data. Compared to Figure 10, the constant density contours are much more regular, and the effect of the Virgo overdensity is largely suppressed. The regularity of the density distribution is particularly striking for redder bins (e.g., for $r - i > 0.7$). In the bluest bin ($0.10 < r - i < 0.15$), there is a detectable departure from a smooth profile in the top left part of

the sampled region. This is the area of the (R, Z) -plane where the pixels that are sampled far apart in (X, Y, Z) -space map onto adjacent pixels in (R, Z) -space. Either deviations from axial symmetry or small errors in the photometric parallax relation (perhaps due to localized metallicity variations) can lead to deviations of this kind. Unfortunately, which one of the two it is, is impossible to disentangle with the data at hand.

4.2. Model Fit

4.2.1. Fitting Algorithm

The model-fitting algorithm is based on the standard Levenberg-Marquardt nonlinear χ^2 minimization algorithm (Press et al.

TABLE 3
BEST-FIT VALUES (JOINT FITS, BRIGHT PARALLAX RELATION)

χ^2	Bin	$\rho(R_\odot, 0)$	L_1	H_1	f	L_2	H_2	f_H
1.61.....	1.3 < $r - i$ < 1.4	0.0058	2150	245	0.13	3261	743	...
	1.2 < $r - i$ < 1.3	0.0054						
	1.1 < $r - i$ < 1.2	0.0046						
	1.0 < $r - i$ < 1.1	0.0038						
1.70.....	0.9 < $r - i$ < 1.0	0.0032	2862	251	0.12	3939	647	0.00507
	0.8 < $r - i$ < 0.9	0.0027						
	0.7 < $r - i$ < 0.8	0.0024						
	0.65 < $r - i$ < 0.7	0.0011						

NOTES.—Best-fit values of Galactic model parameters derived assuming the “bright” photometric parallax relation (eq. [2]). The fit to $0.65 < r - i < 1.0$ bins (bottom row) includes the halo component. Its shape was kept fixed (Table 5, top row), and only the normalization f_H was allowed to vary.

1992), with a multistep iterative outlier rejection. The goal of the iterative outlier rejection procedure is to automatically and gradually remove pixels contaminated by unidentified overdensities, single pixels, or small groups of pixels with large deviations (such as those due to localized star clusters or simply due to instrumental errors, usually near the edges of the volume) and to allow the fitter to “settle” toward the true model even if the initial fit is extremely biased by a few high- σ outliers.

The outlier rejection works as follows: after the initial fit is made, the residuals are examined for outliers from the model higher than a given number of standard deviations, σ_1 . Outlying data points are excluded, the model is refitted, and all data points are retested with the new fit for deviations greater than σ_2 , where $\sigma_2 < \sigma_1$. The procedure is repeated with $\sigma_3 < \sigma_2$, etc. The removal of outliers continues until the last step, where outliers higher than σ_N are excluded and the final model is refitted. The parameters obtained in the last step are the best-fit model parameters.

The σ_i sequence used for outlier rejection is $\sigma_i = \{50, 40, 30, 20, 10, 5\}$. This slowly decreasing sequence allows the fitter to start with rejecting the extreme outliers (which themselves bias the initial fit) and then (with the model now refitted without these outliers and therefore closer to the true solution) gradually remove outliers of smaller and smaller significance and converge toward a solution which best describes the smooth background.

4.2.2. A Measurement of Solar Offset

We begin the modeling by fitting a single exponential disk to the three reddest color bins to find the value of the solar offset Z_\odot . To avoid contamination by the thick disk, we only use pixels with $|Z| < 300$ pc, and to avoid effects of overestimated interstellar extinction correction for the nearest stars (§ 2.3.2), we further exclude pixels with $|Z| < 100$. We further exclude all pixels outside of the $7600 < R < 8400$ pc range, to avoid contamination by clumpy substructure.

We obtain

$$Z_{\odot, \text{bright}} = (25 \pm 5) \text{ pc}, \quad (25)$$

$$Z_{\odot, \text{faint}} = (24 \pm 5) \text{ pc}, \quad (26)$$

for the solar offset, where $Z_{\odot, \text{bright}}$ is the offset obtained using the bright photometric parallax relation and $Z_{\odot, \text{faint}}$ is the offset obtained using the faint. The quoted uncertainty is determined by simply assuming a 20% systematic uncertainty in the adopted distance scale and does not imply a Gaussian error distribution (the formal random fitting error is smaller than 1 pc).

Our value of the solar offset agrees favorably with recent independent measurements [$Z_\odot = (27.5 \pm 6)$ pc, Chen et al. 1999;

TABLE 4
BEST-FIT VALUES (JOINT FITS, FAINT PARALLAX RELATION)

χ^2	Bin	$\rho(R_\odot, 0)$	L_1	H_1	f	L_2	H_2	f_H
1.59.....	1.3 < $r - i$ < 1.4	0.0064	2037	229	0.14	3011	662	...
	1.2 < $r - i$ < 1.3	0.0063						
	1.1 < $r - i$ < 1.2	0.0056						
	1.0 < $r - i$ < 1.1	0.0047						
2.04.....	0.9 < $r - i$ < 1.0	0.0043	2620	225	0.12	3342	583	0.00474
	0.8 < $r - i$ < 0.9	0.0036						
	0.7 < $r - i$ < 0.8	0.0032						
	0.65 < $r - i$ < 0.7	0.0015						

NOTES.—Best-fit values of Galactic model parameters derived assuming the “faint” photometric parallax relation (eq. [1]). The fit to $0.65 < r - i < 1.0$ bins (bottom row) includes the halo component. Its shape was kept fixed (Table 5, bottom row), and only the normalization f_H was allowed to vary.

$Z_\odot = (27 \pm 4)$ pc, Chen et al. 2001; (24.2 ± 1.7) pc obtained from trigonometric *Hipparcos* data by Maíz-Apellániz 2001]. We keep the value of the solar offset fixed in all subsequent model fits.

4.2.3. Disk Fits

We utilize the R - Z density maps of the four $r - i > 1.0$ bins to fit the double exponential disk model. These color bins sample the thin and thick disks, with a negligible halo contribution (less than $\sim 1\%$ for plausible halo models). Furthermore, the photometric relations in this range of colors are calibrated to the metallicities of disk dwarfs, thus making these bins optimal for the measurement of disk model parameters.

We simultaneously fit all double exponential disk model parameters ($\rho, H_1, L_1, f, H_2, L_2$) to the data, for both bright and faint photometric parallax relations. To avoid contamination by the halo, we only use the pixels with $|Z| < 2500$ pc. To avoid effects of overestimated interstellar extinction correction for the nearest stars (§ 2.3.2), we further exclude pixels with $|Z| < 100$.

We jointly fit the data from all four color bins and separately for each bin. In the former, “joint fit” case, only the densities $\rho(R_\odot, 0)$ are allowed to vary between the bins, while the scale lengths, heights, and thick-to-thin disk normalization f are constrained to be the same for stars in each bin. As the color bins under consideration sample stars of very similar mass, age, and metallicity, we expect the same density profile in all bins.³² The best-fit parameters for the joint fit to $r - i > 1.0$ bins are given in the top row of Tables 3 and 4, calculated assuming the bright (eq. [2]) and faint (eq. [1]) photometric parallax relations, respectively. Two-dimensional cross sections of the reduced χ^2 hypersurface around best-fit values are shown in Figure 21 (for the bright relation only; analogous cross sections obtained with the faint relation look qualitatively the same).

In the case of separate fits, all parameters are fitted independently for each color bin. Their variation between color bins serves as a consistency check and a way to assess the degeneracies, significance, and uniqueness of the best-fit values. The best-fit values are shown in the top four rows of Table 6 (bright photometric parallax relation) and the top five³³ rows of Table 7 (faint relation).

In all cases we are able to obtain good model fits, with reduced χ^2 in the range from 1.3 to 1.7. The best-fit solutions are mutually

³² Note also that being 0.1 mag wide, with typical magnitude errors of $\sigma_r \gtrsim 0.02$ mag, the adjacent bins are *not* independent. The histograms in Fig. 46 illustrate this well.

³³ The fit for the $0.9 < r - i < 1.0$ bin when using the faint photometric relation and including a halo component (see § 4.2.5) failed to converge to a physically reasonable value. We have therefore fitted this bin with disk components only.

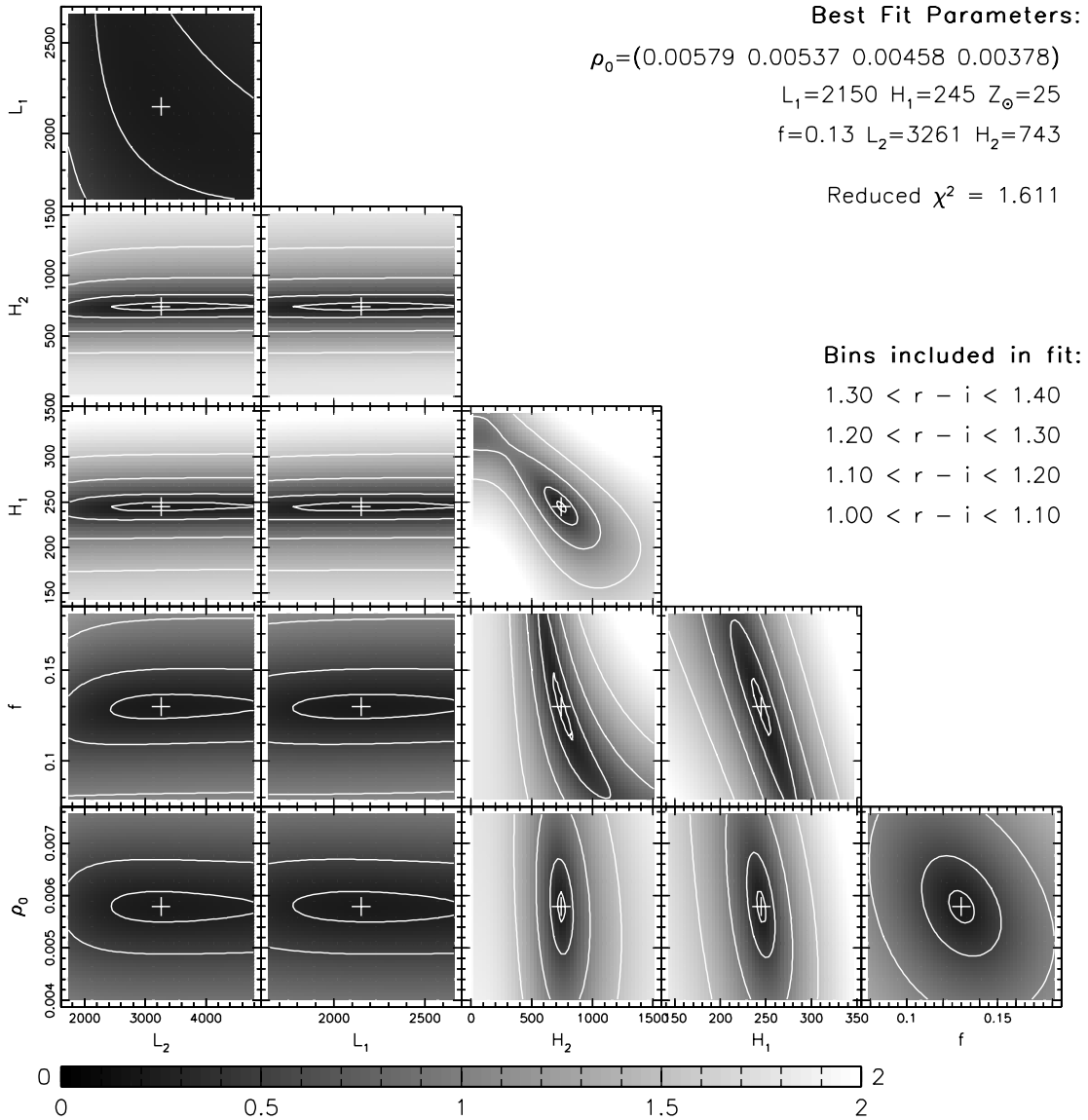


FIG. 21.—Two-dimensional cross sections of reduced χ^2 hypersurface around best-fit values for $1.0 < r - i < 1.4$ data (Table 3, first row). The fit was obtained assuming the “bright” photometric parallax relation (eq. [2]). Analogous cross sections for fits obtained assuming eq. (1) (Table 4, first row) show qualitatively the same features. The innermost contour is at the $1.1\chi_{\min}^2$ level, while the rest are logarithmically spaced in steps of 0.5 dex, starting at $\log \chi^2 = 0.5$.

consistent. In particular, the thin disk scale height is well constrained to $H_1 = 250$ pc (bright) and $H_1 = 230$ – 240 (faint), as are the values of $\rho(R_\odot, 0)$ which give the same results in individual and joint fits at the $\sim 5\%$ level.

The thick-to-thin disk density normalization is $\sim 10\%$, with $f = 0.10$ – 0.13 (bright) and 0.10 – 0.14 (faint). The thick disk scale length solutions are in the $H_2 = 750$ – 900 pc (bright) and 660 – 900 pc (faint) range. Thick disk normalization and scale heights appear less well constrained; however, note that the two are strongly correlated (f vs. H_2 panel in Fig. 21). As an increase in density normalization leads to a decrease in disk scale height and vice versa with no appreciable effect on χ^2 , any two models with so correlated differences of scale height and normalization of up to 20% to 30% are practically indistinguishable. This interplay between f and H_2 is seen in Tables 6 and 7, most extremely for the $1.1 < r - i < 1.2$ bin (Table 7, third row). With this in mind, the fits are still consistent with a single thick disk scale height H_2 and density normalization f describing the stellar number density distribution in all $r - i > 1.0$ color bins.

Constraints on disk scale lengths are weaker, with the goodness of fit and the values of other parameters being relatively insensitive to the exact values of L_1 and L_2 (Fig. 21, *left two columns*). This is mostly due to a short observation baseline in the radial (R) direction. The best-fit parameters lie in the range of $L_1 = 1600$ – 2400 pc, $L_2 = 3200$ – 6000 pc (bright) and $L_1 = 1600$ – 3000 pc, $L_2 = 3000$ – 6000 pc (faint parallax relation). Note that the two are anticorrelated (Fig. 21, *top left*), and combinations of low L_1 and high L_2 or vice versa can easily describe the same density field with similar values of reduced χ^2 (the behavior seen in Tables 6 and 7). The disk scale length fits in individual color bins are also consistent with there being a single pair of scale lengths L_1 and L_2 applicable to all color bins.

4.2.4. Halo Fits

For bluer color bins ($r - i < 1.0$), the probed distance range is larger, and the stellar halo component starts to appreciably contribute to the total density near the far edge of the survey volume. As seen in the middle and bottom panels of Figure 15,

TABLE 5
HALO SHAPE AND PROFILE FIT

Parallax Relation	χ^2	q_H	n_H
Bright	3.05	0.64 ± 0.01	2.77 ± 0.03
Faint	2.48	0.62 ± 0.01	2.78 ± 0.03

NOTE.—Best-fit values of halo power-law index n_H and axis ratio $q_H = c/a$, assuming the “bright” (top row) and “faint” (bottom row) photometric parallax relation.

the disk-only solution becomes visibly unsatisfactory at $Z \gtrsim 4000$ kpc. In addition, the reduced χ^2 values of disk-only models begin to climb to higher than a few once we attempt to fit them to data in $r - i < 1.0$ bins.

Before we move on to adding and fitting the halo component, there are a few significant caveats that must be discussed, understood, and taken into account. First, the presence of clumpiness and merger debris in the halo, if unaccounted for, will almost certainly bias (and make difficult or even impossible to determine) the model parameters. An initial survey of the density field (§ 2.3), the identification, and careful removal of identified overdensities (§ 4.1) are *essential* for obtaining a reasonable fit.

Second, the photometric parallax relations (eqs. [1] and [2]) do not explicitly depend on stellar metallicity. Implicitly, as discussed in § 2.2.1, they take metallicity into account by virtue of being calibrated to disk M dwarfs on the red end and metal-poor halo stars at the blue end. This makes them correct for low-metallicity stars ($[\text{Fe}/\text{H}] \lesssim -1.5$) near $r - i \sim 0.15$ and high metallicity ($[\text{Fe}/\text{H}] \gtrsim -0.5$) at $r - i \gtrsim 0.7$. They are therefore appropriate for the study of halo shape and parameters *only at the blue end* and disk shape and parameters *only on the red end*. Conversely, they are inappropriate for the study of disk shape and parameters at the blue end or halo shape and parameters at the red end. For the same reason, it is difficult to simultaneously fit the halo and the disk in the intermediate $r - i$ bins, as the application of a photometric parallax relation inappropriate for the low-metallicity halo induces distortions of halo shape in the density maps.

Therefore, to measure the shape of the halo, we only select the data points from the three bluest, $0.1 < r - i < 0.25$, bins and only in regions of (R, Z) -plane where a fiducial $q_H = 0.5$, $n_H = 2.5$, $f_H = 0.001$ halo model predicts the fraction of disk stars to be less than 5%. This allows us to fit for the power-law index n_H and the axis ratio q_H of the halo. Because we explicitly excluded the disk, we cannot fit for the halo-to-thin disk normalization f_H (but see § 4.2.5 below for a workaround).

The best-fit parameters obtained for the halo are shown in Table 5 for both the bright and faint photometric relations, and the reduced χ^2 surface for the fit is shown in Figure 22 (bright relation only; the surface looks qualitatively the same for the fit made assuming the faint relation).

The fits are significantly poorer than for the disks, with reduced $\chi^2 = 2-3$. Formal best-fit halo parameters are $n_H = 2.8$ and $q_H = 0.64$, but given the relatively high and shallow minimum and the shape of the χ^2 surfaces in Figure 22, it is better to think of the fit results as constraining the parameters to a range of values—the power-law index to $n_H = 2.5-3$ and the oblateness parameter to $q_H = 0.5-0.8$.

Figure 23 shows residual maps for the bluest color bin and for four different halo models, with the thin and thick disk parameters kept fixed at values determined using redder bins (Table 3). Individual panels illustrate the changes in residuals when the halo power-law index is varied while keeping the axis ratio fixed (*top*

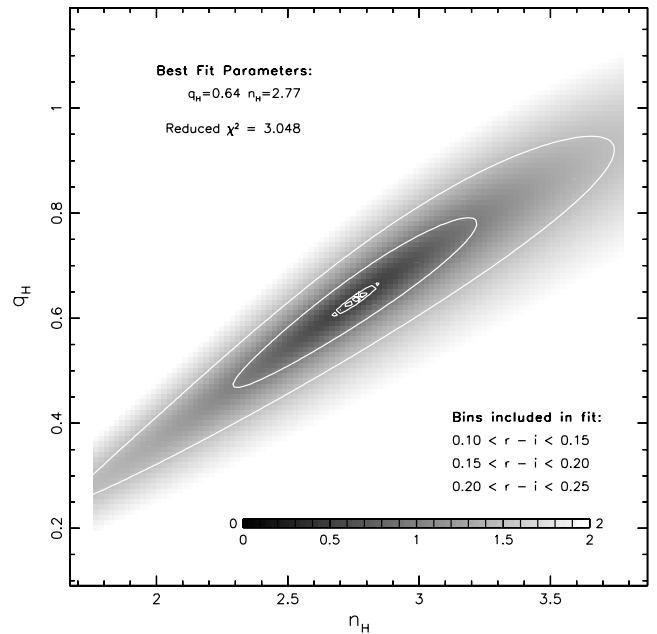


FIG. 22.—Reduced χ^2 surface of halo parameters n_H and q_H around the best-fit values (Table 5, first row). The innermost contour is at the $1.1\chi_{\min}^2$ level, while the rest are logarithmically spaced in steps of 0.5 dex, starting at $\log \chi^2 = 0.5$.

row) and when the ellipticity of the halo is changed from oblate to spherical while keeping the power-law index n_H fixed (*bottom row*). The Monoceros and Virgo overdensities and the overdensity at $R \sim 6.5$ kpc and $Z \sim 1.5$ kpc are clearly evident, but their detailed properties depend significantly on the particular halo model subtracted from the data.

We further find that a power-law halo model always over- or underestimates the stellar counts in the far outer halo (Fig. 23), suggesting that the use of a different profile may be more appropriate and consistent with “dual-halo” profiles favored by (among others) Sommer-Larsen & Zhen (1990), Allen et al. (1991), Zinn (1993), Carney et al. (1996), and Chiba & Beers (2000) and more recently discussed by Siegel et al. (2002).

However, no matter what the exact shape of the profile or the power-law index is, only significantly oblate halos provide good fits to the data (compare the bottom right panel to other panels in Fig. 23). Specifically, given the reduced χ^2 surface in Figure 22, a spherical or prolate halo can be ruled out, and this remains the case irrespective of the details of the photometric parallax relation.³⁴

4.2.5. Simultaneous Disk and Halo Fits

Keeping the best-fit values of halo shape parameters q_H and n_H constant, we next attempt to simultaneously fit the thin and thick disk parameters and the halo normalization, f_H , in four $0.65 < r - i < 1.0$ bins. These bins encompass regions of (R, Z) -space where the stellar number density due to the halo is not negligible and has to be taken into account. Simultaneous fits of both the disk and all halo parameters are still unfeasible, both because halo stars still make up only a small fraction of the total number density and due to poor applicability of the disk-calibrated photometric parallax relations in this $r - i$ range to low-metallicity halo stars. However, knowing the halo shape from the blue, low-metallicity

³⁴ Aspherical halos could be artificially favored by the χ^2 analysis, as a way to parameterize away any existing halo inhomogeneity. However, given the analysis of residuals in § 4.3.8, we consider this to be a very unlikely explanation of the measured oblateness.

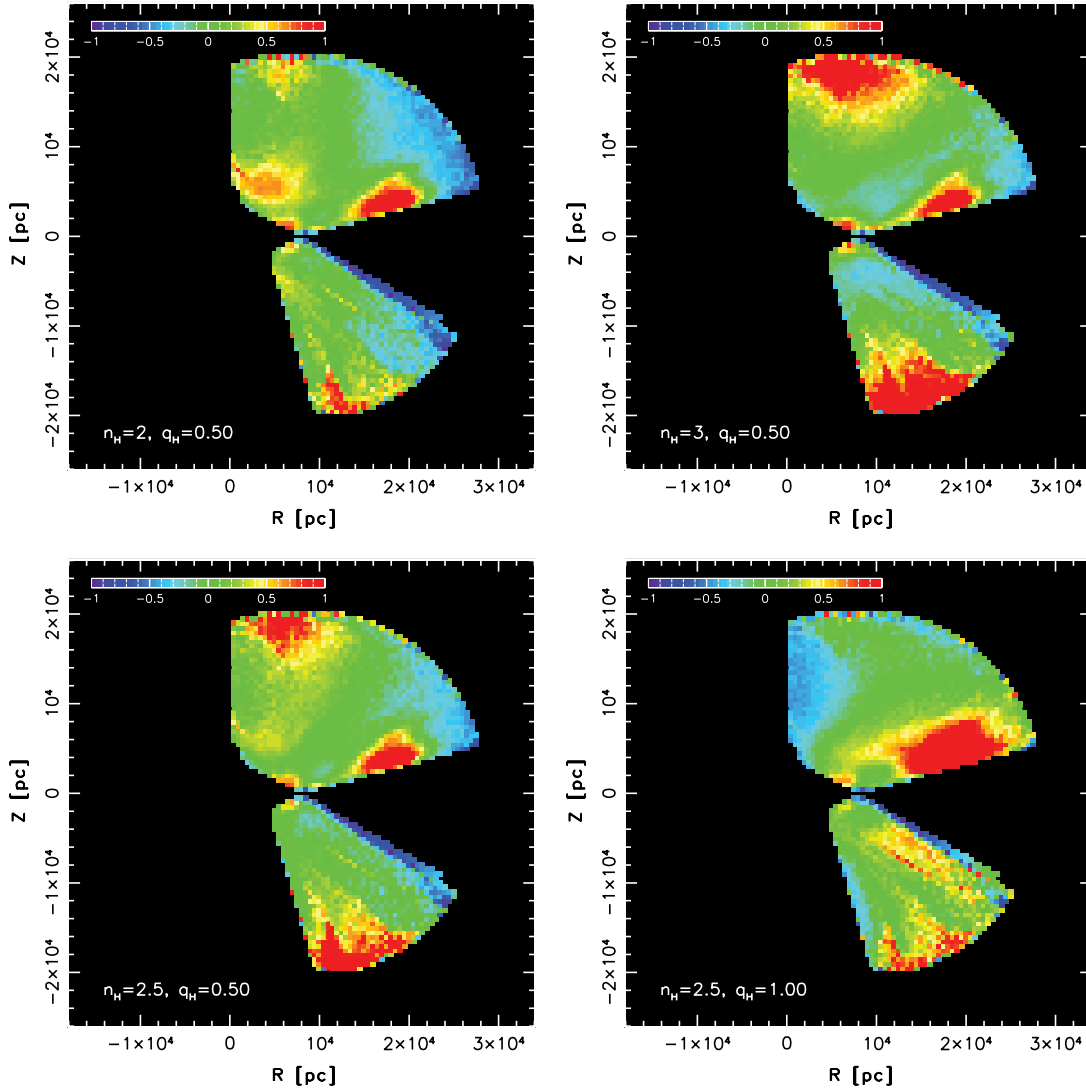


FIG. 23.—Data-model residuals, normalized to the model, for color bin $0.10 < r - i < 0.15$, using four different halo models. All four models have identical thin and thick disk parameters, and only the halo parameters are varied. Panels in the top row illustrate the changes in residuals when the halo power-law index n_H is varied while keeping the axis ratio fixed. Panels of the bottom row illustrate the effects of axis ratio q_H change, while keeping the power-law index constant. While n_H is not strongly constrained, the data strongly favor an oblate halo.

calibrated bins, we may keep q_H and n_H fixed and fit for the halo-to-thin disk normalization, f_H . Given the uncertainty in its current knowledge, the thusly obtained value of f_H is still of considerable interest despite the likely biases.

We follow the procedure outlined in § 4.2.3 and fit the data in $0.65 < r - i < 1.0$ bins jointly for all and separately in each color bin, with both bright and faint photometric parallax relations. The results of the joint fits are given in the bottom rows of Tables 3 and 4. Results for individual bins are given in the bottom rows of Tables 6 and 7 for the bright and faint photometric relations, respectively.

We obtain satisfactory model fits, with reduced χ^2 in the 1.4–2.0 range. As was the case for fits to $r - i > 1.0$ bins, the best-fit disk parameter values are consistent between bins and with the joint fit. The reduced χ^2 surface cross sections, shown in Figure 24, are qualitatively the same as those in Figure 21, and the entire discussion of § 4.2.3 about fit parameters and their interdependencies applies here as well.

Comparison of the top and bottom rows in Tables 3 and 4 shows consistent results between $r - i > 1.0$ and $0.65 < r - i < 1.0$

bins. In particular, the scale heights of the thin disk are the same, and the thick-to-thin disk normalization is the same to within 8%–15%, still within fit uncertainties. The scale lengths are still poorly constrained and on average 10%–30% larger than in disk-only fits. Given the poor constraint on scale lengths, it is difficult to assess whether this effect is physical or if it is a fitting artifact due to the addition of the stellar halo component. The scale height of the thick disk H_2 is $\sim 14\%$ smaller than in disk-only fits. This is likely due to the reassignment to the halo of a fraction of the stellar number density previously assigned to the thick disk.

For f_H , the halo-to-thin disk normalization at ($R = 8$ kpc, $Z = 0$), the best-fit values are in the 0.3%–0.6% range, with the best-fit value for joint fits being $f_H = 0.5\%$ both for the bright and faint parallax relations. In particular, note how insensitive f_H is to the choice of the photometric parallax relation. In this region of $r - i$ colors, the average difference between the bright and faint parallax relations is $\Delta M_r = 0.25$ mag; therefore, even in case of uncertainties of \sim half a magnitude, the change in f_H will be no greater than $\sim 10\%$ – 20% .

TABLE 6
BEST-FIT VALUES (INDIVIDUAL FITS, BRIGHT PARALLAX RELATION)

Color Bin	χ^2	$\rho(R_\odot, 0)$	L_1	H_1	f	L_2	H_2	f_H
1.3 < $r - i$ < 1.4	1.34	0.0062	1590	247	0.09	5989	909	...
1.2 < $r - i$ < 1.3	1.31	0.0055	1941	252	0.11	5277	796	...
1.1 < $r - i$ < 1.2	1.58	0.0049	2220	250	0.09	3571	910	...
1 < $r - i$ < 1.1	1.64	0.0039	2376	250	0.10	3515	828	...
0.9 < $r - i$ < 1	1.38	0.0030	3431	248	0.14	2753	602	0.0063
0.8 < $r - i$ < 0.9	1.48	0.0028	3100	252	0.10	3382	715	0.0039
0.7 < $r - i$ < 0.8	1.83	0.0024	3130	255	0.09	3649	747	0.0037
0.65 < $r - i$ < 0.7	1.69	0.0011	2566	273	0.05	8565	861	0.0043

NOTES.—Best-fit values of Galactic model parameters, fitted separately for each $r - i$ bin assuming the “bright” photometric parallax relation (eq. [2]). In fits which include the halo component, the shape of the halo was kept fixed (Table 5, top row), and only the normalization f_H was allowed to vary.

4.3. Analysis

The Galactic model parameters as fitted in § 4.2 are biased³⁵ by unrecognized stellar multiplicity, finite dispersion of the photometric parallax relation, and photometric errors. They are further made uncertain by possible systematics in calibration of the photometric parallax relations and a simplified treatment of stellar metallicities.

In this section we analyze all of these (and a number of other) effects on a series of Monte Carlo-generated mock catalogs and derive the corrections for each of them. We also look at the resolved local overdensities found in the data and discuss the question of possible statistical signatures of further unresolved overdensities and questions of uniqueness and degeneracy of our best-fit model. After deriving the bias correction factors, we close the section by summarizing and writing out the final debiased set of best-fit SDSS Galactic model parameters, together with their assumed uncertainties.

4.3.1. Monte Carlo-generated Mock Catalogs

To test the correctness of the data processing and fitting procedure and derive the correction factors for Malmquist bias, stellar multiplicity, and uncertainties due to photometric parallax systematics, we developed a software package for generating realistic mock star catalogs. These catalogs are fed to the same data-processing pipeline and fit in the same manner as the real data.

The mock catalog generator, given an arbitrary Galactic model (which in our case is defined by eqs. [21]–[24], a local position-

independent luminosity function, and binary fraction), generates a star catalog within an arbitrarily complex footprint on the sky. The code can also include realistic magnitude-dependent photometric errors (Fig. 7, *bottom*) and the errors due to Gaussian dispersion σ_{M_r} around the photometric parallax mean, $M_r(r - i)$.

Using this code, we generate a series of mock catalogs within the footprint of the SDSS data used in this study (Fig. 6) using a fiducial model with parameters listed in the top row of Table 8. For the luminosity function, we use the Kroupa et al. (1993) luminosity function, transformed from $\phi(M_r)$ to $\phi(M_r)$ and re-normalized to $\rho(R = 8000, Z = 0) = 0.04$ stars $\text{pc}^{-3} \text{mag}^{-1}$ in the $1.0 < r - i < 1.1$ bin. Since we make comparisons between the simulation and $r - i > 1.0$ bins, we do not include the halo component ($f_H = 0$).

For all tests described in the text to follow, we generate the stars in the $0.7 < r - i < 1.6$ color and $10 < r < 25$ magnitude range, which is sufficient to include all stars that may possibly scatter into the survey flux ($15 < r < 21.5$) and disk color bin ($1.0 < r - i < 1.4$) limits, either due to photometric errors, uncertainty in the photometric parallax relation, or an added binary companion. To transform from distance to magnitude, we use the bright photometric parallax relation (eq. [4]).

4.3.2. Correctness of Data Processing and Fitting Pipeline

We first test for the correctness of the data processing and fitting pipeline, by generating a “perfect” catalog. Stars in this catalog have no photometric errors added, and their magnitudes and colors are generated using equations (2) and (5).

We fit this sample in the same manner as the real data in § 4.2.3. The results are given in the second row of Table 8. The fit recovers

TABLE 7
BEST-FIT VALUES (INDIVIDUAL FITS, FAINT PARALLAX RELATION)

Color Bin	χ^2	$\rho(R_\odot, 0)$	L_1	H_1	f	L_2	H_2	f_H
1.3 < $r - i$ < 1.4	1.32	0.0064	1599	246	0.09	5800	893	...
1.2 < $r - i$ < 1.3	1.40	0.0064	1925	242	0.10	4404	799	...
1.1 < $r - i$ < 1.2	1.56	0.0056	2397	221	0.17	2707	606	...
1 < $r - i$ < 1.1	1.71	0.0049	2931	236	0.10	2390	760	...
0.9 < $r - i$ < 1	1.62	0.0043	3290	239	0.07	2385	895	...
0.8 < $r - i$ < 0.9	1.69	0.0038	2899	231	0.08	2932	759	0.0021
0.7 < $r - i$ < 0.8	2.59	0.0034	2536	227	0.09	3345	671	0.0033
0.65 < $r - i$ < 0.7	1.92	0.0016	2486	241	0.05	6331	768	0.0039

NOTES.—Best-fit values of Galactic model parameters, fitted separately for each $r - i$ bin assuming the “faint” photometric parallax relation (eq. [1]). In fits which include the halo component, the shape of the halo was kept fixed (Table 5, bottom row), and only the normalization f_H was allowed to vary.

³⁵ Or “apparent,” in the terminology of Kroupa et al. (1993).

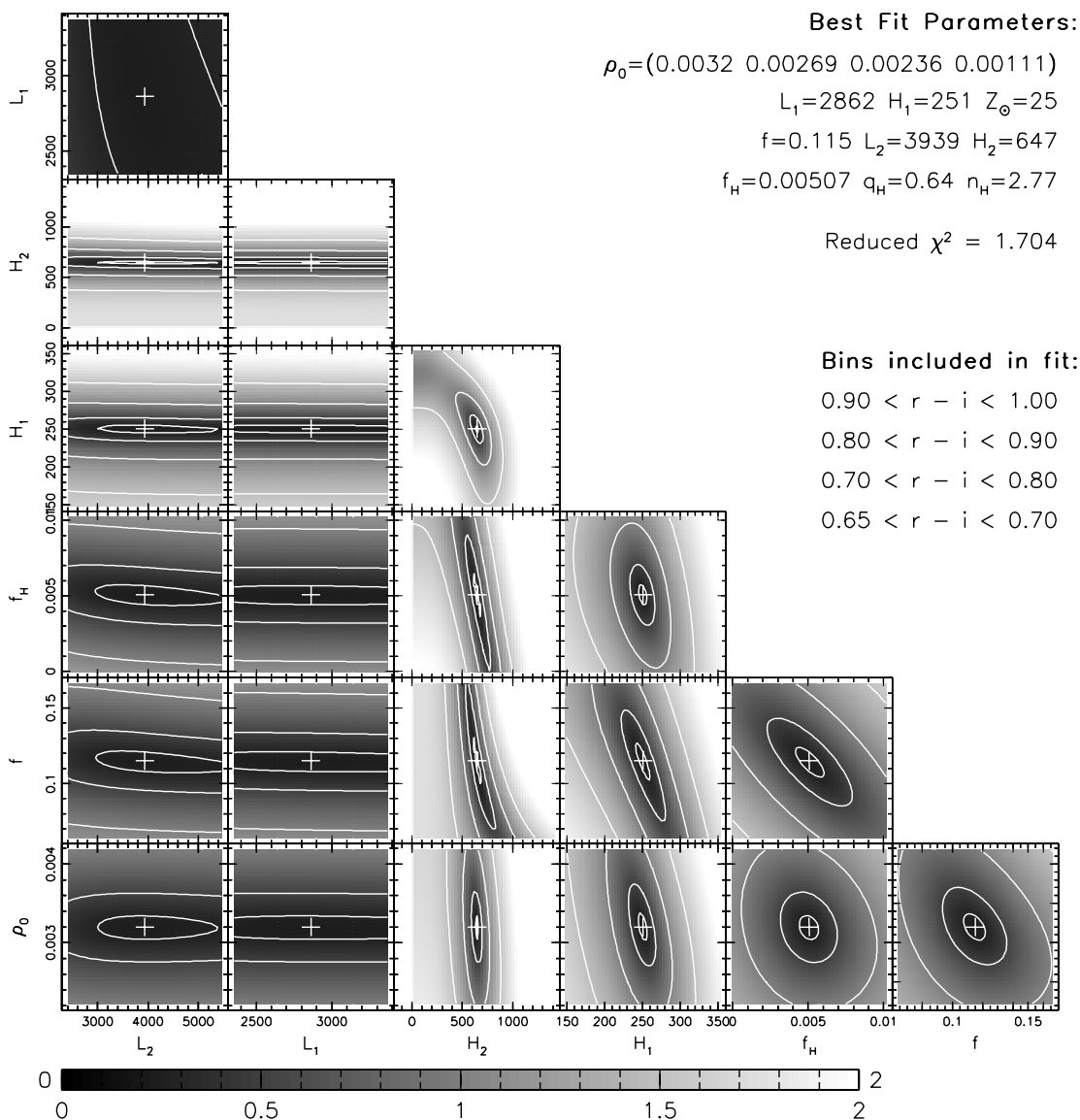


FIG. 24.—Two-dimensional cross sections of reduced χ^2 hypersurface around best-fit values for $0.65 < r - i < 1.0$ data (Table 3, second row). The fit was obtained assuming the “bright” photometric parallax relation (eq. [2]) and includes the contribution of the halo. Analogous cross sections for fits obtained assuming eq. (1) (Table 4, second row) show qualitatively the same features. The innermost contour is at the $1.1\chi_{\min}^2$ level, while the rest are logarithmically spaced in steps of 0.5 dex, starting at $\log \chi^2 = 0.5$.

TABLE 8
MONTE CARLO-GENERATED CATALOG FITS

Simulation	χ^2	L_1	H_1	f	L_2	H_2
True Model	2500	240	0.10	3500	770
Perfect Catalog.....	1.03	2581 ± 44	244 ± 2	0.094 ± 0.009	3543 ± 69	791 ± 18
Photometric and Parallax Errors.....	0.95	2403 ± 40	230 ± 2	0.111 ± 0.010	3441 ± 57	725 ± 13
25% Binary Fraction.....	0.97	2164 ± 39	206 ± 1	0.119 ± 0.011	3199 ± 47	643 ± 9
50% Binary Fraction.....	0.97	1986 ± 34	193 ± 1	0.115 ± 0.011	2991 ± 41	611 ± 7
100% Binary Fraction.....	1.02	1889 ± 31	178 ± 1	0.104 ± 0.010	2641 ± 31	570 ± 6

NOTES.—The true model parameters (top row) and the best-fit values of model parameters recovered from a series of Monte Carlo-generated catalogs. These test the correctness of the data processing pipeline and the effects of cosmic variance (“Perfect Catalog”), the effects of photometric parallax dispersion and photometric errors (“Photometric and Parallax Errors”), and the effects of varying fraction of unresolved binary stars in the data (last three rows).

TABLE 9
EFFECTS OF $M_r(r-i)$ CALIBRATION ERRORS

Simulation	χ^2	L_1	H_1	f	L_2	H_2
$M_r(r-i) - 0.5$	1.18	3080 ± 55	305 ± 4	0.123 ± 0.011	4881 ± 78	976 ± 19
$M_r(r-i)$	0.95	2403 ± 40	230 ± 2	0.111 ± 0.010	3441 ± 57	725 ± 13
$M_r(r-i) + 0.5$	1.23	1981 ± 32	198 ± 2	0.138 ± 0.013	3091 ± 52	586 ± 11

NOTES.—Effects of systematic error in the calibration of photometric parallax relation. Middle row lists the parameters recovered assuming the correct parallax relation (eq. [2]), from a Monte Carlo-generated catalog with realistic photometric errors and dispersion $\sigma_{M_r} = 0.3$ mag around the mean of $M_r(r-i)$. This is the same catalog as in the third row of Table 8. The first and last rows show parameters recovered when a parallax relation which systematically under-/overestimates the absolute magnitudes by 0.5 mag (over-/underestimates the distances by $\sim 23\%$) is assumed.

the original model parameters, with the primary source of error being the “cosmic variance” due to the finite number of stars in the catalog.

This test confirms that fitting and data processing pipelines introduce no additional uncertainty to best-fit model parameters. It also illustrates the limits to which one can, in principle, determine the model parameters from our sample assuming that (1) stars are distributed in a double exponential disk and (2) the three-dimensional location of each star is perfectly known. These limits are about 1%–2%, significantly smaller than all other sources of error.

4.3.3. Effects of Malmquist Bias

We next test for the effects of photometric errors and the errors due to the finite width of the photometric parallax relation. We model the photometric errors as Gaussian, with a magnitude-dependent dispersion σ_r measured from the data (Fig. 7, *bottom*). Median photometric errors range from $\sigma_r = 0.02$ on the bright to 0.12 on the faint end. We assume the same dependence holds for g and i bands as well. We model the finite width of the photometric parallax relation as a Gaussian $\sigma_{M_r} = 0.3$ dispersion around the mean of $M_r(r-i)$. The two sources of effective photometric error add up in quadrature and act as a source of a Malmquist bias, with the photometric parallax relation dispersion giving the dominant effect (eq. [12]).

The best-fit parameters obtained from this sample are given in the third row of Table 8. The thin and thick disk scale heights are underestimated by $\sim 5\%$. The density normalization f is overestimated by $\sim 10\%$ (note however that this is still within the statistical uncertainty). The scale lengths are also slightly underestimated, with the effect less pronounced for the thick disk. We conclude that the Malmquist bias due to photometric errors and the dispersion around the photometric parallax relation has a relatively small effect on the determination of Galactic model parameters, at the level of $\sim 5\%$.

4.3.4. Effects of Unrecognized Multiplicity

Unrecognized multiplicity biases the density maps and the determination of Galactic model parameters by systematically making unresolved binary stars, when misidentified as a single star, appear closer than they truly are. Its effect is most strongly dependent on the fraction of observed “stars,” f_m , that are in fact unresolved multiple systems.

We model this effect by simulating a simplified case where all multiple systems are binaries. Because the fraction of binary systems is poorly known, we generate three mock catalogs with varying fractions f_m of binary systems misidentified as single stars and observe the effects of f_m on the determination of model parameters. Photometric errors and photomet-

ric parallax dispersion (as discussed in § 4.3.3) are also mixed in.

The results are given in the bottom three rows of Table 8. The effect of unresolved binary systems is a systematic reduction of all spatial scales of the model. Measured disk scale heights are underestimated by as much as 25% ($f_m = 1$), 20% ($f_m = 0.5$), and 15% ($f_m = 0.25$). Measured scale lengths are similarly biased, with the thin disk scale length being underestimated by 25%, 20%, and 13% and the thick disk scale length by 25%, 15%, and 9% for $f_m = 1, 0.5$, and 0.25, respectively. The thick disk density normalization is mildly overestimated ($\sim 10\%$) but not as strongly as the disk scales, and is still within statistical uncertainty.

4.3.5. Effects of Systematic Distance Determination Error

We next measure the effect of systematically over- or underestimating the distances to stars due to absolute calibration errors of the photometric parallax relation. This can already be judged by comparing the values of model parameters determined from fits using the bright and faint photometric parallax relations (Tables 3 and 4), but here we test it on a clean simulated sample with a known underlying model.

We generate a mock catalog by using the bright photometric parallax relation (eq. [2]) to convert from distances to magnitudes and mix in SDSS photometric and parallax dispersion errors (§ 4.3.3). We process this catalog by assuming a parallax relation 0.5 mag brighter and 0.5 mag fainter than equation (2), effectively changing the distance scale by $\pm 23\%$.

Fit results are shown in Table 9, including for comparison in the second row the parameters recovered using the correct $M_r(r-i)$ relation. The effect of systematic distance errors is to comparably increase or decrease measured geometric scales. The thin and thick disk scale heights increase by 33% and 34% and the scale lengths by 28% and 42%, respectively, if the distances are overestimated by 23%. If they are underestimated by the same factor, the parameters are reduced by 14% and 19% (thin and thick disk scale height) and 18% and 10% (thin and thick disk scale lengths). Interestingly, both increasing and decreasing the distance scale results in an *increase* of measured normalization, by a factor of $\sim 10\%$ –25%.

4.3.6. Test of Cylindrical Symmetry

In § 3.1 we argued based on the shapes of isodensity contours in Figures 12–14 and in particular in Figure 11 that once the large overdensities are taken out, the Galactic density distribution is cylindrically symmetric. Therefore, it was justifiable for the purpose of determining the overall Galactic stellar number density distribution to measure the density along the same galactocentric annuli R and only consider and model the distribution of stars in the two-dimensional R - Z plane.

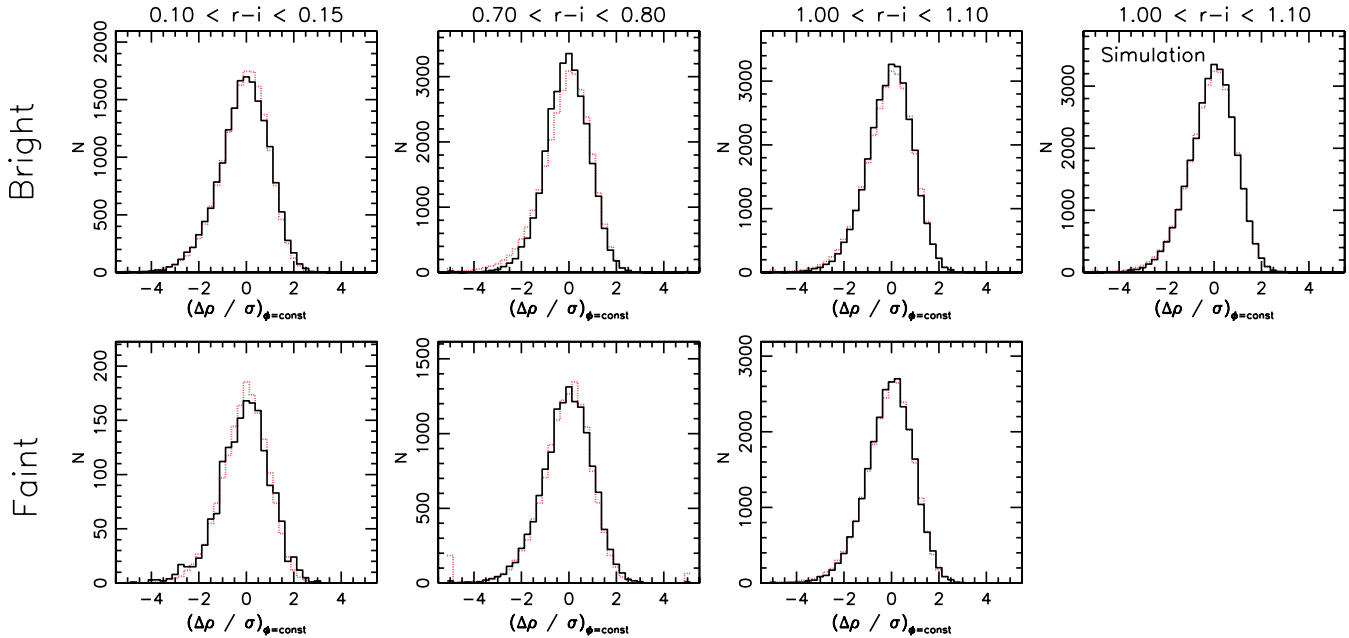


FIG. 25.—Distribution of noise-normalized deviations of density in pixels (X, Y, Z) from the mean density measured along their corresponding annuli $[R = (X^2 + Y^2), Z]$. Black solid-line histogram shows the data. Red dotted-line histogram shows a Poisson noise model. Histograms in the top and bottom rows have been calculated assuming the bright (eq. [2]) and faint (eq. [1]) photometric parallax relation, respectively. The rightmost panel in the top row shows the same distributions derived from a Monte Carlo–simulated catalog, with 25% unresolved binary fraction, $\sigma_{M_r} = 0.3$ parallax dispersion, and SDSS photometric errors.

Using Figure 25 we quantitatively verify this assumption. In the panels of the top row as solid-line black histograms we plot the distribution of

$$\frac{\Delta\rho}{\sigma} = \frac{\rho(R, \phi, Z) - \bar{\rho}(R, Z)}{\sigma_P(R, \phi, Z)} \quad (27)$$

for four $r - i$ color bins.³⁶ This is the difference of the density measured in a pixel at (R, ϕ, Z) and the mean density $\bar{\rho}(R, Z)$ at annulus (R, Z) , normalized by the expected Poisson fluctuation $\sigma_P(R, \phi, Z) = [N(R, \phi, Z)]^{1/2}/V(R, \phi, Z)$.

The red dotted-line histogram in the panels shows a Poisson model of noise-normalized deviations expected to occur due to shot noise only. If all pixels were well sampled ($N \gtrsim 50$ stars, which is not the case here), this distribution would be a $\mu = 0$, $\sigma = 1$ Gaussian.

The data and the Poisson model show a high degree of agreement. However, in a strict statistical sense, for all but the $1.3 < r - i < 1.4$ bin the data and the model are inconsistent with being drawn from the same distribution at a 5% confidence level. This is not very surprising, as the effects of unresolved multiplicity and other observational errors may modify the residual distribution. We verify this by examining the same statistic calculated from a Monte Carlo–generated catalog with a 25% unresolved binary fraction and mixed in photometric error (Table 8, fourth row). The resulting “observed” and Poisson model histograms for the simulated catalog are shown in the top rightmost panel of Figure 8. They show the same behavior as seen in the data.

One may ask if these distributions could be used to further test (and/or constrain) the photometric parallax relations, as under- or overestimating the distances will break the cylindrical symmetry of the Galaxy and distort the isodensity contours. The answer is, unfortunately, no. In the bottom row of Figure 25 we show the distributions analogous to those in the top row, but calculated from

maps obtained using the faint parallax relation (eq. [1]). They are very similar to those in the top row, with no deviations that we can conclusively attribute to the change in photometric parallax relation, although there is an intriguing slightly better data-model agreement in the $0.7 < r - i < 0.8$ color bin for the faint relation than for the bright one. This is initially surprising, as one would intuitively expect the erroneous distance estimate to map the density from different real galactocentric annuli (R, Z) to the same observed (R_o, Z_o) and, therefore, widen the residual distribution. However, this effect (as we verified using the Monte Carlo–generated catalogs) is indiscernible for the combination of density distribution seen in the Milky Way and the portion in (R, Z) -space where we have clean data. The region near $R = 0$ where the assumption of cylindrical symmetry is most sensitive to errors in distance determination is contaminated by debris from the Virgo overdensity, making it unusable for this particular test.

4.3.7. Resolved Substructure in the Disk

The panels in Figure 26 illustrate the fitting results and the revealed clumpy substructure. The columns, from left to right, show the data, the model, and the model-normalized residuals. The bottom three rows are results of fitting a disk-only model, while the top row also includes a fit for the halo.

While the best-fit models are in good agreement with a large fraction of the data, the residual maps show some localized features. The most prominent feature is found at practically the same position ($R \sim 6.5$ kpc and $Z \sim 1.5$ kpc) in all color bins and, in Figure 26, is the most prominent in the top right panel. The feature itself is not symmetric with respect to the Galactic plane, although a weaker counterpart seems to exist at $Z < 0$. It may be connected to the feature observed by Larsen & Humphreys (1996) and Parker et al. (2003) in the POSS I survey at $20^\circ < l < 45^\circ$, $b \sim 30^\circ$ and which they interpreted at the time as a signature of thick disk asymmetry. We also show it in an X - Y slice on the middle panel of Figure 27, where it is revealed to have a ringlike structure, much like the Monoceros stream in Figure 13. Another

³⁶ Analogous histograms of other $r - i$ bins share the same features.

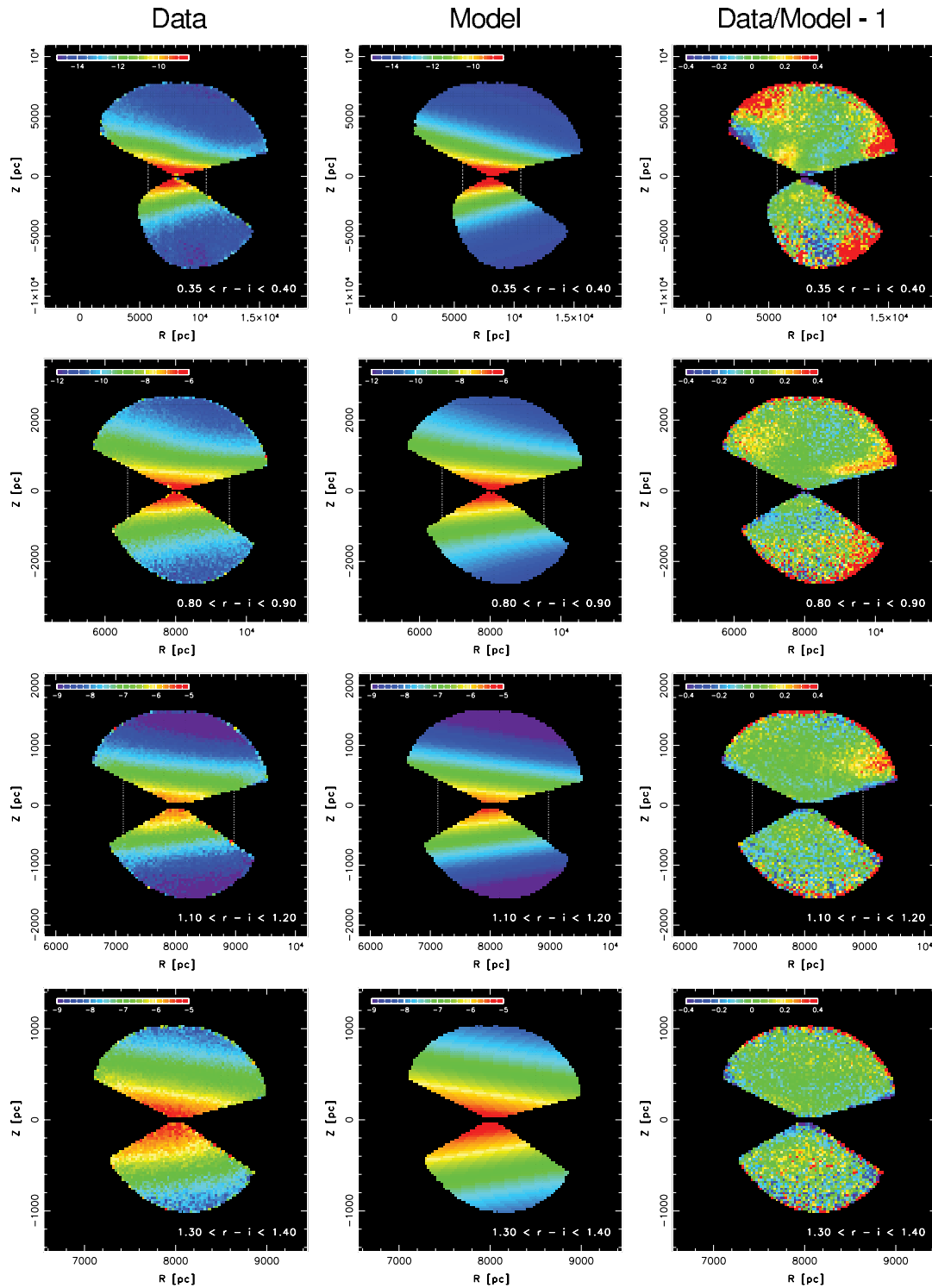


FIG. 26.—Examples of model fits for four color bins, one per row. Note the different scales. The left panel of each row shows the data, the middle panel shows the best-fit model, and the right panel shows (data-model) residuals, normalized to the model. The residuals are shown on a linear stretch, from -40% to $+40\%$. Note the excellent agreement of the data and the model for reddest color bins (*bottom row*) and an increasing number of overdensities as we move toward bluer bins. In the residuals map for the $0.35 < r - i < 0.40$ bin (*top row*), the edges of the Virgo overdensity (*top right*) and the Monoceros stream (*left*), the overdensity at $(R \sim 6.5, Z \sim 1.5)$ kpc, and a small overdensity at $(R \sim 9.5, Z \sim 0.8)$ kpc (*a few red pixels*) are easily discernible. The apparently large red overdensity in the south at $(R \sim 12, Z \sim -7)$ kpc is an instrumental effect and not a real feature.

smaller overdensity is noticeable in all but the reddest data-model panel of Figure 26 at $R \sim 9.5$ kpc and $Z \sim 0.8$ kpc, apparently extending for ~ 1 kpc in the radial direction. When viewed in an X - Y slice, it is also consistent with a ring (Fig. 27, *right*); however, due to the smaller area covered in the X - Y plane, an option

of it being a localized clumpy overdensity is not possible to exclude.

If this substructure is not removed from the disk as we have done in § 4.1, it becomes a major source of bias in the determination of model parameters. The effect depends on the exact location,

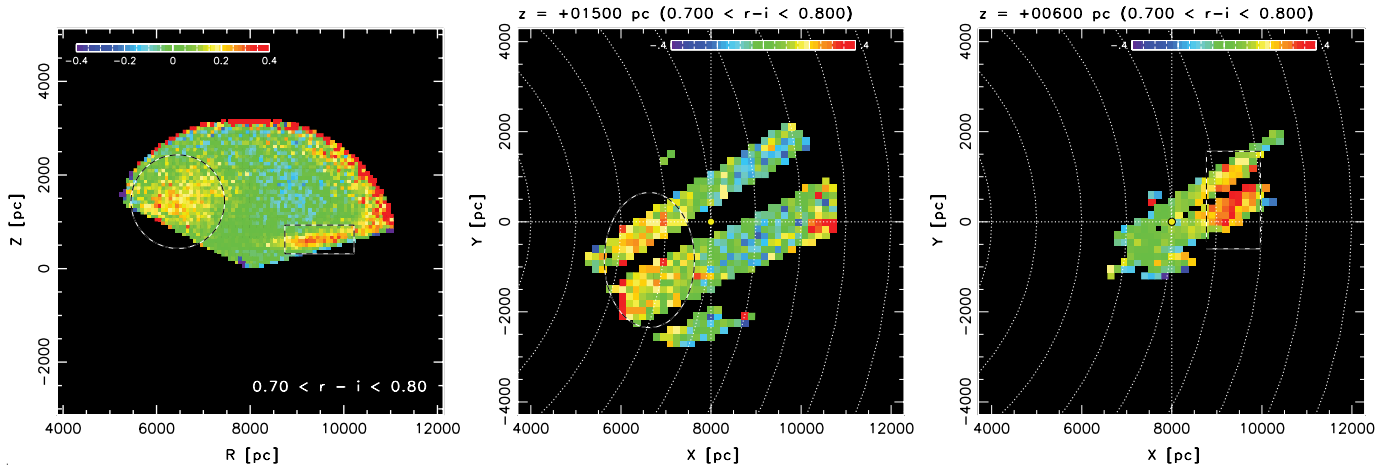


FIG. 27.—Ringlike deviations from the underlying density distribution detected after the best-fit model subtraction. The left panel shows the data-model residuals in the R - Z plane, normalized to the model, for the $0.7 < r - i < 0.8$ bin. Two overdensities detected on Fig. 26 are clearly visible and marked by a dashed circle and rectangle. In the X - Y plane, shown in the middle panel, the $R \sim 6.5$ kpc feature reveals itself as a ringlike $\sim 20\%$ density enhancement over the smooth background at $Z \sim 1.5$ kpc. Similarly on the right panel, the $R \sim 9.5$ feature is detectable as a strong $\sim 50\%$ enhancement in the $Z = 600$ pc slice.

size, and magnitude of each overdensity and whether the overdensity is inside the survey’s flux limit for a particular color bin. For example, the effect of the ($R \sim 6.5$, $Z \sim 1.5$) overdensity was to increase the scale of the thick disk, while reducing the normalization, to compensate for the excess number density at higher Z -values. The effect of the $R \sim 9.5$ overdensity was similar, with an additional increase in scale length of both disks to compensate for larger than expected density at $R > 9$ kpc. Furthermore, these effects occur only in bins where the overdensities are visible, leading to inconsistent and varying best-fit values across bins. Removal of the clumps from the data set prior to fitting the models (§ 4.1) restored the consistency.

4.3.8. Statistics of Best-Fit Residuals

The best-fit residuals of data where no apparent substructure was detected may hold statistical evidence of unrecognized low-contrast overdensities and clumpiness. If there are no such features in the data, the distribution of residuals will be consistent with a Poisson noise model. Conversely, if a substantial degree of unresolved clumpiness exists, the distribution of residuals will be wider and may be skewed compared to the distribution expected from Poisson noise only.

We begin by inspecting the statistics of residuals in the (R , Z)-plane, shown in Figure 28 for four color bins representative of the general behavior. The black solid-line histogram shows the distribution of the data-model deviation normalized by the shot noise. As pixels in the (R , Z)-plane are well sampled (typically, $N_{\text{stars}} > 50$ in more than 95% of pixels), the shot noise induced errors are Gaussian, and the residuals are expected to be normally distributed [$N(\mu = 0, \sigma = 1)$, dotted red curve] for a perfect model fit. The distribution seen in the data is wider than the expected Gaussian, by 10% at the red end and 85% at the blue end.

Two-dimensional (R , Z)-plane pixels contain stars from all (potentially distant) X - Y positions in the observed volume which map to the same R , thus making the residuals difficult to interpret. We therefore construct analogous distributions of residuals for pixels in three-dimensional (X , Y , Z)-space. They are shown in the panels of the left column of Figure 29 (black solid-line histograms). As not all (X , Y , Z) pixels are well sampled, full Poissonian noise model is necessary to accurately model the distribution of residuals. We overplot it on panels of Figure 29 as red dotted-line

histograms. In the left column of the same figure, we also plot the measured distribution of model-normalized residuals (black solid-line histogram) and the Poisson model prediction for residuals due to shot noise only (red dotted-line histogram). To judge the effects of observational errors and unresolved multiplicity, the bottom two panels show the distributions measured from a Monte Carlo-generated catalog with 25% unresolved binary fraction and photometric error (Table 8, fourth row). Comparison of data and Poisson models, and the observed and simulated distributions, leads us to conclude that across all examined color bins, the distribution of deviations is consistent with being caused by shot noise only.

This is in apparent conflict with the analysis of residuals in the two-dimensional (R , Z)-plane. The key in reconciling the two is to notice that different spatial scales are sampled in the three- and two-dimensional cases. The three-dimensional analysis samples scales comparable to the pixel size. The effective sampling scale is made variable and somewhat larger by the smearing in the line-of-sight direction due to unrecognized stellar multiplicity, but is still on the order of not more than a few pixel sizes. On the other hand, the effective scale in two dimensions is the length of the arc over which three-dimensional pixels were averaged to obtain the R - Z maps. This is on order of a few tens of percent of the faint volume-limiting distance (Table 2, column D_1) for each bin. The deviations seen in two-dimensional maps are therefore indicative of data-model mismatch on large scales, such as those due to large-scale overdensities or simply due to the mismatch of the overall shape of the analytic model and the observed density distribution.

In support of this explanation in Figure 30 we plot a rainbow-coded shot noise-normalized map of residuals in pixels at the $Z = 10$ kpc slice, $0.1 < r - i < 0.15$ color bin. On large scales a small but noticeable radial trend in the residuals is visible, going from slightly underestimating the data (larger median of residuals, more red pixels) at smaller R toward overestimating the data near the edge of the volume at higher R (smaller median of residuals, more blue pixels). This trend manifests itself as a widening of the residual distribution (and increase in χ^2) in Figure 28.

The small-scale fluctuations are visible as the “noisiness” of the data. They are locally unaffected by the large-scale trend and consistent with just Poisson noise superimposed on the local density background. If examined in bins along the R -direction, the

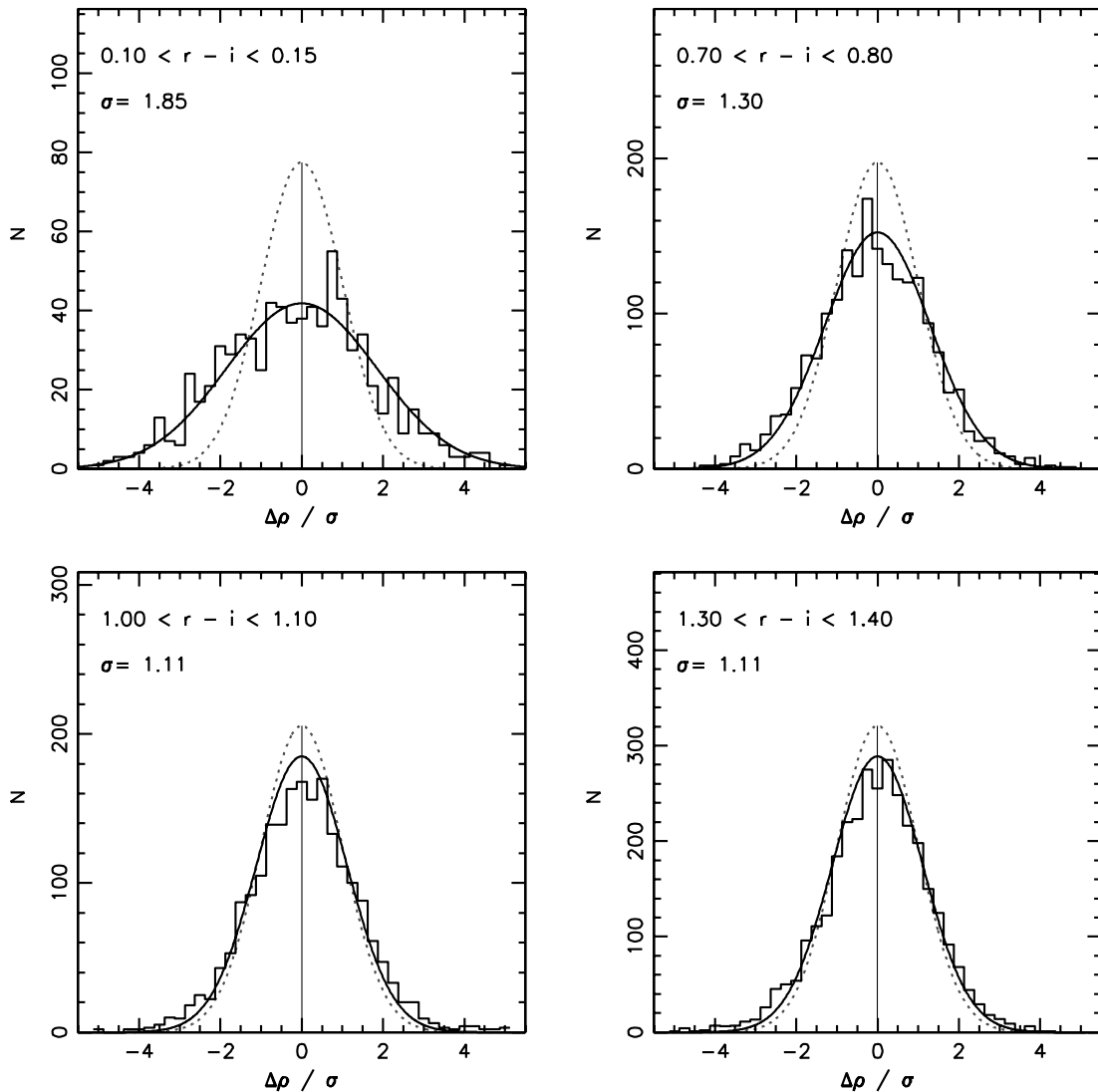


FIG. 28.—Distribution of residuals in (R, Z) -plane pixels. The black solid-line histogram shows the data, and the overplotted solid black curve is a Gaussian distribution with dispersion σ determined from the interquartile range of the data. For comparison, the dotted red line shows a $\sigma = 1$ Gaussian, the expected distribution if the residuals were due to shot noise only. [See the electronic edition of the *Journal* for a color version of this figure.]

large-scale trend does leave a trace; the median of residuals is slightly higher than expected from the Poisson model at low R and lower than expected at high R . But when the residuals of all pixels are examined together, this signal disappears as the opposite shifts from lower and higher radii compensate for each other. This leaves the residual distribution in Figure 29 consistent with being entirely caused by shot noise.

We conclude from this admittedly crude but nevertheless informative analysis that it (1) rules out significant clumpiness on scales comparable to the pixel size of each color bin; (2) demonstrates there are deviations on scales comparable to radial averaging size, indicating that the functional forms of the model do not perfectly capture the large-scale distribution; and (3) shows that these deviations are negligible for the disk and pronounced for the halo, pointing toward a need for halo profiles more complicated than a single power law.

4.3.9. Wide Survey Area and Model Fit Degeneracies

In a model with as many as 10 free parameters, it is not easy to assess the uniqueness of a best-fit solution nor to fully understand the interplay between the fitted parameters. We show two illuminating examples of fitting degeneracies.

In Figure 31 we plot the density distributions for two significantly different models: a thin plus thick disk model without a halo and a single disk plus halo model. Despite this fundamental intrinsic difference, it is possible to fine tune the model parameters to produce nearly identical Z -dependence of the density profiles at $R = 8$ kpc. As shown in the bottom panel, significant differences between these two models are only discernible at $|Z| > 3$ kpc and R significantly different from 8 kpc.

Second, in the left column of Figure 32 we reproduce the top two panels of Figure 15. The density profile is well described by two exponential disks of scale heights $H_1 = 260$ and $H_2 = 1000$ and normalization of 4%. In the right column of the figure we plot the same data, but overplot with best-fit models from Table 3. The scales in this model are $H_1 = 245$ and $H_2 = 750$, with thick-to-thin normalization of 13%, and the bottom right panel also includes a contribution of the halo. Although significantly different, the two models are here virtually indistinguishable.

This is a general problem of pencil beam surveys with a limited-sky coverage. A single pencil beam and even a few pencil beams (depending on the quality of the data and positioning of the beams) cannot break such model degeneracies. We speculate that this in fact is likely the origin of some of the dispersion in disk parameter

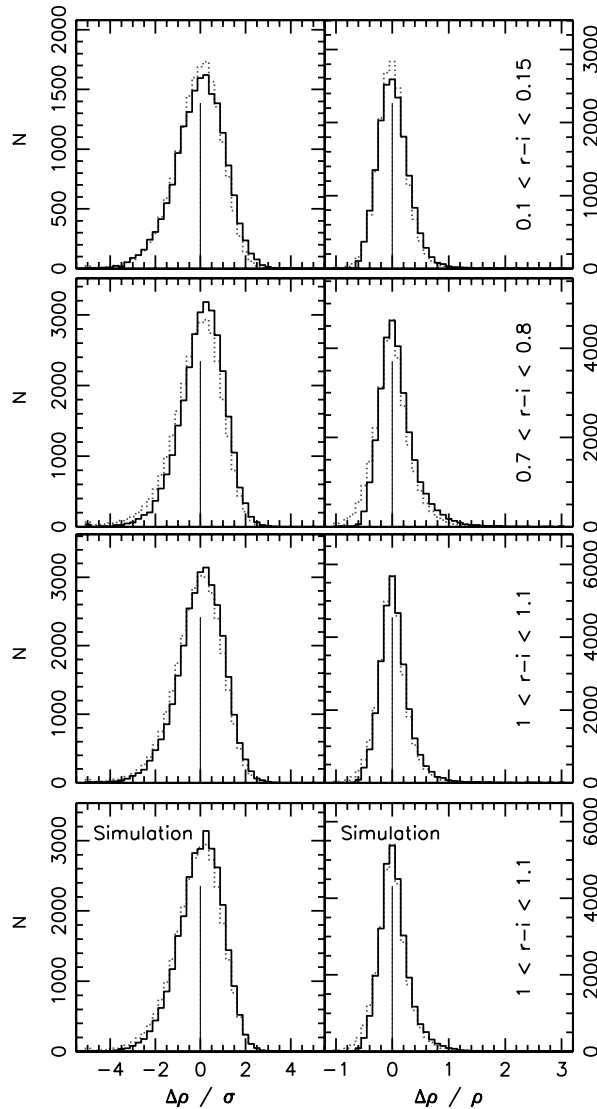


FIG. 29.—*Left column:* Poisson noise-normalized distribution of residuals in three-dimensional (X, Y, Z) pixels for three representative color bins. *Right column:* Model-normalized distribution of residuals in each pixel, $(\text{data} - \text{model})/\text{model}$. The black solid-line histograms show the data, while the red dotted-line histograms show the expectation from residuals due to Poisson noise only. The bottom row shows the same distributions derived from a Monte Carlo-simulated catalog, with 25% unresolved binary fraction, $\sigma_M = 0.3$ parallax dispersion, and SDSS photometric errors. [See the electronic edition of the *Journal* for a color version of this figure.]

values found in the literature (e.g., Siegel et al. 2002, Table 1; Bilir et al. 2006).

In our case, while we have not done a systematic search for degenerate models leading to similar χ^2 values given our survey area, we have explored the possibility by attempting 100 refits of the data starting with random initial parameter values. In the case of fits to individual bins, we find local χ^2 minima, higher by $\sim 20\%$ – 30% than the global minimum, with parameter values notably different from the best-fit solution. However, when jointly fitting all $r - i > 1.0$ color bins, in all cases the fit either fails to converge, converges to a local χ^2 minimum that is a factor of a few higher than the true minimum (and produces obviously spurious features in maps of residuals), or converges to the same best-fit values given in Table 3. SDSS therefore seems largely successful in breaking the degeneracies caused by the limited survey area

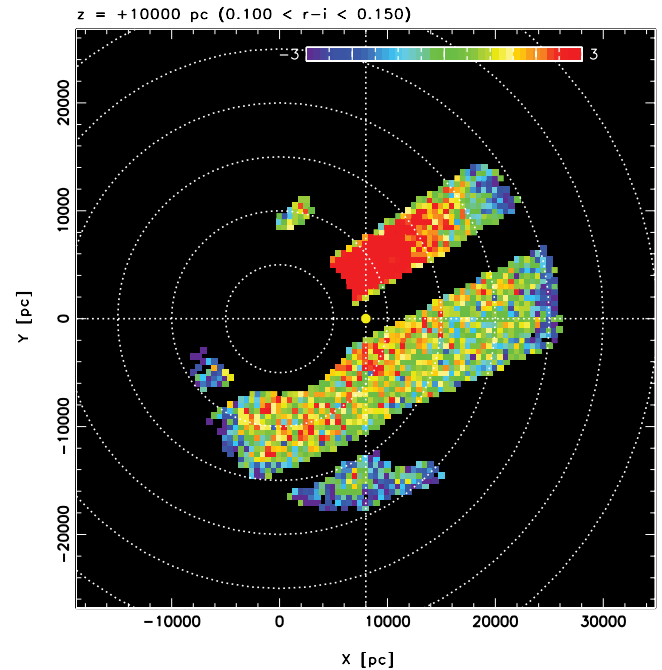


FIG. 30.—A $Z = 10$ kpc X - Y slice of data from the $0.10 < r - i < 0.15$ color bin. Only pixels with less than 5% of the density coming from the Galactic disk component are shown. The colors encode noise-normalized residuals in each pixel, saturating at -3σ (purple) and $+3\sigma$ (red). The large red spot in the top part of the figure is due to the Virgo overdensity (this region was excluded during model fitting; it is shown here for completeness only).

and photometric precision, leaving local departures from exponential profiles as the main remaining source of uncertainty in best-fit model parameters.

4.3.10. Physical Basis for the Density Profile Decomposition into Disks and the Halo

Although the density profiles shown in bottom right panel of Figure 32 and the bottom panel of Figure 15 appear with high signal-to-noise ratios, it may be somewhat troubling that as our range of observed distances expands, we need to keep introducing additional components to explain the data. Are these components truly physically distinct systems or largely phenomenological descriptions with little physical basis?

The question is impossible to answer from number density data alone, and two companions papers use metallicity estimates (Paper II) and kinematic information (Paper III) to address it. Here we only look at a subset of this question, namely, the differentiation between the disk and halo components. Disk stars (Population I and intermediate Population II) have metallicities on average higher by about 1–2 dex than that of the halo. Such a large difference in metallicity affects the $u - g$ color of turnoff stars (e.g., Chen et al. 2001). An analysis of SDSS colors for Kurucz model atmospheres suggests that stars at the tip of the stellar locus with $0.7 < u - g \lesssim 1$ necessarily have metallicities lower than about -1.0 . These stars also have markedly different kinematics, further supporting the claim that they are halo stars (Papers II and III).

We select two subsamples of stars from the $0.10 < r - i < 0.15$ color bin: low-metallicity halo stars with $0.60 < u - g < 0.95$ and high-metallicity disk stars with $0.95 < u - g < 1.15$. This separation is of course only approximate, and significant mixing is expected both at the faint end (disk stars contaminated by the more numerous halo stars) and at the bright end (halo stars

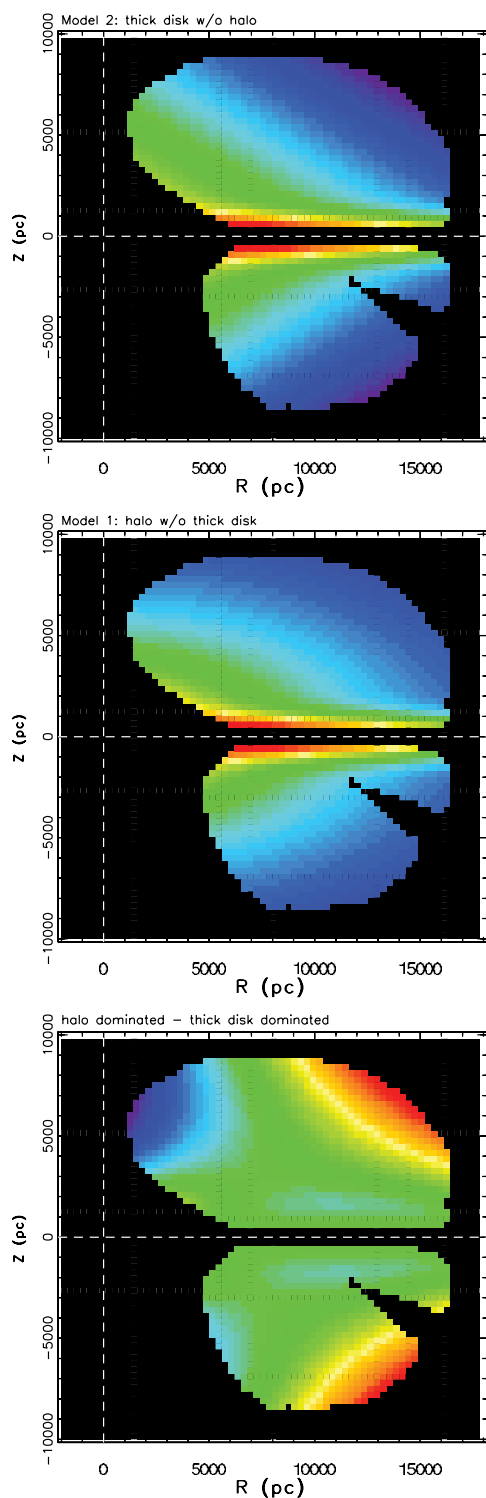


FIG. 31.—Illustration of the degeneracies in fitting models for stellar distribution. The top panel shows a thin disk plus thick disk model, without any contribution from the halo (volume density on a logarithmic stretch, from blue to red, shown only for the regions with SDSS data), and the middle panel shows a single disk plus an oblate halo model. Both models are fine-tuned to produce nearly identical counts for $R = 8$ kpc and $|Z| < 8$ kpc. The bottom panel shows the difference between the two models (logarithmic stretch for $\pm a$ factor of 3, from blue to red; the zero level corresponds to green color). The models are distinguishable only at $|Z| > 3$ kpc and R significantly different from 8 kpc.

contaminated by the more numerous disk stars). Nevertheless, the density profiles for these two subsamples, shown in Figure 33, are clearly different. In particular, the disk profile is much steeper and dominates for $Z \lesssim 3$ kpc, while the halo profile takes over at larger distances from the Galactic plane. This behavior suggests that the multiple components visible in the bottom panel in Figure 15 are not an overinterpretation of the data.

In addition to supporting a separate low-metallicity halo component, this test shows that a single exponential disk model is insufficient to explain the density profile of high-metallicity stars. This is ordinarily remedied by introducing the thick disk. However, with only the data presented here, we cannot deduce if the division into thin and thick disks has a physical basis or is a consequence of our insistence on exponential functions to describe the density profile.

4.3.11. The Corrected Best-Fit Parameters

In § 4.2 we have used two samples of stars to fit the parameters of the disk: the $1.0 < r - i < 1.4$ sample of M dwarfs and $0.65 < r - i < 1.0$ sample of late K/early M dwarfs. Best-fit results obtained from the two samples are very similar and consistent with the stars being distributed in two exponential disks with constant scales across the spectral types under consideration.

The fit to the $0.65 < r - i < 1.0$ sample required an addition of a third component, the Galactic halo. This, combined with the photometric parallax relations that are inappropriate for low-metallicity stars in this color range, may bias the determination of thick disk parameters. For example, while the measured scale height of the thick disk in the $0.65 < r - i < 1.0$ range is $\sim 10\%$ lower than in the $1.0 < r - i < 1.4$ range, it is difficult to say whether this is a real effect or an interplay of the disk and the halo.

Furthermore, we detected two localized overdensities in the thick disk region (§ 4.3.7). While every effort was made to remove them from the data before fitting the model, any residual overdensity that was not removed may still affect the fits. If this is the case, the $0.65 < r - i < 1.0$ bins are likely to be more affected than their redder counterparts, being that they cover a larger volume of space (including the regions where the overdensities were found). For these reasons, we prefer the values of disk parameters as determined from the $1.0 < r - i < 1.4$ sample, as these are (1) unaffected by the halo and (2) least affected by local overdensities.

Other dominant sources of errors are (in order of decreasing importance) (1) uncertainties in absolute calibration of the photometric parallax relation, (2) the misidentification of unresolved multiple systems as single stars, and (3) Malmquist bias introduced by the finite width of the $M_r(r - i)$ relation. Given the currently limited knowledge of the true photometric parallax relation (Fig. 2), there is little one can do but try to pick the best one consistent with the existing data and understand how its uncertainties limit the accuracy of derived parameters. Out of the two relations we use (bright, eq. [2], and faint, eq. [1]), we prefer the bright normalization as it is consistent with the kinematic data (Paper III) and the analysis done with wide binary candidates (§ 2.2.2) shows its shape to be correct to better than 0.1 mag for $r - i > 0.5$. If we are mistaken, as discussed in § 4.3.5, errors in M_r of $\Delta M_r = \pm 0.5$ will lead to errors of 20%–30% in parameter estimation. Given Figure 2 and the analysis of wide binary candidates in § 2.2.2 we believe this to be the worst-case scenario and estimate that the error of each scale parameter is unlikely to be larger than $\pm 20\%$.

The dependence of best-fit parameters derived from mock catalogs on multiplicity (binarity) is shown in Figure 34. The challenge in correcting for multiplicity is knowing the exact fraction

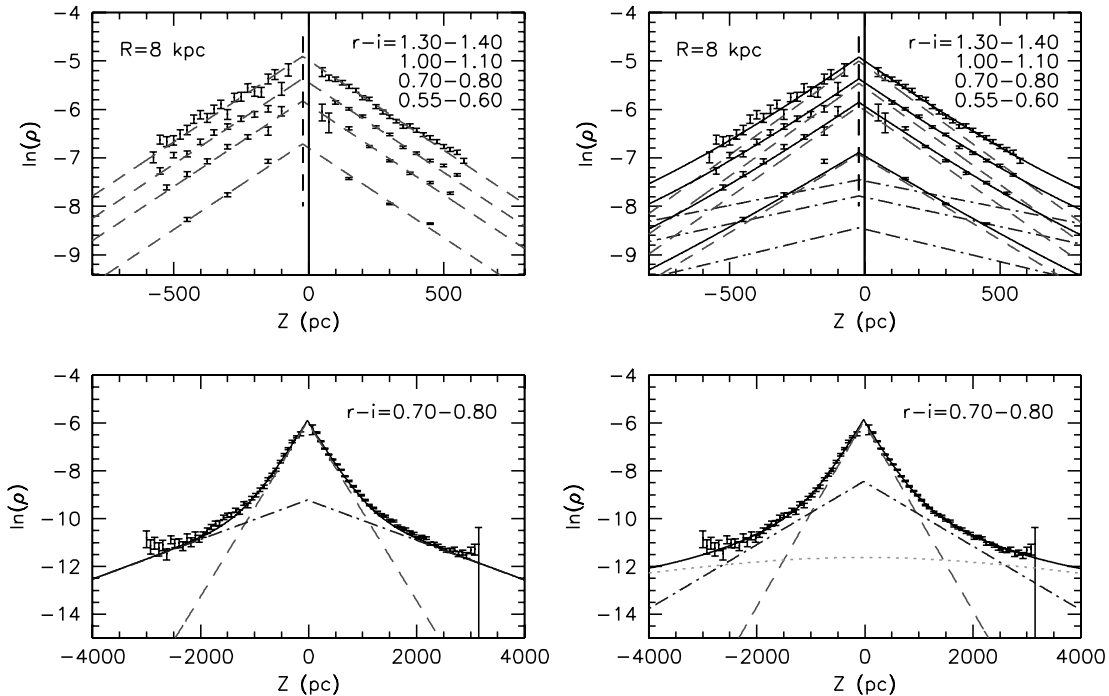


FIG. 32.—Illustration of degeneracies present in fitting of Galactic models. The two panels in the left column are the same top two panels of Fig. 15. The panels to the right show the same data, but are overplotted with best-fit models from Table 3. In spite of substantially different best-fit values, the two models are virtually indistinguishable when fitting the $R = 8$ kpc, $\pm Z$ -direction of the data. [See the electronic edition of the *Journal* for a color version of this figure.]

of observed “stars” which are unresolved multiple systems. While it is understood that a substantial fraction of Galactic field stars are in binary or multiple systems, its exact value, dependence on spectral type, population, and other factors are still poorly known. Measurements range from 20% for late types (L, M, and K dwarfs; Reid et al. 2006; Reid & Gizis 1997; Fischer & Marcy 1992) to upward of 60% for early types (G dwarfs; Duquennoy & Mayor 1991). The composition (mass ratios) of binaries is also poorly constrained, but appears to show a preference toward more equal-mass companions in late spectral types (Reid et al. 2006, Fig. 8). Given that our least biased disk parameters were derived from the M dwarf sample ($r - i > 1.0$), we choose to follow Reid & Gizis (1997) and adopt a binary fraction of 35%.

We accordingly revise L_1 , H_1 , and H_2 upward by 15% and L_2 by 10% to correct for multiplicity (see Fig. 34). We further include an additional 5% correction due to Malmquist bias (§ 4.3.3) and, for the same reason, correct the density normalization by -10% . The final values of measured and corrected parameters are listed in Table 10.

5. THE VIRGO OVERDENSITY

The X - Y projections of the number density maps at the heights above 6 kpc from the Galactic plane show a strong deviation from expected cylindrical symmetry. In this section we explore this remarkable feature in more detail. We refer to this feature as “the Virgo overdensity,” because the highest detected overdensity is in the direction of the constellation Virgo, but note that the feature is detectable over 1000 deg^2 of sky.

5.1. The Extent and Profile of the Virgo Overdensity

To quantify the extent and profile of the Virgo overdensity, we consider the data in an X' - Z plane, perpendicular to the Galactic symmetry axis, and rotated from the X - Z plane by $\phi = 30^\circ$ clockwise around the \hat{Z} -axis. In Figure 12, this plane would be seen edge on, as a straight line at a 30° angle from the X -axis, passing

through the Galactic center and the approximate center of the Virgo overdensity. Note that in this plane the distance measured along the X' -axis is just the cylindrical galactocentric radius R .

In the top left panel of Figure 35 we show the corresponding number density map for the bluest color bin. Isodensity contours show a significant deviation from the expected monotonic decrease with X' ($=R$). Instead, they reveal the existence of an overdense region around $X' \sim 7\text{--}8$ kpc and $Z \sim 10$ kpc. This overdensity is also visible in the density profiles at $Z = 10$ kpc above the plane, shown in the $Y' > -3$ kpc panels of Figure 36. As is discernible from these figures, the Virgo overdensity is responsible for at least a factor of 2 number density excess at $Z = 10$ kpc.

To analyze this feature in more detail, we subtract a best-fit Galactic model from the data shown in the top right panel of Figure 35. We first fit a model described by equations (21)–(24) to the observations having $Y < 0$ (or equivalently $180^\circ < l < 360^\circ$). As evidenced by Figure 12, this region does not seem significantly affected by the overdensity. We show the difference of the data from the top right panel of Figure 35 and the so obtained model in the top middle panel of the same figure. The top right panel shows the same difference but normalized to the model.

The model-normalized map reveals much more clearly the extent and location of the overdensity. A significant density excess (up to a factor of 2) exists over the entire sampled range of Z ($6 < Z/\text{kpc} < 20$). The importance of the overdensity, relative to the smooth Milky Way halo background, increases as we move away from the Galactic plane. This increase is however mainly due to a fast power-law decrease of the number density of the halo, which causes the increase in Virgo-to-Milky Way ratio. The number density of stars belonging to the overdensity actually increases toward the Galactic plane, as seen in the top middle panel.

For comparison, analogous density and residual plots from a parallel plane at $Y' = -9$ kpc are shown in the bottom row of

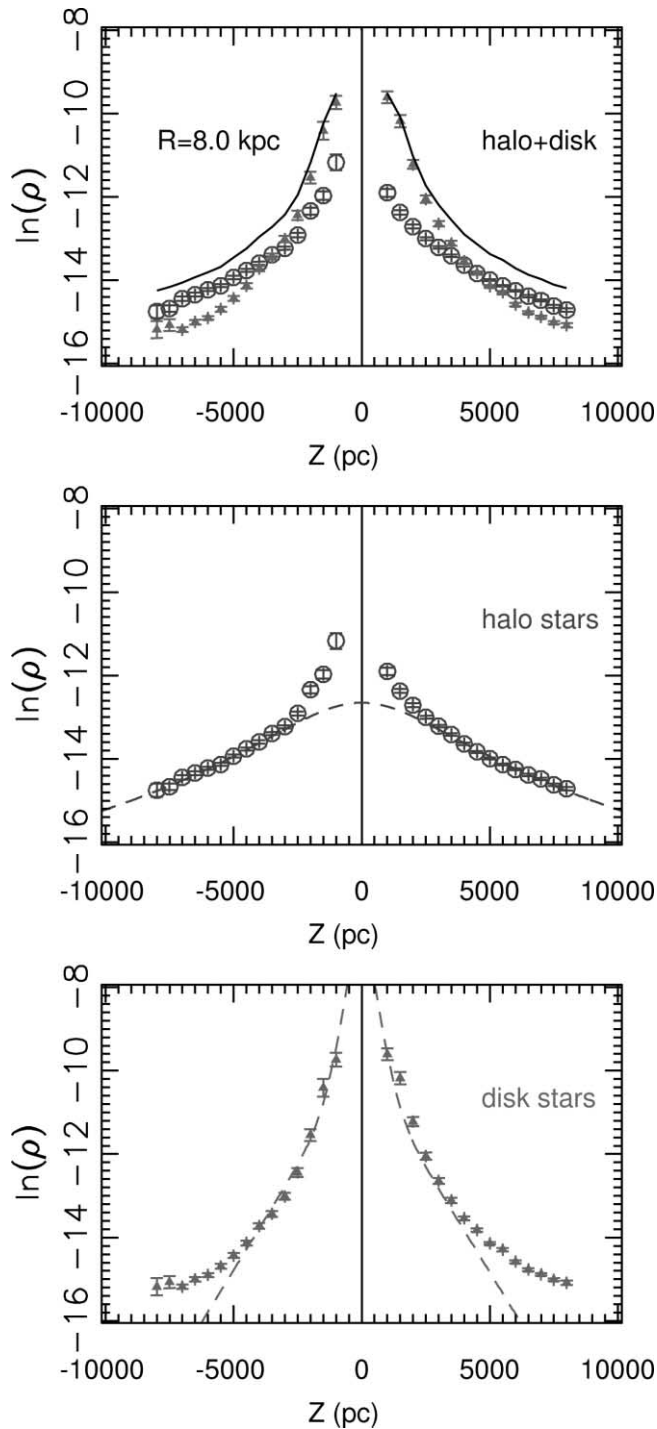


FIG. 33.—Vertical (Z) distribution of SDSS stellar counts for $R = 8$ kpc and $0.10 < r - i < 0.15$ color bin. Stars are separated by their $u - g$ color, which is a proxy for metallicity, into a sample representative of the halo stars (low metallicity, $0.60 < u - g < 0.95$, circles) and a sample representative of the disk stars (high metallicity, $0.95 < u - g < 1.15$, triangles). The line in the top panel shows the sum of the counts for both subsamples. The counts for each subsample are shown separately in the middle and bottom panels and compared to the best-fit models, shown as lines. Note that the disk stars are more concentrated toward the Galactic plane. Because of a simple $u - g$ cut, both samples are expected to suffer from contamination; close to the Galactic plane ($|Z| < 2$ kpc) the halo sample is contaminated by the disk stars, while further away from the plane ($|Z| > 5$ kpc), the disk sample is contaminated by halo stars. [See the electronic edition of the *Journal* for a color version of this figure.]

Figure 35. These show no large-scale deviations from the model. The density contours rise smoothly and peak near $X' = 0$, the point closest to the Galactic center. The same is seen in $Y' < -5$ kpc slices of Figure 36.

Because no local maximum of the overdensity is detected as Z approaches the observation boundary at $Z = 6$ kpc, with the data currently available we are unable to quantify its true vertical (Z) extent. It is possible that it extends all the way into the Galactic plane and, if it is a merging galaxy or a stream, perhaps even to the southern Galactic hemisphere. In the direction of Galactic radius, the Virgo overdensity is detected in the $2.5 < X'/\text{kpc} < 12.5$ region. The X' position³⁷ of maximum density appears to shift slightly from $X' \sim 6$ kpc at $Z = 6$ kpc to $X' \sim 7$ kpc at $Z = 15$ kpc. The width (“full width at half-density”) decreases by a factor of ~ 2 as Z increases from 6 to 20 kpc. While not a definitive proof, these properties are consistent with a merging galaxy or stream.

The thickness of the overdensity in the direction perpendicular to the plane of the image in Figure 35 (the Y' -direction) is no less than ~ 5 kpc. As in the case of the Z -direction, the true extent remains unknown because of the current data availability. Note that the size of the overdensity seen in the maps in the direction of the line of sight toward the Sun is a combination of the true size and the smearing induced by the photometric measurement and parallax errors (Fig. 7) and (most significantly) the effects of unrecognized stellar multiplicity. The true line-of-sight extent is therefore likely smaller, by at least 30%–35%.

5.2. Direct Verification of the Virgo Overdensity

Significant data processing was required to produce maps such as the one revealing the Virgo overdensity (e.g., the top panels in Fig. 35). In order to test its existence in a more direct and presumably more robust way, we examine the Hess diagrams constructed for the region of the sky that includes the maximum overdensity and for a control region that appears unaffected by the Virgo feature. The boundaries of these two regions, which are symmetric with respect to the $l = 0$ line, the corresponding Hess diagrams, and their difference are shown in Figure 37.

The top left panel of Figure 37 shows the northern (in Galactic coordinates) sky density of stars with $0.2 < g - r < 0.3$ and $20 < r < 21$ in the Lambert equal area projection of Galactic coordinates (the north Galactic pole is in the center, $l = 0$ is toward the left, and the outermost circle is $b = 0^\circ$). This map projection does not preserve shapes (it is not conformal, e.g., Gott et al. 2005), but it preserves areas—the area of each pixel in the map is proportional to the solid angle on the sky, which makes it particularly suitable for study and comparison of counts and densities on the celestial sphere. The color and magnitude constraints select stars in a $D \sim 18$ kpc heliocentric shell and can be easily reproduced using the publicly available SDSS database. The Virgo overdensity is clearly visible even with these most basic color and magnitude cuts and extends over a large patch of the sky, roughly in the $l = 300^\circ$, $b = 65^\circ$ direction. The overall number density distribution is clearly *not* symmetric with respect to the horizontal $l = 0, 180$ line. For example, in a thin shell at $r \sim 21$ mag there are 1.85 ± 0.03 times more stars in the $l = 300^\circ$, $b = 65^\circ$ direction, than in the corresponding symmetric ($l = 60^\circ$, $b = 65^\circ$) direction, a $\sim 28 \sigma$ deviation from a cylindrically symmetric density profile. When the color range is sufficiently red (e.g., $0.9 < g - r < 1.0$) and in the same magnitude range, the asymmetry disappears (not shown). These stars have

³⁷ Note that in this $Y' = 0$ plane $X' \equiv R$, the galactocentric cylindrical radius.

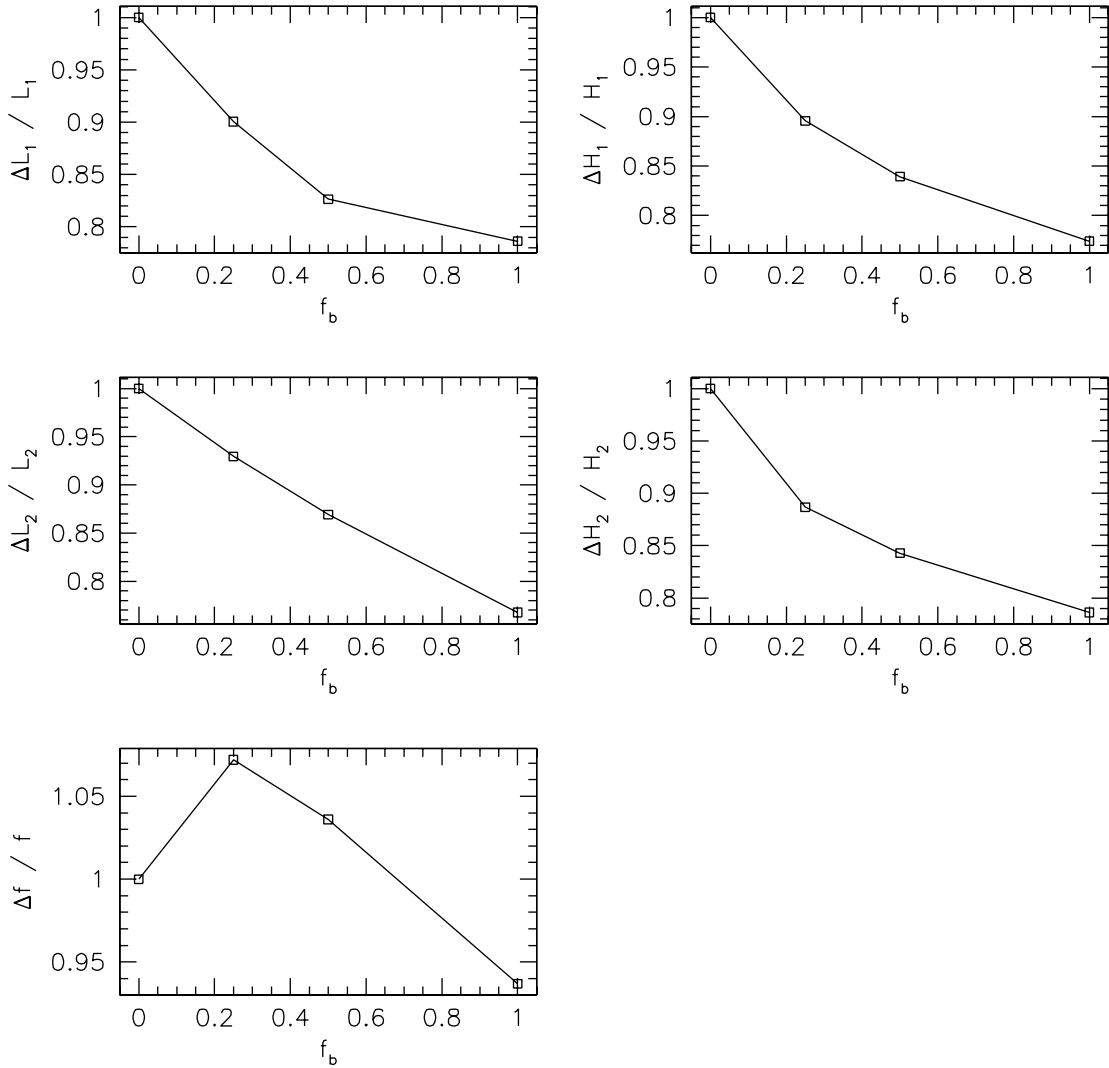


FIG. 34.—Effect of unrecognized binarity on fits of model parameters, derived from simulations listed in Table 8. Each of the panels shows the change of a particular model parameter when a fraction f_b of observed “stars” are unrecognized binary systems.

a smaller absolute magnitude, are therefore much closer, and do not go far enough to detect the overdensity.

The two right panels in Figure 37 show the Hess diagrams for two 540 deg² large regions toward ($l = 300^\circ, b = 60^\circ$) and ($l = 60^\circ, b = 60^\circ$), and the bottom left panel shows their difference.

TABLE 10
THE GALACTIC MODEL

Parameter	Measured	Bias-corrected Value	Error estimate
Z_0	25	...	20%
L_1	2150	2600	20%
H_1	245	300	20%
f	0.13	0.12	10%
L_2	3261	3600	20%
H_2	743	900	20%
f_h	0.0051	...	25%
q	0.64	...	≤ 0.1
n	2.77	...	≤ 0.2

NOTE.—Best-fit Galactic model parameters (see eqs. [21]–[24]), as directly measured from the apparent number density distribution maps (second column) and after correcting for a 35% assumed binary fraction and Malmquist bias due to photometric errors and dispersion around the mean of the photometric parallax relation (third column).

The difference map reveals a strong overdensity at $g - r \sim 0.3$ and $r \gtrsim 20$. A more quantitative analysis of the Hess diagram difference is shown in Figure 38. For red stars, the counts in two regions are indistinguishable, while for blue stars, the counts difference is highly statistically significant. There is no indication for a turnover in blue star number count difference, which strongly suggests that the Virgo overdensity extends beyond the SDSS faint limit. We conclude that the Hess diagram analysis robustly proves the existence of a significant star count overdensity toward $l = 300^\circ, b = 65^\circ$, from approximately $r \sim 18$ to ~ 21.5 mag.

From the diagram in the bottom left panel of Figure 37, a crude estimate of the surface brightness of the overdensity can be made by summing up the fluxes of all stars in the color-magnitude diagram and dividing the total flux by the area observed. To isolate the overdensity, we only count the fluxes of stars satisfying $0.2 < g - r < 0.8$ and $18 < r < 21.5$. This will effectively be a lower limit, because we will miss stars dimmer than the limiting magnitude ($r = 21.5$) and bright giants ($r < 18$). We obtain a value of

$$\Sigma_r = 32.5 \text{ mag arcsec}^{-2}. \quad (28)$$

This is about a magnitude and a half fainter than the surface brightness of the Sagittarius dwarf northern stream ($\Sigma_V \sim 31 \text{ mag arcsec}^{-2}$; Martínez-Delgado et al. 2001, 2004).

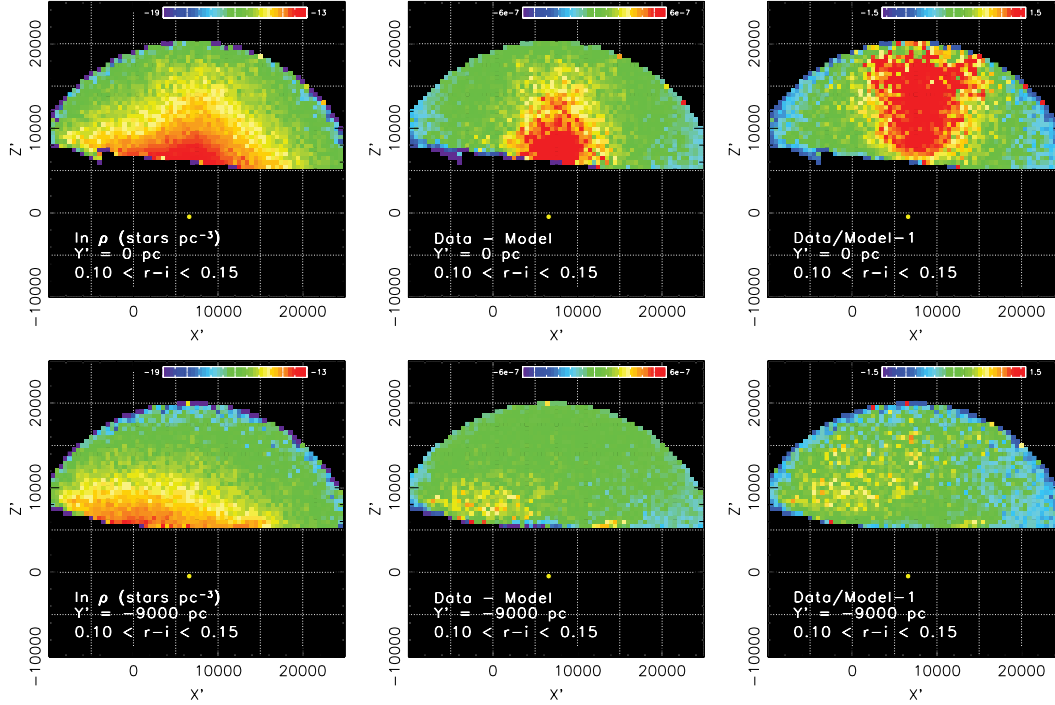


FIG. 35.—*Top left*: Distribution of stellar number density similar to that in Fig. 10, except that here we only show the data from a narrow $Y' = 0$ slice in a X', Y', Z' coordinate system defined by rotating the X, Y, Z galactocentric system counterclockwise by $\phi = 30^\circ$ around the Z -axis. In these coordinates, the $Y' = 0$ plane cuts vertically through the center of the Virgo overdensity. *Top middle*: Difference of the observed density and a best-fit model constrained using the data from the $Y < 0$ region. *Top right*: Same as the top middle panel, but *normalized to the model*. *Bottom*: Analogous slices taken at $Y' = -9$ kpc. Compared to the top row, they show a lack of any discernible substructure.

Assuming the entire overdensity covers $\sim 1000 \text{ deg}^2$ of the sky (consistent with what is seen in the top left panel of Fig. 37) and is centered at a distance of $D \sim 10$ kpc, from the surface brightness we obtain an estimate of the integrated absolute r -band magnitude, $M_r = -7.7$ mag. This corresponds to a total luminosity of $L_r = 0.09 \times 10^6 L_\odot$, where we calculate the absolute r -band magnitude of the Sun to be $M_{r\odot} = 4.6$, using equations (2) and (3) from Juric et al. (2002) and adopting $(B - V)_\odot = 0.65$ and $V_\odot = 4.83$ from Binney & Merrifield (1998). This luminosity estimate is likely uncertain by at least a factor of a few. Most of the uncertainty comes from the unknown exact distance and area covered by the overdensity. Uncertainty due to the flux limit depends on the exact shape of the luminosity function of stars making up the overdensity, but is likely less severe. For example, assuming that the luminosity function of the overdensity is similar to that of the solar neighborhood (Reid et al. 2002, Table 4) and that our sample of overdensity stars is incomplete for $g - r > 0.5$ (see bottom left panel of Fig. 37), the corrected luminosity and absolute magnitude are $L_r = 0.10 \times 10^6 L_\odot$ and $M_r = -7.8$ (note that only the red end of the luminosity function is relevant here). Taking a more conservative incompleteness bound of $g - r > 0.3$, the luminosity grows to $L_r = 0.11 \times 10^6 L_\odot$ (22% difference) or $M_r = -8$ in terms of absolute magnitude. Again, *these are all lower limits*.

5.3. Metallicity of the Virgo Overdensity

The SDSS u -band measurements can be used to gauge the metallicity of the Virgo overdensity. As already discussed in § 4.3.10, stars at the tip of the stellar locus ($0.7 < u - g \lesssim 1$) typically have metallicities lower than about -1.0 . This $u - g$ separation can be improved by using instead the principal axes in the $g - r$ versus $u - g$ color-color diagram (Ivezić et al. 2004b),

$$P_{1s} = 0.415(g - r) + 0.910(u - g) - 1.28, \quad (29)$$

$$P_{2s} = 0.545(g - r) - 0.249(u - g) + 0.234. \quad (30)$$

The MS stars can be isolated by requiring

$$-0.06 < P_{2s} < 0.06, \quad (31)$$

and the low-metallicity turnoff stars using

$$-0.6 < P_{1s} < -0.3, \quad (32)$$

with $P_{1s} = -0.3$ approximately corresponding to $[\text{Fe}/\text{H}] = -1.0$.

In Figure 39 we show Hess diagrams of P_{1s} color versus r magnitude for the Virgo overdensity field, the control field, and their difference. A significant excess of stars with $P_{1s} < -0.3$ exists in the Virgo overdensity field, while there is no statistically significant difference in star counts for stars having $P_{1s} > -0.3$. The observed P_{1s} distribution implies metallicities lower than those of thick disk stars and similar to those of the halo stars (see also Paper II).

5.4. Detections of Related Clumps and Overdensities

There are a number of stellar overdensities reported in the literature that are probably related to the Virgo overdensity. Newberg et al. (2002) searched for halo substructure in SDSS equatorial strips ($\delta \sim 0$) and reported a density peak at $(l, b) \sim (297^\circ, 63^\circ)$. They tentatively concluded that this feature is “a stream or other diffuse concentration of stars in the halo” and pointed out that follow-up radial velocity measurements are required to ascertain that the grouping is not a product of chance and statistics of small numbers.

Detections of RR Lyrae stars are particularly useful because they are excellent standard candles. Using RR Lyrae detected by the QUEST survey, Vivas et al. (2001; see also Zinn et al. 2004) discovered an overdensity at ~ 20 kpc from the Galactic center at $(l, b) \sim (314^\circ, 62^\circ)$ and named it the “12.4^h clump.” The same clump is discernible in the SDSS candidate RR Lyrae sample

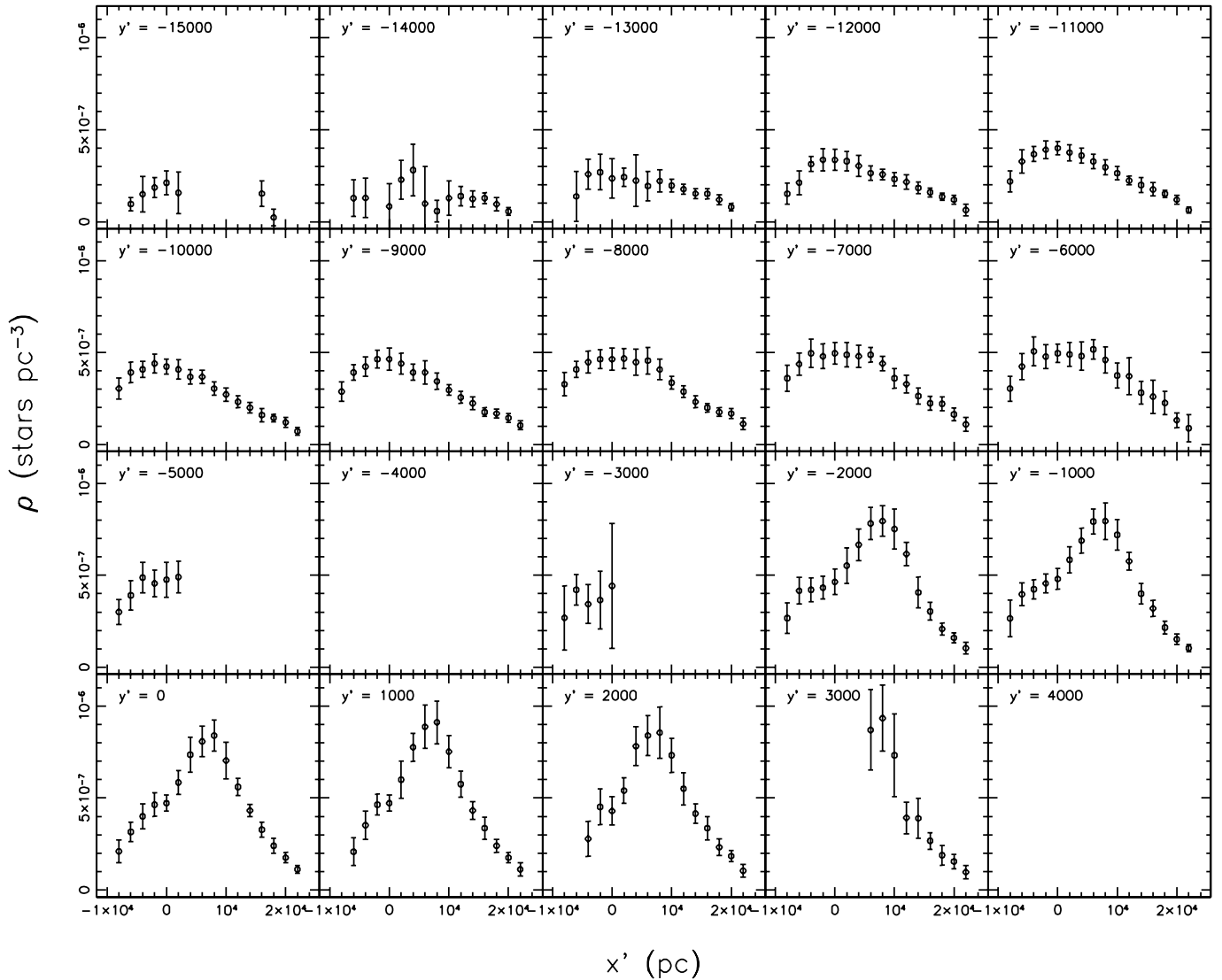


FIG. 36.—Distribution of stellar number density for $0.10 < r - i < 0.15$ color bin at $Z = 10$ kpc above the Galactic plane. Each panel shows a narrow Y' cross section in coordinate system defined by $\phi = 30^\circ$ (see the caption of Fig. 35). Note a clear and strong density excess around $X' \sim 8$ kpc in $Y' > 0$ panels, coming from the Virgo overdensity.

(Ivezić et al. 2000, 2003, 2004c, 2004d). More recently, the Northern Sky Variability Survey (NSVS) RR Lyrae survey (Woźniak et al. 2004) detected an overdensity in the same direction and at distances extending to the sample faint limit, corresponding to about ~ 6 kpc (P. Woźniak 2005, private communication).

The 2MASS survey offers an important advantage of an all-sky view of the Milky Way. We have followed a procedure developed by Majewski et al. (2003) to select M giant candidates from the public 2MASS database. We use M giant candidates that belong to the Sgr dwarf stream to fine-tune selection criteria. We also estimate the mean K -band absolute magnitude by tying it to the stream distance implied by RR Lyrae stars (Ivezić et al. 2004c, 2004d). We adopt $1.0 < J - K < 1.3$ and $9.2 < K < 10.2$ as the color-magnitude selection of M giant candidates at a mean distance of 10 kpc.

Using a sample of 75,735 candidates selected over the whole sky (dominated by stars in the Galactic plane), we study their spatial distribution in the high galactic latitude regions (see Fig. 40). We find a significant excess of candidate giants in the Virgo overdensity area, compared to a region symmetric with respect to the $l = 0$ line, with the number ratio consistent with the properties of the Virgo overdensity inferred from SDSS data. For example, in a

subsample restricted to $55^\circ < b < 80^\circ$, there are 66 stars with $240^\circ < l < 360^\circ$ and only 21 stars with $0^\circ < l < 120^\circ$, with the former clustered around $l \sim 300^\circ$. There is no analogous count asymmetry in the southern Galactic hemisphere.

5.5. A Merger, Tri-axial Halo, Polar Ring, or?

The Virgo overdensity is a major new feature in the Galactic halo; even within the limited-sky coverage of the available SDSS data, it extends over 1000 deg^2 of sky. Given the well-defined overdensity outline, low surface brightness, and luminosity, its most plausible interpretation is a tidally disrupted remnant of a merger event involving the Milky Way and a smaller, lower metallicity dwarf galaxy. However, there are other possibilities.

An attempt may be made to explain the detected asymmetry by postulating a nonaxisymmetric component such as a triaxial halo. This alternative is particularly interesting, because Newberg & Yanny (2005), who essentially used the same data as analyzed here, have suggested that evidence for such a halo exists in SDSS star counts. A different data analysis method employed here—the three-dimensional number density maps—suggests that the excess of stars associated with the Virgo overdensity is *not* due to a triaxial halo. The main argument against such a halo is that,

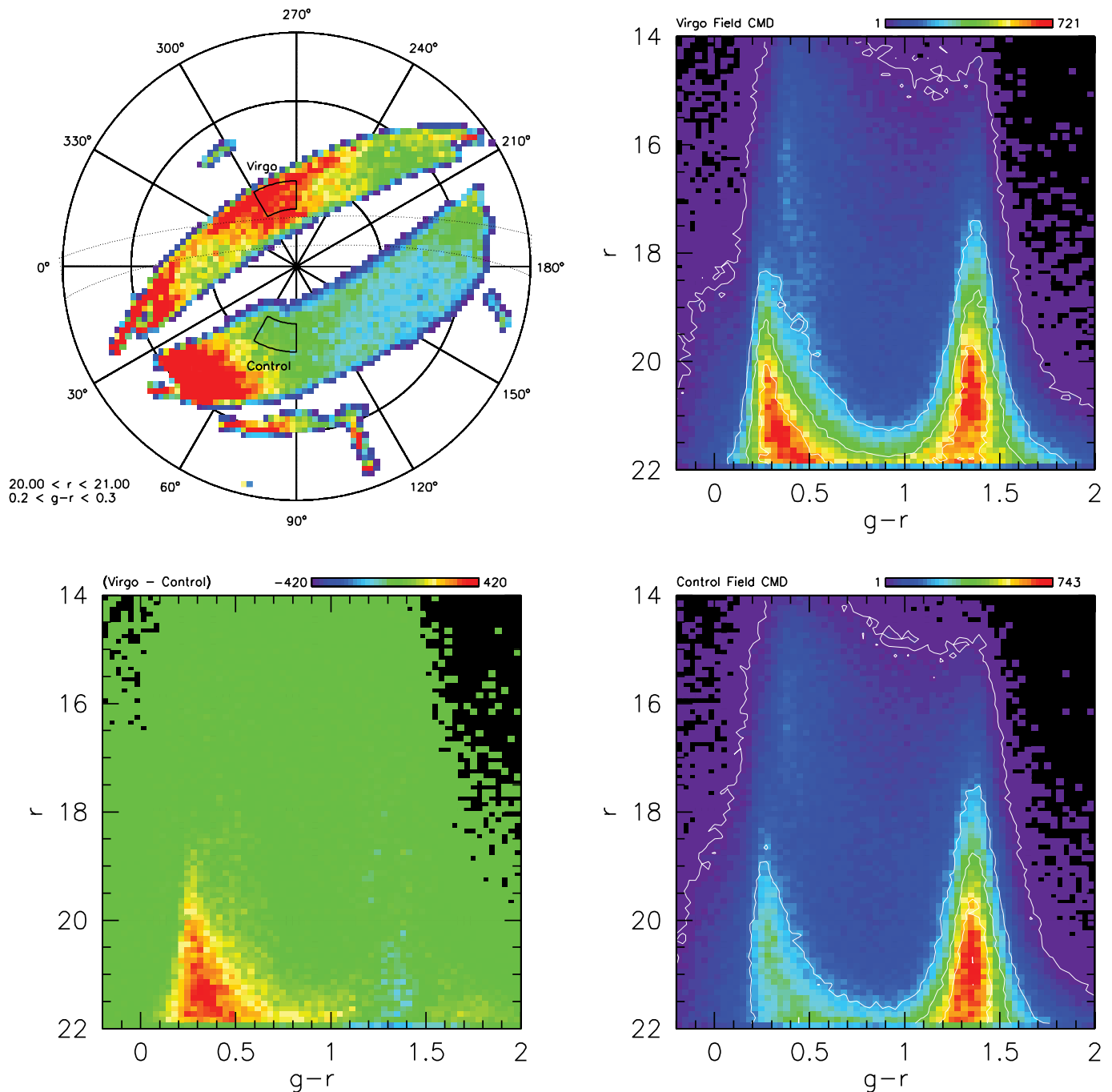


FIG. 37.—*Top left:* Sky density of stars with $b > 0^\circ$, $0.2 < g-r < 0.3$, and $20 < r < 21$ in the Lambert projection (concentric circles correspond to constant Galactic latitude; equal area corresponds to equal solid angle on the sky) of Galactic coordinates (the north Galactic pole is in the center, $l = 0$ is toward the left, and the outermost circle is $b = 0^\circ$). The number density is encoded with a rainbow color map and increases from blue to red. Note that the sky density distribution is *not* symmetric with respect to the horizontal $l = 0, 180$ line. When the stellar color range is sufficiently red (e.g., $0.9 < g-r < 1.0$), this asymmetry disappears (not shown). *Right column:* Hess diagrams for two 540 deg^2 large regions toward ($l = 300^\circ, b = 60^\circ$; *top*) and ($l = 60^\circ, b = 60^\circ$; *bottom*), marked as polygons in the top left panel. *Bottom left:* Difference between these Hess diagrams; note the strong statistically significant overdensity at $g-r \sim 0.3$ and $r \gtrsim 20$. The pixel size in each of the three Hess diagrams is $(d(g-r), dr) = (0.033, 0.1)$.

despite its triaxiality, it still predicts that the density decreases with the distance from the Galactic center. But, as shown in Figures 12 and 36, the observed density profile has a local maximum that is *not* aligned with the Galactic center. This can still be explained by requiring the axis of the halo not to be coincident with the Galactic axis of rotation. However, even this model requires the halo density to attain maximal value in the Galactic center, and as seen from Figure 35, a modest linear extrapolation of the Virgo overdensity to $Z = 0$ still keeps it at $R \sim 6$ kpc away

from the Galactic center. Unless one is willing to resort to models where the center of the stellar halo and the center of the Milky Way disk do not coincide, triaxial halo cannot explain the geometry of the Virgo overdensity.

Although this makes the explanation of Virgo as a signature of a triaxial halo unlikely, it does not preclude the existence of such a halo. Unfortunately, it would be very difficult to obtain a reliable measurement of the halo triaxiality with the currently available SDSS data because of contamination by the Virgo overdensity

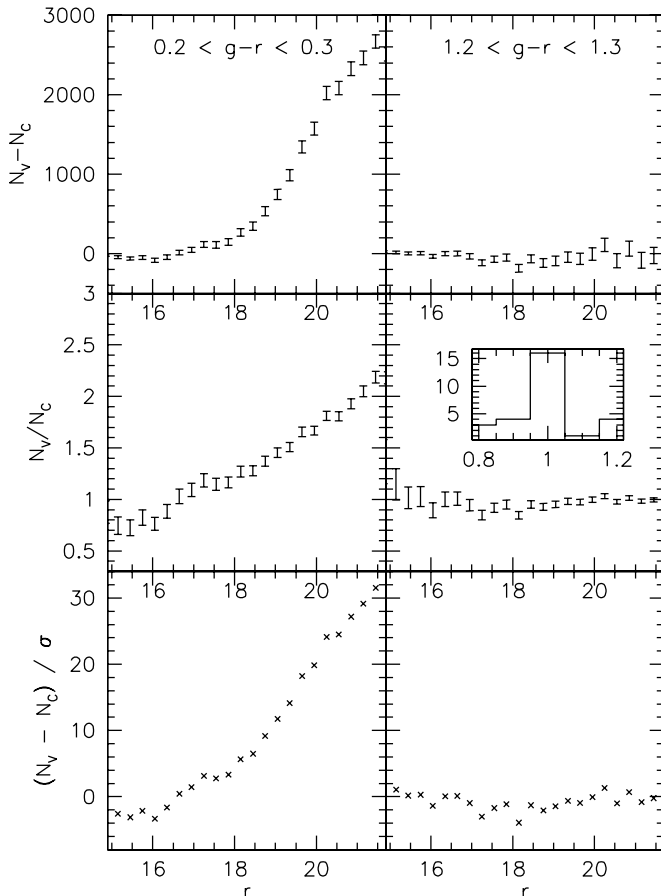


FIG. 38.—Quantitative analysis of the Hess diagram difference shown in the bottom left panel in Fig. 37. The left column corresponds to the color bin $0.2 < g - r < 0.3$ that is representative of the Virgo overdensity, and the right column is a control sample with stars satisfying $1.2 < g - r < 1.3$. The top panels show the counts difference as a function of apparent magnitude, and the middle panels show the counts ratio. The inset in the middle right panel shows a histogram of the counts ratio for $r < 21.5$. The bottom panels show the counts difference normalized by the expected Poisson fluctuations. Note that for red stars the counts are indistinguishable, while for blue stars the difference is highly statistically significant.

and uncertainties about its true extent. As more SDSS and other data become available in other parts of the sky, it may become possible to mask out the overdensity and attempt a detailed halo fit to reveal the exact details of its shape and structure.

Another possible explanation of the overdensity is a “polar ring” around the Galaxy. This possibility seems much less likely than the merger scenario, because there is no visible curvature toward the Galactic center at high Z in Figure 35. Indeed, there seems to be a curvature in the opposite sense, where the bottom ($Z \sim 6$ kpc) part of the overdense region appears to be about 0.5–1 kpc closer to the Galactic center than its high- Z part. In addition, there is no excess of 2MASS M giant candidates in the southern sky that could be easily associated with the northern Virgo overdensity.³⁸

Finally, the coincidence of this overdensity and the Virgo galaxy supercluster (Binggeli 1999) could raise a question of whether the overdensity could be due to faint galaxies that are misclassified as stars. While plausible in principle, this is most likely not the case because the star/galaxy classifier is known to be robust at the 5% level to at least $r = 21.5$ (Ivezić et al. 2002), the overdensity is detected over a much larger sky area (1000 deg^2 vs. $\sim 90 \text{ deg}^2$), and the overdensity is confirmed by apparently much brighter RR Lyrae stars and M giants.

6. DISCUSSION

6.1. A Paradigm Shift

Photometric parallax methods have a long history of use in studies of the Milky Way structure (e.g., Gilmore & Reid 1983; Kuijken & Gilmore 1989; Chen et al. 2001; Siegel et al. 2002). An excellent recent example of the application of this method to pre-SDSS data is the study by Siegel et al. (2002). While their and SDSS data are of similar photometric quality, the sky area analyzed here is over 400 times larger than that analyzed by Siegel et al. This large increase in sample size enables a shift in emphasis from modeling to direct model-free *mapping* of the complex and clumpy Galactic density distribution. Such mapping and analysis

³⁸ Note that the polar rings explanation is also unlikely for theoretical reasons as these are thought to originate in large galactic collisions which would leave its imprint on other components of the Milky Way as well. We discuss it as an option here from a purely observational standpoint and mainly for completeness.

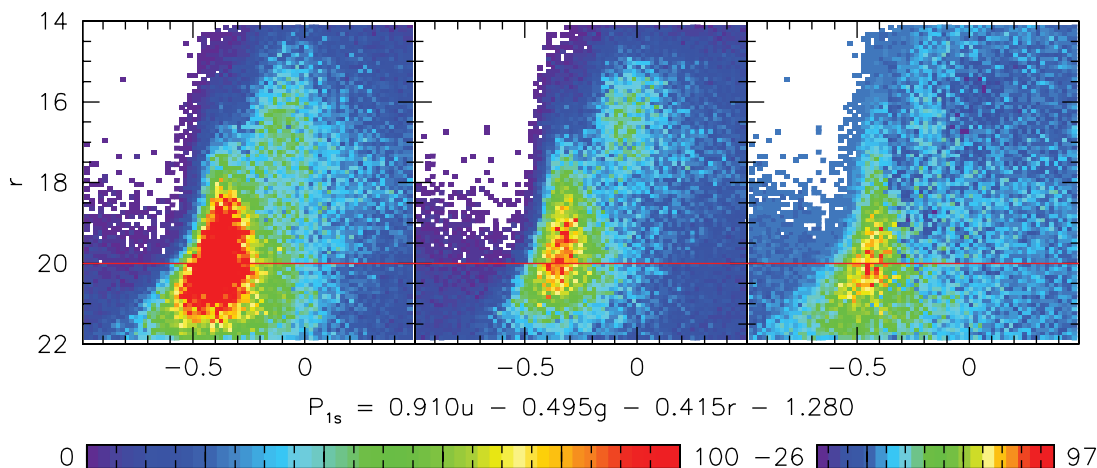


FIG. 39.—Hess diagrams of P_{1s} color vs. r magnitude for the Virgo overdensity field (left), the control field as defined in Fig. 37 (middle), and their difference (right). The colors encode star counts within the fields. A significant excess of stars with $P_{1s} < -0.2$ is present in the Virgo overdensity field. There is no statistically significant difference in star counts for stars having $P_{1s} > -0.2$, implying that the stars that constitute the Virgo overdensity have metallicities lower than disk stars and closer to metallicities characteristic of the halo.

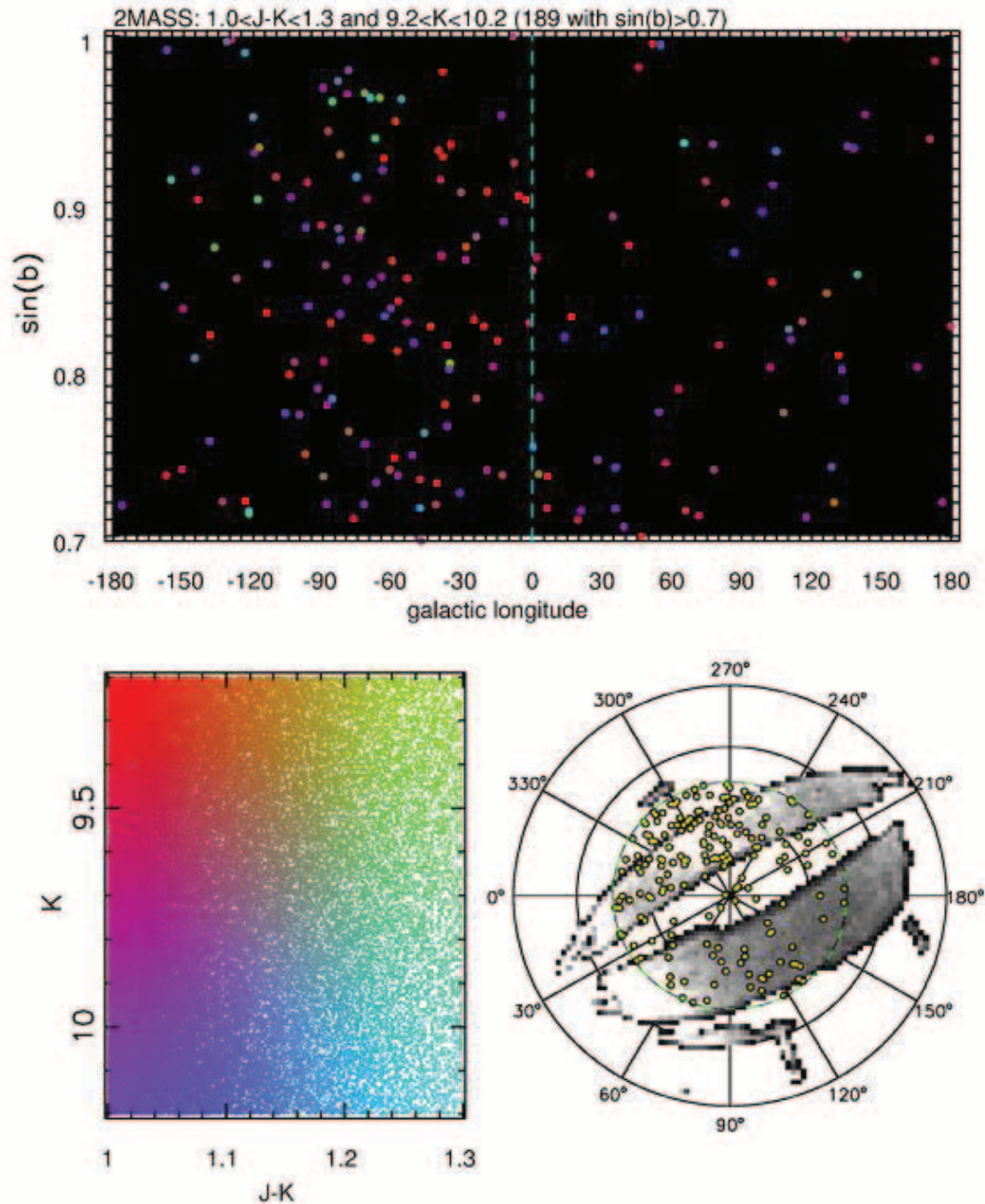


FIG. 40.—Sky distribution of 189 2MASS M giant candidates with $b > 45^\circ$, selected by $9.2 < K < 10.2$ and $1.0 < J - K < 1.3$. The symbols in the top panel are color coded using their K -band magnitude and $J - K$ color, according to the scheme shown in the bottom panel (which shows all 75,735 candidates from the whole sky). The symbols in bottom right panel show the same sample as in the top panel in Lambert projection, with the SDSS density map from Fig. 37 shown as the gray-scale background. At $\sin(b) > 0.8$, there are 2.5 times as many stars with $l < 0$ than with $l > 0$. This asymmetry provides an independent confirmation of the Virgo overdensity revealed by the SDSS data.

of the maps allows for identification and removal of clumpy substructure, which is a *necessary precondition* for a reliable determination of the functional form and best-fit parameters of the Galactic model.

This qualitative paradigm shift was made possible by the availability of SDSS data. SDSS is superior to previous optical sky surveys because of its high catalog completeness and precise multiband CCD photometry to faint flux limits over a large sky area. In particular, the results presented here were enabled by several distinctive SDSS characteristics:

1. A large majority of stars detected by the SDSS are MS stars, which have a fairly well-defined color-luminosity relation. Thus, accurate SDSS colors can be used to estimate luminosity and,

hence, distance for each individual star. Accurate photometry (~ 0.02 mag) allows us to reach the intrinsic accuracy of the photometric parallax relation, estimate distances to single stars within 15%–20%, and estimate the relative distances of stars in clumps of similar age and metallicity to better than 5%.

2. Thanks to faint flux limits ($r \sim 22$), distances as large as 15–20 kpc are probed using numerous MS stars (~ 48 million). At the same time, the large photometric dynamic range and the strong dependence of stellar luminosities on color allow constraints ranging from the Sun's offset from the Galactic plane (~ 25 pc) to a detection of overdensities at distances beyond 10 kpc.

3. The large-sky area observed by the SDSS (as opposed to pencil beam surveys), spanning a range of Galactic longitudes and latitudes, enables a good coverage not only of the (R, Z) -plane,

but also of a large fraction of the Galaxy’s volume. The full three-dimensional analysis, such as slices of the maps in X - Y planes, reveals a great level of detail.

4. The SDSS u -band photometric observations can be used to identify stars with subsolar metallicities and to study the differences between their distribution and that of more metal-rich stars.

6.2. The Best-Fit Galactic Model

When the exponential disk models are used to describe the gross behavior of the stellar number density distribution, we derive the best-fit parameter values summarized in Table 10. Before proceeding to compare these results to the literature, we note that a proper comparison with previous work is sometimes difficult due to the lack of clarity of some authors regarding which effects were (or were not) taken into account when deriving the model parameters. Of particular concern is the problem of unrecognized multiplicity: uncorrected for, or if using a significantly different binary fraction, it will affect the disk scales by up to 30% (§ 4.3.4). In the discussion to follow we assumed, if not explicitly mentioned otherwise, that all appropriate corrections were taken into account by the authors of the studies against which we compare our results.

The derived 300 pc vertical scale of the thin disk (corrected for an assumed 35% binary fraction) is about 10% lower than the canonical 325 pc value and near the middle of the range of values found in the recent literature (240–350 pc; Robin et al. 1996; Larsen & Humphreys 1996; Buser et al. 1999; Chen et al. 2001; Siegel et al. 2002). Similarly, the scale height of the thick disk is in the range found by Siegel et al. (2002), Buser et al. (1999), and Larsen & Humphreys (1996) and about 20% higher than the 580–790 pc range spanned by measurements of Robin et al. (1996), Ojha et al. (1999), and Chen et al. (2001). We note that uncorrected for unrecognized multiplicity, our thin and the thick disk scale estimates (245 and 740, respectively) would be closer to the lower end of the range found in the literature.

We find a local thick disk normalization of $\sim 12\%$, larger than most previous estimates but similar to recent determinations by Chen et al. (2001) and Siegel et al. (2002) ($\gtrsim 10\%$). Models with normalizations lower than 10% show increasingly large χ^2 , and in particular, the combinations of parameters characteristic of early “low-normalization/high-thick disk scale height” models (e.g., Gilmore & Reid 1983; Robin & Creze 1986; Yoshii et al. 1987; Yamagata & Yoshii 1992; Reid & Majewski 1993) are strongly disfavored by the SDSS data. The root cause of the apparent discrepancy may be sought for in the fact that all of these studies were pencil beam surveys operating on a single or at most a few lines of sight, usually toward the NGP. However, a single or even a few pencil beams are insufficient to break the degeneracies inherent in the multiparameter Galactic model (§ 4.3.9). While adequately describing the observed lines of sight, these pencil beam best-fit parameters are local minima, unrepresentative of the entire Galaxy. Only by using a wider and deeper sample, such as the one presented here, were we able to break the degeneracy and derive a globally representative model.

The value of the thin disk scale length is in agreement with the recent estimates by Ojha et al. (1999), Chen et al. (2001), and Siegel et al. (2002) and lower than the traditionally assumed 3–4 kpc. The scale length of the thick disk is longer than that of the thin disk. The qualitative nature of this result is robust; variations of the assumed photometric parallax relation, binary fraction, or the exact choice of and size of the color bins leave it unchanged. Quantitatively, the ratio of best-fit length scales is

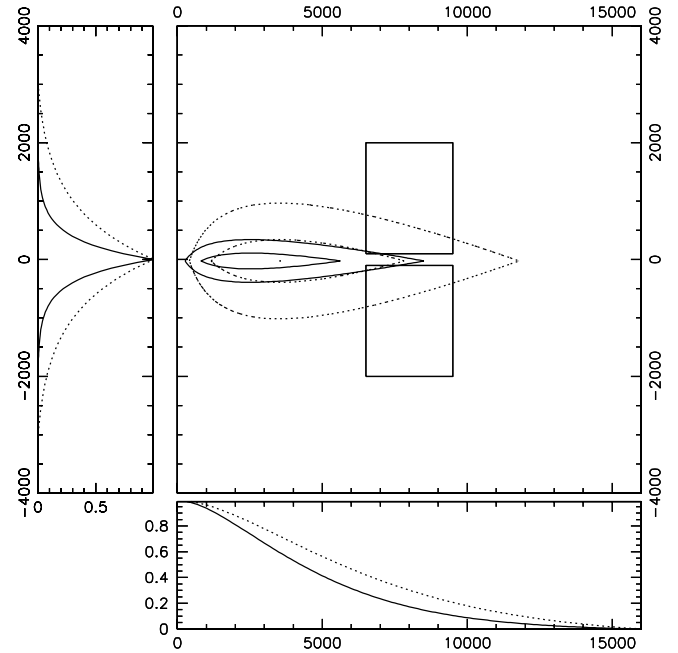


FIG. 41.—Mass contribution to thin (solid lines) and thick (dotted lines) disks from different radii and heights in the Galaxy. Center panel shows the isodensity contours of thin (solid lines) and thick (dotted lines) disks having the bias-corrected parameters of Table 10. Two rectangles centered around $R = 8$ kpc enclose the range in radii and vertical distances Z from the disk from which the model parameters were measured. The bottom panel shows the cumulative fraction of disk mass enclosed outside a given radius R . Similarly, the left panel shows the fraction of disk mass enclosed at heights $|Z| > |Z_{\text{given}}|$. Note that while our coverage in the Z -direction is adequate, in the R -direction we sample a region that contains less than 20% of the total disk mass and extrapolate the obtained density laws toward the Galactic center where most of the mass lies.

close to 1.4, similar (within uncertainties) to typical scale length ratios of ~ 1.25 seen in edge-on late-type disk galaxies (Yoachim & Dalcanton 2006).

Assuming that exponential density laws correctly describe the density distribution all the way to the Galactic center, our model implies that $\sim 23\%$ of the total luminosity (and stellar mass) in K and M dwarfs is contained in the thick disk. Despite being an extrapolation from a small region containing only a few tens of percent of the total mass of the disk (Fig. 41), this is in good agreement with observations of thick disks in external edge-on galaxies (Yoachim & Dalcanton 2006, Fig. 24).

6.3. Detection of Resolved Substructure in the Disk

Although important for understanding the current structure of the Milky Way, the disk mass ratios, details of density laws, or the exact values of Galactic model parameters are *insufficient by themselves* to attack the question of the mechanism of Galactic disk formation (both thin and thick). It is the departures from these laws that actually hold more information about the formation than the laws themselves.

Thick disk formation scenarios can broadly be divided into three classes: (1) slow kinematic heating of stars from the thin disk (Spitzer & Schwarzschild 1953; Barbanis & Woltjer 1967; Sellwood & Carlberg 1984), (2) pressure-supported slow collapse immediately after an ELS62-like monolithic collapse (e.g., Larson 1976), or (3) merger-induced stirring of thin disk material and/or direct accretion of stellar content of the progenitor (Quinn et al. 1993; Abadi et al. 2003; Brook et al. 2004). Scenarios (1) and (2) are usually disfavored due to the inability of either the giant

molecular clouds or the spiral structure to excite the stars to orbits observed in the thin disk (e.g., Quillen & Garnett 2000) and the apparent lack of vertical metallicity gradient in the thick disk (Gilmore et al. 1995; see however Paper II for evidence to the contrary).

The third scenario recently garnered increased attention, with detailed theoretical simulations of the formation of realistic galaxies in a Λ CDM hierarchical merger picture context (Abadi et al. 2003; Brook et al. 2004), the observation of properties of thick disks (Dalcanton & Bernstein 2002; Yoachim & Dalcanton 2006), and even a counterrotating thick disk in FGC 227 (Yoachim & Dalcanton 2005). A simulation reported by Abadi et al. (2003) while not *directly* comparable to the Milky Way (their galaxy is spheroid dominated) is especially illuminating regarding the qualitative mechanisms that may build up the thick disk. Three of their conclusions are of particular consequence to our work: (1) the thick disk is formed by direct accretion of stellar content from satellites on low-inclination orbits; (2) the stars from a single disrupted satellite are not uniformly radially mixed, but rather form a toruslike structure at radii where the final disruption occurs; and (3) if formed through the same process, the disk of the Milky Way disk may still hold signatures of such early accretion events.

Our finding that the thin and thick disk structure, similarly to that of the halo, is complicated by localized overdensities and permeated by ringlike departures from exponential profiles may lend credence to the mechanism described by Abadi et al. (2003). In addition to the already known Monoceros stream, we found evidence for two more overdensities in the thick disk region (Fig. 27), both consistent with rings or streams in the density maps. While unlikely to be the relics from the age of thick disk formation (they would need to survive for ~ 8 –10 Gyr), it is plausible that they, like the Monoceros stream, are remnants of smaller and more recent accretion events analogous to those that formed the thick disk.

In the case of the Monoceros stream, the three-dimensional maps offer an effective method to study its properties. The maps demonstrate this feature is well localized in the radial direction, which rules out the hypothesis that this overdensity is due to disk flaring. The maps also show that the Monoceros stream is not a homogeneously dense ring that surrounds the Galaxy, providing support for the claim by Rocha-Pinto et al. (2003) that this structure is a merging dwarf galaxy (see also Peñarrubia et al. [2005] for a comprehensive theoretical model). In Paper II we demonstrate that stars in the Monoceros stream have a metallicity distribution that is more metal-poor than thick disk stars, but more metal-rich than halo stars.

Discoveries of this type of substructure point to a picture of the thick disk filled with streams and remnants much in the same way like the halo. A crude extrapolation of the three disk overdensities seen in our survey volume ($|Z| < 3$ kpc, $R < 15$ kpc) to the full Galactic disk leads to a conclusion that there may be up to ~ 15 –30 clumpy substructures of this type in the Galaxy. These “disk streams” are still likely to carry, both in their physical (metallicity) and kinematic properties, some information on their progenitors and history.

6.4. Stellar Halo

We find it possible to describe the halo of the Milky Way by an oblate r^{-n_H} power-law ellipsoid, with the axis ratio $c/a \equiv q_H \sim 0.5$ –0.8 and the power-law index of $n_H = 2.5$ –3 (with the formal best-fit parameters $q_H = 0.64$ and $n_H = 2.8$ for galactocentric radii $\lesssim 20$ kpc). These values are consistent with previous studies; specifically, they are in excellent agreement with Besançon

program values ($q_H = 0.6$ –0.85, $n_H = 2.44$ –2.75; Robin et al. 2000), with a more recent measurement of $q_H = 0.6$ and $n_H = 2.75$ by Siegel et al. (2002) and with the previous SDSS estimate of $q_H \sim 0.55$ (Chen et al. 2001). The convergence of best-fit values is encouraging, especially considering the differences in methodologies (direct fitting vs. population synthesis modeling) and the data (photometric systems, limiting magnitudes, types of tracers, and lines of sight) used in each of these studies.

The goodness of halo model fit is poorer than that of the disk fits (reduced $\chi^2 \sim 2$ –3). Similar problems with halo fits were previously noticed in studies of smaller samples of kinematically and metallicity-selected field stars (Hartwick 1987; Sommer-Larsen & Zhen 1990; Allen et al. 1991; Preston et al. 1991; Kinman et al. 1994; Carney et al. 1996; Chiba & Beers 2000), globular clusters (Zinn 1993; Dinescu et al. 1999), and MS stars (Gilmore et al. 1985; Siegel et al. 2002) and are unlikely to be explained away by instrumental or methodological reasons alone (Siegel et al. 2002). Our own analysis of why this is so (§ 4.3.8 and Fig. 30) points toward a need for a more complex density distribution profile. For example, instead of a single power law, a two-component “dual halo,” in which the stars are divided into a spherical and a flattened subcomponent, may be invoked to explain the observations (e.g., Sommer-Larsen & Zhen 1990).

Such models, when applied to star counts, do show improvements over a single power law (Siegel et al. 2002). Furthermore, this division may be theoretically motivated by an attempt to unify the ELS62 and Searle & Zinn (1978) pictures of Galaxy formation: the flattened subcomponent being a result of the initial monolithic collapse and the spherical component originating from subsequent accretion of satellites (Sandage 1990; Majewski 1993; Norris 1994). While this explanation is *circumstantially* supported by the detection of ongoing accretion in the halo today (e.g., Yanny et al. 2000; Ivezić et al. 2000; Vivas et al. 2001; Majewski et al. 2003; Belokurov et al. 2006 and references therein), we would prefer a more *direct* line of evidence for it, derived from observations of halo stars themselves.

For example, one may hope the component coming from accretion is visibly irregular, streamlike, and/or clumpy, thus lending credence to the hypothesis of its origin. However, our examination of the distribution of residuals in § 4.3.8 revealed no signal of unresolved clumpy substructure in the halo on ~ 1 –2 kpc scales. Instead, we found the large reduced χ^2 is best explained by a poor choice of the density law profile (a single power law). A double power-law or a more complicated profile such as the one used by Preston et al. (1991) would likely better fit the data.

The clumpiness may still be prevalent, but on a different spatial scale or smaller in amplitude and harder to detect with the simple analysis employed here. We leave the question of scale-dependent clumpiness in the halo and its possible two-component nature for a subsequent study.

6.5. The Virgo Overdensity

We report the discovery of the Virgo overdensity. Despite its large angular size and proximity, its low surface brightness kept it from being recognized by smaller surveys. Given the low surface brightness, its well-defined outline, and low metallicity, the most plausible explanation of the Virgo overdensity is that it is a result of a merger event involving the Milky Way and a smaller, lower metallicity dwarf galaxy. For now, based on existing maps, we are unable to differentiate whether the observed overdensity is a tidal stream, a merger remnant, or both. However, it is evident that the Virgo overdensity is surprisingly large, extending

in the vertical (Z) direction to the boundaries of our survey ($6 \text{ kpc} < Z < 15 \text{ kpc}$) and $\sim 10 \text{ kpc}$ in the R -direction. It is also exceedingly faint, with a lower limit on the surface brightness of $\Sigma_r = 32.5 \text{ mag arcsec}^{-2}$.

A potential connection of the Virgo overdensity and the Sagittarius stream is discussed in a follow-up paper by Martínez-Delgado et al. (2007). Their N -body simulations of the Sagittarius stream show that the Virgo overdensity resides in the region of space where the leading arm of the Sagittarius stream is predicted to cross the Milky Way plane in the solar neighborhood. This tentative Virgo-Sagittarius association needs to be confirmed by measurement of highly negative radial velocities for the stars of the Virgo overdensity.

A similar diffuse structure, the Triangulum-Andromeda feature (hereafter, TriAnd), was recently identified by Rocha-Pinto et al. (2004) and Majewski et al. (2004) in the southern Galactic hemisphere as an overdensity of M giants observed with 2MASS. They find an excess in M giant number density over a large area of the sky ($100^\circ < l < 150^\circ$, $-40^\circ < b < -20^\circ$). TriAnd, just as the Virgo structure presented here, is very diffuse and shows no clear core. Rocha-Pinto et al. (2004) estimate the distance to TriAnd to be at least $\sim 10 \text{ kpc}$. Recently, additional tenuous structures were discovered in the same region of the sky (Majewski et al. 2004; Martin et al. 2007), pointing to the possibility that diffuse clouds such as Virgo and TriAnd are quite common in the Galactic halo.

Assuming that the Virgo overdensity is a part of a larger previously unidentified stream, it would be of interest to look for a possible continuation in the southern Galactic hemisphere. Our preliminary analysis of 2MASS M giant data did not reveal a similarly large density enhancement in the south. It would also be interesting to follow the stream toward the Galactic north, beyond the $Z \sim 20 \text{ kpc}$ limit of our survey, where a signature of overdensity has been revealed by RR Lyrae stars (Duffau et al. 2006). Above all, the understanding of the Virgo overdensity would greatly benefit from measurements of the proper motion and radial velocity of its constituent stars.

6.6. Mapping the Future

This study is only a first step toward a better understanding of the Milky Way enabled by modern large-scale surveys. Star counting, whether interpreted with traditional modeling methods or using number density maps, is limited by the number of observed stars, the flux limit and sky coverage of a survey, and the ability to differentiate stellar populations. All these data aspects will soon be significantly improved.

First, the SDSS has entered its second phase, with a significant fraction of observing time allocated for the Milky Way studies (the Sloan Extension for Galaxy Understanding and Exploration, SEGUE; Newberg & Sloan Digital Sky Survey Collaboration 2003). In particular, the imaging of low Galactic latitudes and a large number of stellar spectra optimized for Galactic structure studies will add valuable new data to complement this work. In addition, the SDSS kinematic data both from radial velocities and from proper motions (determined from astrometric comparison of the SDSS and the Palomar Observatory Sky Survey catalog; Munn et al. 2004) is already yielding significant advances in our understanding of the thin and thick disks and halo kinematic structure (Paper III).

Another improvement to the analysis presented here will come from the *Gaia* satellite mission (e.g., Wilkinson et al. 2005).

Gaia will provide geometric distance estimates and spectrophotometric measurements for a large number of stars brighter than $V \sim 20$. Despite the relatively bright flux limit, these data will be invaluable for calibrating the photometric parallax relation and for studying the effects of metallicity, binarity, and contamination by giants. At the moment, the uncertainties of the photometric parallax relation are the single largest contributor to uncertainties in the derived parameters of Galactic models, and improvements in its calibration are of great interest to all practitioners in this field.

A further major leap forward will be enabled by upcoming deep synoptic sky surveys, such as Pan-STARRS (Kaiser et al. 2002) and LSST (Tyson 2002). Pan-STARRS has already achieved first light with its first telescope, and the four-telescope version may become operational around 2010. If approved for construction in 2009, the LSST may obtain its first light in 2014. These surveys will provide multiband optical photometry of better quality than SDSS over practically the entire sky (LSST will be sited in Chile, and Pan-STARRS is at Hawaii; note that Pan-STARRS will not use the u -band filter). One of their advantages will be significantly deeper data; for example, the LSST will enable studies such as this one to a 5 mag fainter limit, corresponding to a distance limit of 150 kpc for the turnoff stars. LSST proper-motion measurements will constrain tangential velocity to within 10 km s^{-1} at distances as large as that of the Virgo overdensity reported here ($\sim 10 \text{ kpc}$). These next-generation maps will be based on samples including several billion stars and will facilitate not only the accurate tomography of the Milky Way, but of the whole Local Group.

We thank Princeton University, the University of Washington, and the Institute for Advanced Study for generous financial support of this research. Ž. Ivezić and B. Sesar acknowledge support by NSF grant AST 05-51161 to LSST for design and development activity. Donald P. Schneider acknowledges support by NSF grant AST 06-07634. We especially thank the anonymous referee for numerous helpful comments and suggestions which have significantly improved this manuscript.

Funding for the creation and distribution of the SDSS Archive has been provided by the Alfred P. Sloan Foundation, the Participating Institutions, the National Aeronautics and Space Administration, the National Science Foundation, the US Department of Energy, the Japanese Monbukagakusho, and the Max Planck Society. The SDSS Web site is <http://www.sdss.org/>.

The SDSS is managed by the Astrophysical Research Consortium (ARC) for the Participating Institutions. The Participating Institutions are the University of Chicago, Fermilab, the Institute for Advanced Study, the Japan Participation Group, the Johns Hopkins University, the Korean Scientist Group, Los Alamos National Laboratory, the Max-Planck-Institute for Astronomy (MPIA), the Max-Planck-Institute for Astrophysics (MPA), New Mexico State University, University of Pittsburgh, University of Portsmouth, Princeton University, the United States Naval Observatory, and the University of Washington.

This publication makes use of data products from the Two Micron All Sky Survey, which is a joint project of the University of Massachusetts and the Infrared Processing and Analysis Center/California Institute of Technology, funded by the National Aeronautics and Space Administration and the National Science Foundation.

APPENDIX

EFFECTS OF LOCUS PROJECTION

The improvement in the estimate of $r - i$ color resulting from the locus projection depends on the local slope of the locus. If the locus has a steep or almost vertical slope, as for stars with $g - r \sim 1.4$ (cf. Fig. 8), the knowledge of $g - r$ color does not further constrain $r - i$ color. On the other hand, for shallow slopes the knowledge of $g - r$ color determines the intrinsic $r - i$ to a much better accuracy than the $r - i$ measurement alone. For most of the observed $g - r$ color range we are closer to the second regime, with the locus having a slope of $d(r - i)/d(g - r) \sim 0.3$ for $0 < g - r < 1$.

To illustrate the effects of locus projection, in Figure 42 we simulate an ensemble of 10^5 stars with the same color ($g - r = 0.4$, $r - i = 0.143$) subjected to photometric errors representative of SDSS observations ($\sigma_{r-i} = \sigma_{g-r} = 0.03$ mag). Errors introduce a scatter in observed colors as shown in the inset. Using only the $r - i$ information we obtain the expected $\sigma_{r-i} = 0.03$ mag scatter in observed $r - i$ color (*dashed-line histogram*). By projecting the colors to the locus, the scatter is reduced to $\sigma_{r-i} = 0.01$ mag. As we construct density maps for stars binned in color bins with $\Delta(r - i) = 0.05$ mag width, this is a significant reduction in scatter.

There are other benefits of locus projection. Figure 43 illustrates how photometric errors can bias the determination of the number of stars in regions with large gradients of the number density (in the $g - r$ vs. $r - i$ color-color diagram). The solid line shows the true density distribution of stars as a function of $r - i$ color. In this toy model, we used $\rho(r - i) \propto (r - i)^2$, with a sharp cutoff at $r - i = 0.24$ (*solid-line histogram*). Scattering the stars drawn from that distribution with the $\sigma_{r-i} = \sigma_{g-r} = 0.03$ mag photometric errors and binning in $r - i$ color bins produces the dashed histogram (effectively, a convolution of the original distribution with the SDSS photometric errors). It systematically underestimates the original density distribution by as much as 50% in the region of the highest negative density gradient (near the $r - i = 0.24$ cutoff), while overestimating the density in regions with positive density gradient. The exact under- or overestimation depends on the scale at which the true density changes appreciably. If it is significantly smaller than σ_{r-i} or σ_{g-r} , as is the case near the cutoff in Figure 43, the biases become significant. Applying the locus projection gives a much better estimate of the original distribution (*dotted-line histogram*).

This is not a purely hypothetical example; this type of strong density gradient is observed near $g - r \sim 0.2$ (cf. Fig. 8). Figure 44 compares the number of stars per $r - i$ color bin for observed $r - i$ colors (*dashed-line histogram*) and the colors estimated by locus projection (*solid-line histogram*) for the 48 million stars in our star catalog. In the regions of maximal gradients, the locus projection has a $\sim 20\%$ effect on the total number of stars per $r - i$ bin. Not including this correction would similarly bias the density normalization of Galactic models deduced from this sample. The bias would further propagate to luminosity function determination.³⁹

One may further be concerned about the dependence of the location of the $r - i$ versus $g - r$ stellar locus on other parameters. We do observe a slight magnitude dependence of the locus, especially for stars with bluer $g - r$ colors. Figure 45 shows the dependence of the measured $r - i$ color on the r -band magnitude for stars with $0.29 < g - r < 0.31$ (the “worst-case $g - r$ color,” where we find the dependence of the locus location on the magnitude to be the largest). We find a weak, approximately linear dependence, with $d(r - i)_{\text{locus}}/dr \sim 0.007$ mag/mag (*solid line*). The horizontal dashed line shows the location of the locus for this bin as given by equation (5). The two match for $r = 18$. We have chosen to disregard this magnitude dependence when performing the locus

³⁹ For this particular work, the discussed bias is not a problem as we make use of only the reddest bins ($r - i > 1.0$) to measure the Galactic model parameters.

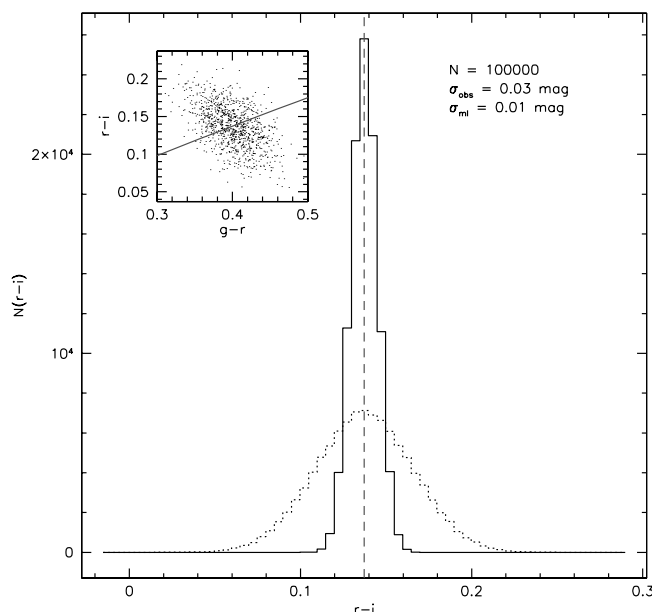


FIG. 42.—Illustration of the reduction in the $r - i$ color scatter after applying the locus projection. An ensemble of 10^5 stars with the same color ($g - r = 0.4$, $r - i = 0.143$) is subjected to SDSS photometric errors ($\sigma_g = \sigma_r = \sigma_i = 0.02$ mag), resulting in the color distribution shown in the inset. Its $r - i$ histogram (*dashed line*) has a rms scatter of $\sigma_{r-i} = 0.03$ mag. After the colors are locus corrected (*solid-line histogram*), the scatter is reduced to $\sigma_{r-i} = 0.01$ mag. The amount of reduction of the scatter depends on the slope of the locus; the more horizontal the locus gets, the better is the determination of the true $r - i$ color. [See the electronic edition of the Journal for a color version of this figure.]

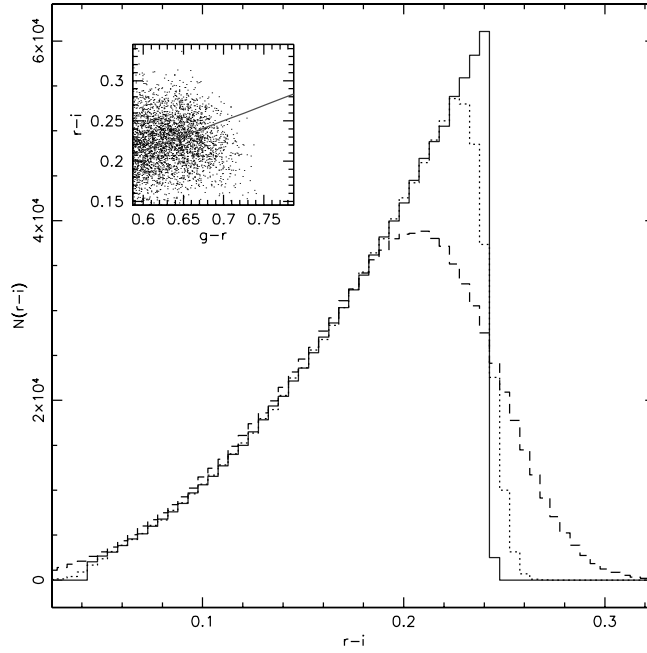


FIG. 43.—Illustration of the bias in the determination of the number density introduced by photometric errors. The solid-line histogram shows a toy model distribution as a function of the $r - i$ color [$\rho(r - i) \propto (r - i)^2$, with a sharp cutoff at $r - i = 0.24$]. The dashed-line histogram is the convolution of the original distribution with SDSS photometric errors ($\sigma_g = \sigma_r = \sigma_i = 0.02$ mag). The measured density of stars with $r - i = 0.24$ is underestimated by as much as 50%. Applying the locus projection gives an improved estimate of the original distribution (*dotted-line histogram*). [See the electronic edition of the Journal for a color version of this figure.]

projection procedure. We reason that the real dependence is not on magnitude but on metallicity⁴⁰ and probably other unknown factors for which we do not have a firm handle. By attempting to correct for those, we risk introducing additional unknown and more complicated biases. Second, the magnitude dependence is relatively small and only affects the bluest bins.

Finally, the three panels in Figure 46 show the histograms of observed $r - i$ colors for stars which have their locus-projected colors in the $0.1 < (r - i)_e < 0.15$ color range. The top panel shows the histogram for all stars in the sample. The 0.03 mag scatter is comparable to SDSS photometric errors. To check for the effects discussed in the previous paragraph, the middle and bottom panels show histograms for the brightest and faintest magnitude bins, respectively. A slight magnitude dependence can be seen as a small shift of the histogram median to the left (*middle*) and right (*top*). In addition, the worsening of photometric precision at the faint end is quite visible in the bottom panel, as the scatter increases to 0.08 mag.

⁴⁰ For example, a part of the shift in locus is likely created by the distant metal-poor stars of the halo, which are preferentially found at fainter magnitudes in our sample.

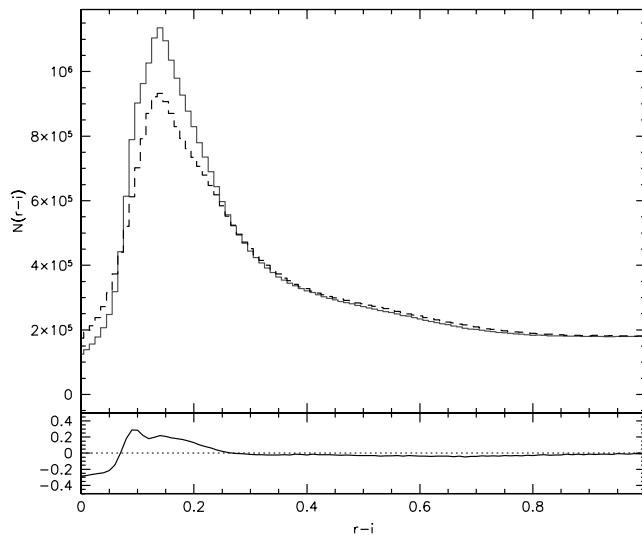


FIG. 44.—Comparison of the number of stars per $r - i$ bin for observed $r - i$ (*dashed-line histogram*) and the locus-corrected $(r - i)_e$ colors (*solid-line histogram*) for the 48 million stars in our star catalog. In the regions of maximal gradients, the locus projection has a $\sim 20\%$ effect on the total number of stars per $r - i$ bin. Not including this correction would similarly bias the density normalization of Galactic models. [See the electronic edition of the Journal for a color version of this figure.]

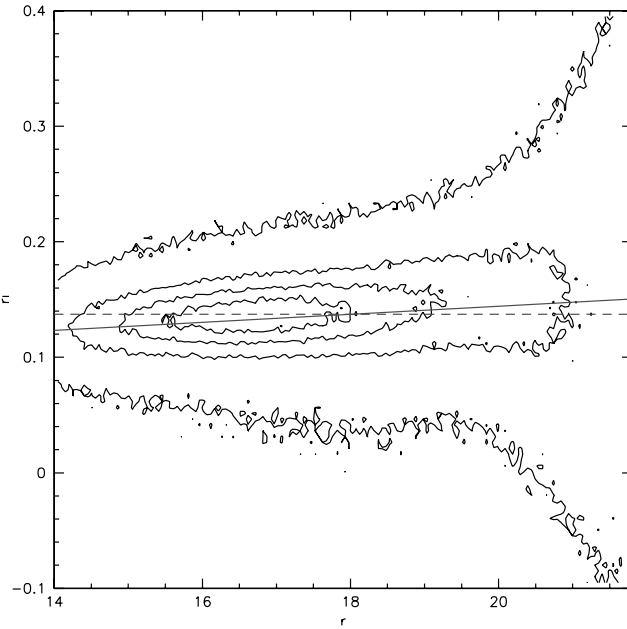


FIG. 45.—Dependence of the measured $r - i$ color on the r -band magnitude for stars with $0.29 < g - r < 0.31$. An approximately linear dependence, with $d(r - i)/dr \sim 0.007 \text{ mag/mag}$ is observed (solid line). The horizontal dashed line shows the location of the locus for this bin as given by eq. (4). The two match for $r = 18$. [See the electronic edition of the Journal for a color version of this figure.]

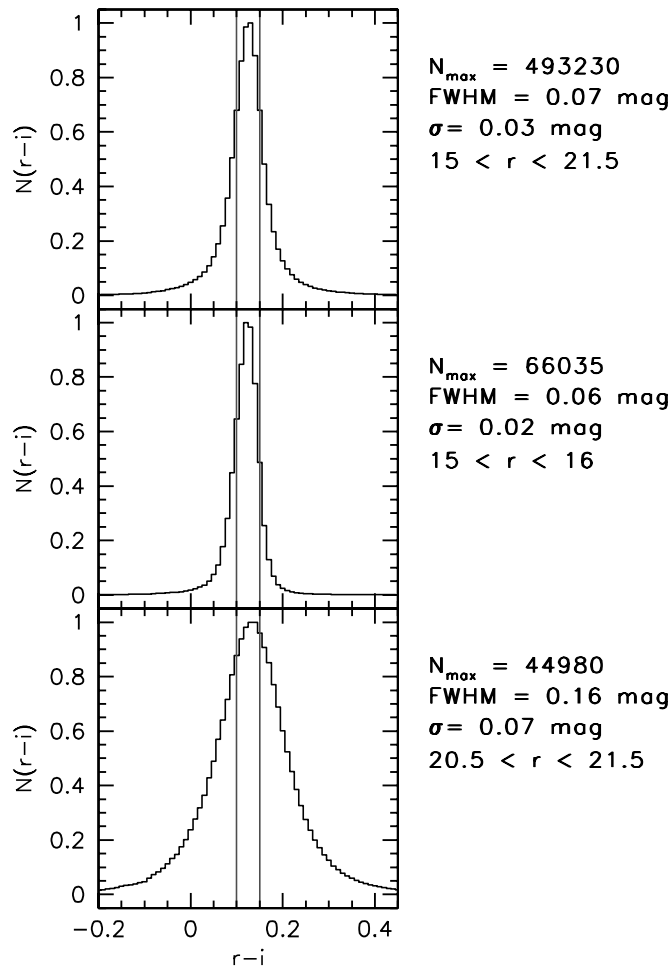


FIG. 46.—Effect of ignoring the magnitude dependence of the locus. The histograms show observed $r - i$ colors of stars having locus-corrected colors in the $0.1 < (r - i)_e < 0.15$ color range. The top panel shows the histogram for all stars in the sample. The spread of $\sigma = 0.03 \text{ mag}$ is comparable to SDSS photometric errors. The middle and bottom panels show histograms for the brightest and faintest magnitude bins, respectively. A weak magnitude dependence can be seen as a small shift of histogram median to the left (middle) and right (bottom). [See the electronic edition of the Journal for a color version of this figure.]

- Sesar, B., et al. 2008, *ApJ*, in press
- Siegel, M. H., Majewski, S. R., Reid, I. N., & Thompson, I. B. 2002, *ApJ*, 578, 151
- Smith, J. A., et al. 2002, *AJ*, 123, 2121
- Smolčić, V., et al. 2004, *ApJ*, 615, L141
- Sommer-Larsen, J., & Zhen, C. 1990, *MNRAS*, 242, 10
- Spitzer, L. J., & Schwarzschild, M. 1953, *ApJ*, 118, 106
- Stoughton, C., et al. 2002, *AJ*, 123, 485
- Tucker, D. L., et al. 2006, *Astron. Nachr.*, 327, 821
- Tyson, J. A. 2002, *Proc. SPIE*, 4836, 10
- Vivas, A. K., et al. 2001, *ApJ*, 554, L33
- Wilkinson, M. I., et al. 2005, *MNRAS*, 359, 1306
- Williams, C. C., et al. 2002, *BAAS Abstr.*, 34, 1292
- Woźniak, P. R., et al. 2004, *AJ*, 127, 2436
- Wyse, R. F. G., & Gilmore, G. 1989, *Comments Astrophys.*, 13, 135
- Yamagata, T., & Yoshii, Y. 1992, *AJ*, 103, 117
- Yanny, B., et al. 2000, *ApJ*, 540, 825
- Yoachim, P., & Dalcanton, J. J. 2005, *ApJ*, 624, 701
- . 2006, *AJ*, 131, 226
- York, D. G., et al. 2000, *AJ*, 120, 1579
- Yoshii, Y., Ishida, K., & Stobie, R. S. 1987, *AJ*, 93, 323
- Zinn, R. 1993, in *ASP Conf. Ser. 48, The Globular Cluster-Galaxy Connection*, ed. G. H. Smith & J. P. Brodie (San Francisco: ASP), 38
- Zinn, R., Vivas, A. K., Gallart, C., & Winnick, R. 2004, in *ASP Conf. Ser. 327, Satellites and Tidal Streams*, ed. F. Prada, D. Martinez Delgado, & T. J. Mahoney (San Francisco: ASP), 92